

Photophysical Studies to Advance Fluorescence Applications in Biophysics

by

Nikita Kumari

A Dissertation Presented in Partial Fulfillment
of the Requirements for the Degree
Doctor of Philosophy

Approved April 2021 by the
Graduate Supervisory Committee:

Marcia Levitus, Chair
Ian Gould
Yan Liu

ARIZONA STATE UNIVERSITY

May 2021

ABSTRACT

Fluorescence spectroscopy has been a vital technique in biophysics due to its high sensitivity and specificity. While the recent development of single-molecule (SM) techniques has furthered the molecular-level understanding of complicated biological systems, the full potential of these techniques hinges on the development and selection of fluorescent probes with customized photophysical properties. Red region probes are inherently desirable as background noise from typical biological systems tends to be at its minimum in this spectral region. The first part of this work studies the photophysical properties of red cyanine dyes to assess their usefulness for particular SM applications.

Protein-induced fluorescence enhancement (PIFE) based approaches are increasingly being used to investigate DNA-protein interactions at the SM level. However, a key limitation remains the absence of good red PIFE probes. This work investigates the photophysical properties of a red hemicyanine dye (Dy-630) as a potential PIFE probe. Results shed light on optimal design principles for ideal probes for PIFE applications, opening new avenues for the technique's broad applicability in biophysical studies.

Further, the photophysical behavior of two novel cyanine fluorophores in the far-red (rigidized pentacyanine) and near-Infrared (IR) (rigidized heptacyanine) region are studied. Both probes are designed to eliminate a photoisomerization caused non-radiative pathway by rigidization of the cyanine backbone. The rigidized pentacyanine was found to have desired photophysical properties and improved quantum yield, vital for application in super-resolution imaging. For rigidized heptacyanine, in contrast to the prior project, it was found that photoisomerization does not contribute significantly to the deactivation

pathway. Thus, this work clarifies the role of photoisomerization on heptamethine cyanine scaffold and will enable future efforts to optimize NIR dyes for diverse applications.

The second part of this work aims to answer the fundamental question of how the physics of DNA can impact its biology. To this end, interlinkage between the flexibility of local sequence context and the efficiency of uracil removal by Uracil-DNA glycosylase (UDG) protein is investigated using fluorescent base analogue, 2-Aminopurine (2-AP).

In summary, this work focuses on photophysical investigations, the understanding of which is vital for the selection and development of fluorescent probes for biophysical studies.

ACKNOWLEDGMENTS

I am indebted to many people for their help, collaboration, and support in completing this work. Firstly, I would like to thank my advisor, Dr. Marcia Levitus for her time, effort, and support throughout my PhD journey. She has taught me how to approach scientific problems in a rigorous manner and her dedication towards science is a constant source of inspiration for me. I thank my committee members, Dr. Ian Gould, and Dr. Yan Liu for their time and attention to my research work. I would like to show my appreciation towards Dr. Su Lin who has ensured the smooth running of TCSPC and transient absorption setups for my experiments.

I would like to thank Dr. Monika Ciuba who I worked with on my first project and who has trained me in using various instruments in the lab. I would like to thank Dr. Martin Schnermann from National Cancer Institute (NCI), who collaborated with our group for two projects discussed in chapter 3 and 4. I want to thank all the past and present graduate and undergraduate students in the Levitus group who I have interacted with along the way who have made my time in the lab enjoyable.

I can't thank enough my parents for their immense support and relentless commitment to my dreams. As a first-generation college student, I am deeply indebted to them for providing me the opportunities that were not readily available to them. I would also like to thank my brother, Gaurav, for being my biggest cheerleader, critique, and confidant since day one of my life. I would like to express my heartfelt gratitude towards my friends who have stuck by me throughout this journey, and I am lucky to have such a great support system in my life. Finally, I would like to acknowledge the efforts of educators throughout my academic life who have instilled in me a love for science and a lifelong quest to learn new things.

TABLE OF CONTENTS

	Page
LIST OF TABLES	viii
LIST OF FIGURES	ix
CHAPTER	
1 INTRODUCTION	1
1.1 Photophysical Terms to Understand Fluorescence	1
1.2 Biophysical Applications of Fluorescence.....	7
1.3 Fluorophores	9
A. Rhodamine	11
B. Carbopyronin and Oxazine.....	12
C. Carbocyanine.....	12
1.4 Photophysics of Cyanines.....	14
1.5 Techniques to Quantify Photophysical Properties	20
A. Quantum Yield Measurement	20
B. Lifetime Measurement	24
C. Pump-Probe Measurement	28
D. Total Internal Reflection Fluorescence (TIRF) Measurement.....	31
1.5 Scope and Contribution.....	33
2 <i>METHODS AND APPLICATIONS IN FLUORESCENCE</i>	
“PHOTOPHYSICAL PROPERTIES OF THE HEMICYANINE DY-630	

CHAPTER	Page
AND ITS POTENTIAL AS A SINGLE-MOLECULE FLUORESCENT PROBE FOR BIOPHYSICAL APPLICATIONS”	36
2.1 Abstract.....	36
2.2 Introduction.....	37
2.3 Methods.....	42
A. Materials and Chemicals	42
B. Absorption and Steady-State Fluorescence Spectroscopy	43
C. Time-Resolved Fluorescence Spectroscopy.....	45
D. Single-Molecule Fluorescence	46
2.4 Results and Discussion	47
A. Absorbance Properties of Rhodamine Dimers.....	47
B. Laser Flash Photolysis.....	51
C. Interactions between Dy-630 and the DNA Nucleobases.....	54
D. Fluorescence Properties of Dy-630 Bound to DNA	57
2.5 Discussion.....	63
2.6 Conclusions.....	69
2.6 Acknowledgements.....	70
3 <i>JOURNAL OF THE AMERICAN CHEMICAL SOCIETY</i> “CYANINE CONFORMATIONAL RESTRAINT IN THE FAR-RED RANGE”	71
3.1 Abstract.....	71
3.2 Main Text.....	71

CHAPTER	Page
3.3 Acknowledgments.....	80
4 <i>THE JOURNAL OF ORGANIC CHEMISTRY</i> “DEFINING THE IMPACT OF CYANINE CONFORMATIONAL RESTRAINT IN THE NEAR- INFRARED RANGE”	82
4.1 Abstract.....	82
4.2 Introduction.....	83
4.3 Results and Discussion	86
4.4 Conclusion	97
4.5 Acknowledgments.....	98
5 MOLECULAR BASIS OF DNA SEQUENCE-DEPENDENT URACIL REMOVAL EFFICIENCY INVESTIGATED BY FLUORESCENCE	100
5.1 Introduction.....	100
5.2 UDG Function.....	101
5.3 Sequence Dependence and Interlink to Flexibility	103
5.4 Photophysical Properties of 2-Aminopurine.....	106
5.5 2-AP as a Probe of the DNA Duplex	107
5.6 Materials and Methods.....	114
A. Chemicals and Sequences	114
B. Kinetic Assay	116
C. Measurement of Quantum Yield of DNA Sequences	118
D. Lifetime Measurements.....	120

CHAPTER	Page
5.7 Results and Discussion	125
A. Quantum Yield.....	125
B. Lifetime Analysis	125
C. Ultrafast-Decaying Dark Species Population.....	127
D. UDG Uracil Removal Kinetics	130
E. Ultrafast-Decaying Dark Species Correlation to Rigidity.....	131
5.8 Future Work	132
REFERENCES	136
APPENDIX	
A SUPPLEMENTAL INFORMATION FOR CHAPTER 2	156
B SUPPLEMENTAL INFORMATION FOR CHAPTER 4	167
C GLOBAL LIFETIME REPRODUCIBILITY STUDIES FOR CHAPTER 5.....	195
D REUSE PERMISSION FOR PUBLISHED WORK	198

LIST OF TABLES

Table		Page
2.1	Spectroscopic and Photophysical Properties of Dy-630, diIC ₂ (5), and diIC ₂ (3) in Pure Solvents	66
2.2	Fluorescence Quantum Yields and Lifetimes of Cy5, Dy-630, and Dy-632 Covalently Bound to DNA.....	68
4.1	Spectroscopic and Photophysical Properties of 1 and 2	90
5.1	Sequences Used in Initial Studies	115
5.2	Quantum Yield Reference Sequence	118
5.3	Parameters Derived From the Globally Fitted Decays of Sequence 1 rev	123
5.4	Parameters Derived From the Globally Fitted Decays of Sequence 1	123
5.5	Parameters Derived From the Globally Fitted Decays of Sequence 2	123
5.6	Parameters Derived From the Globally Fitted Decays of Sequence 3	124
5.7	Parameters Derived From the Globally Fitted Decays of Sequence 4	124
5.8	Parameters Derived From the Globally Fitted Decays of Sequence 4 rev	124
5.9	Quantum Yield Results for DNA Sequences.....	125
5.10	Lifetime Analysis of DNA Sequences	127
5.11	Calculated α_0 for DNA Sequences	128
5.12	α_0 and Corrected Fractional Distribution of Lifetime Components.....	129
5.13	Sequences to Be Studied Next	133

LIST OF FIGURES

Figure	Page
1.1 Energy Diagram of a Typical Fluorescent Molecule.....	2
1.2 Fluorophore Structures	11
1.3 Basic Cyanine Structure	13
1.4 Potential Energy Diagram for Cyanine Photoisomerization	15
1.5 Setup for Fluorimeter Used for Steady-State Measurement.....	21
1.6 Inner Filter Effect.....	23
1.7 Working of TCSPC.....	25
1.8 Schematic of TA Setup.....	30
1.9 TIRF Setup and Slide Preparation.....	31
2.1 Chemical Structures of Dyes Used.....	42
2.2 Photophysical Properties of Dyes.....	49
2.3 Transient Absorption Data for Dy-630	52
2.4 Steady-State Data of Dy630 with dNMP	55
2.5 Lifetime Data of Dy630 with dNMP	57
2.6 Lifetime Data of Dy-630-DNA with KF.....	59
2.7 Single-Molecule Traces of Dy-630-DNA.....	60
2.8 Single-Molecule Traces of Dy-632-DNA.....	62
2.9 Dwell Time Analysis of Dy-630-DNA and Dy-632-DNA	64
3.1 Structural Information of Fluorophores	72
3.2 Photophysical Properties of Parent and Restrained Fluorophore	77

Figure	Page
3.3 Super-Resolution Imaging Data	79
4.1 Restrained Cyanine Structure	86
4.2 Transient Absorption of Parent and Restrained Fluorophore	91
4.3 Solvent and Temperature Dependence of Parent and Restrained Fluorophore	92
4.4 Computational Studies for Energy Levels	94
5.1 UDG Activity Mechanism.....	102
5.2 Structures and Hydrogen-Bonding.....	105
5.3 Quenching of 2-AP Fluorescence Placed on DNA.....	110
5.4 Cartoon Representation of Population on DNA.	112
5.5 2-AP Based UDG Kinetic Assay	117
5.6 Residual Comparison for Three and Four Lifetime Components Fit.....	122
5.7 Lifetime Decay of Sequences Shown With IRF.....	126
5.8 Stacked Column Plot of Calculated Amplitudes for Sequences	132

CHAPTER 1

INTRODUCTION

1.1 Photophysical Terms to Understand Fluorescence

Fluorescence is a common theme of this work and it's imperative to start with steps that lead to fluorescence in a molecule. A molecule can be represented by a state energy diagram, as shown in figure 1 which is used routinely to keep track of the ground state, the lowest-energy excited singlet state, and the lowest-energy excited triplet state. State energy diagram is commonly referred to as Jablonski diagram in honor of a Polish scientist, Aleksander Jablonski, who first portrayed the relative positions of electronic and vibrational levels without an attempt to indicate the nuclear geometries of the states.¹ Hence the horizontal (x) axis has no physical meaning. The lines representing singlet (S_1) and triplet (T_1) are displaced just to avoid congestion in the diagram. The vertical (y) axis represents the potential energy coordinate of the system. Higher energy singlet ($S_2, S_3..$) and triplet ($T_2, T_3..$) state are not included in figure 1 for clarity and it's known that excitation of these higher-energy excited states results in deactivation to S_1 and T_1 faster than any other measurable process (rate in the range of 10^{-13} - 10^{-12} s) which is called Kasha's rule. Kasha's rule states that polyatomic molecules generally luminesce with appreciable only from the lowest excited state.² This observation is a consequence of energy differences between upper excited states of a given multiplicity being much smaller than those between the lowest singlet or triplet state and the ground state so that the rates of internal conversion

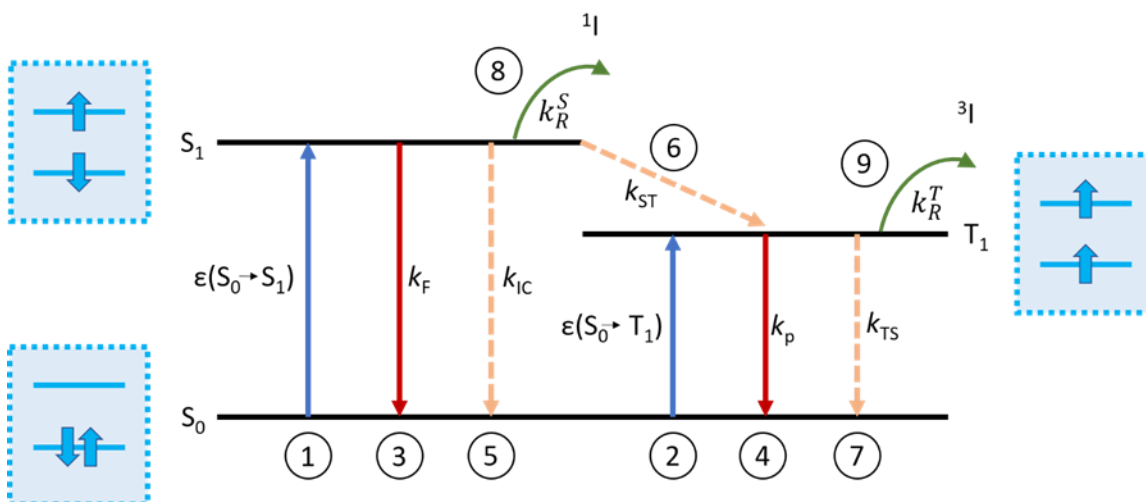


Figure 1.1: Energy Diagram of a Typical Fluorescent Molecule. The electronic configurations of the respective state are shown in the blue box next to the states. Photophysical steps (circled with numbers) are discussed in detail in the main text. S=singlet state, T=triplet state, F=fluorescence, IC=internal conversion, p=phosphorescence, R=primary photochemical reaction, 1I and 3I =singlet and triplet reactive intermediate respectively, k=rate constant, ϵ =extinction coefficient, 0=ground state, 1=first excited state.

(IC) (a non-radiative process which will be discussed further in details) from upper excited states far exceed the rates of fluorescence and phosphorescence. The spin allowed singlet-singlet absorption of photons as shown in step 1 is characterized by an extinction coefficient, $\epsilon(S_0 \rightarrow S_1)$ and the spin-forbidden singlet-triplet photon absorption (step 2) with extinction coefficient, $\epsilon(S_0 \rightarrow T_1)$. The time scale of electronic absorption is $\sim 10^{-15}$ s in the ultraviolet-visible (UV-VIS) and absorption of electromagnetic radiation in the UV-VIS range always populates an electronic excited state. The extinction coefficient is an experimentally determined quantity, determined by using beer-lambert law, which considers the ability of a molecule to absorb light at a particular wavelength:

$$A = \log_{10} \left(\frac{I_0}{I} \right) = \epsilon \cdot l \cdot c \quad (1.1)$$

where A is the absorbance of light through a material of pathlength l and concentration of the absorbing substance c . I_0 and I is the intensity of light entering and exiting the substance, respectively. Absorbance is measured using a spectrometer and then often used to determine the extinction coefficient of a known concentration solution or concentration of a known extinction coefficient as path length is known in the majority of cases. The only term dependent on the molecule is the extinction coefficient, which is also dependent on wavelength. So, it's not surprising that the wavelength-dependent extinction coefficient is the dictating factor in the shape of absorbance spectrum and region of absorption for a molecule.

To understand what dictates the value of extinction coefficient, we need to think of the molecular picture, which brings us to absorption cross-section (σ) which is closely connected to extinction coefficient and expressed in units of area. However, it has nothing to do with the size of the molecule but the size of “target” or area of space around a molecule that is accessible to being struck by a passing photon. So, the intensity of light being absorbed can be expressed as:

$$I(x+dx) - I(x) = dI(x) = -I(x) \cdot \sigma \cdot N = -I(x) \sigma \cdot n \cdot dx \quad (1.2)$$

where n = molecules/cm³, N = molecules/cm² and σ = cross section (cm²/molecule).

So, equation 1.2 can be written as:

$$\frac{dI(x)}{I(x)} = -\sigma \cdot n \cdot dx \quad (1.3)$$

Further, integrating gives us $\ln\left(\frac{I(x)}{I_0}\right) = -\sigma \cdot n \cdot x$ (1.4)

Coming back to the point of how this approach is related to beer-lambert law, we try to express equation 1.4 using conversion $\ln(x) = 2.303 \log(x)$, for $x = I$ and $C = M$ (mol/dm^3) = $1000 \cdot n / N_{av}$

$$\log\left(\frac{I_0}{I(l)}\right) = \frac{\sigma \cdot N_{av}}{2.303 \cdot 1000} C \cdot l = \varepsilon \cdot C \cdot l \quad (1.5)$$

Thus, giving us a relationship between ε and σ ,

$$\varepsilon = \frac{\sigma \cdot N_{av}}{2.303 \cdot 1000} \quad (1.6)$$

The cross-section is related further to dipole and transition moments but the probability that a molecule will absorb a photon is highest when the electric vector of the photon is parallel to the absorption transition dipole moment (μ) and falls to 0 when perpendicular.³

Step 3 is the radiative step that gives rise to fluorescence, which is the spontaneous emission of radiation by an excited molecule, typically in the first excited singlet state (S_1) with retention of spin multiplicity. The timescale of this step is in the range of 10^{-9} - 10^{-7} s. The absorption generally happens to a wide range of vibrational levels of S_1 , which ultimately relax back to the lowest vibronic level of this one, and the timescale of this vibrational relaxation is much faster than fluorescence (in the range of 10^{-13} - 10^{-12} s). Thus, all of the electrons are in the lowest vibrational state of S_1 before the step of fluorescence

takes place, and hence, the energy of electron emitted during fluorescence is always less than the energy absorbed. Therefore, the fluorescence spectrum is always red-shifted as compared to the absorbance spectrum. When such transition happens from triplet state (T_1) to ground state (S_0) happen (step 4) they are generally longer in timescales than step 3 (10^{-3} – 10^2 s) and are termed as phosphorescence. It's important to understand what dictates the extent of electrons coming to the ground state via radiative emission. If we could get one photon out as fluorescence per photon absorbed, we would get a fluorescence efficiency of one for fluorescence. However, as will be discussed next, other non-radiative pathways compete with the fluorescence pathway of deactivation, and thus, this efficiency, which is formally known as quantum yield is never one.

Electronic transition selection rules forbid transition between different spin states and thus such transitions between singlet and triplet states are called forbidden. However, this rule doesn't take into regard the cases where spin and the orbital angular momentum interaction exist (spin-orbit coupling). When such interactions are possible between singlet and triplet level, an isoenergetic radiationless process can happen which is known as intersystem crossing (steps 6 and 7).

Internal Conversion is an isoenergetic radiationless transition between two electronic states of the same multiplicity, between the vibrational level of close energies (step 5). This is aided by the solvent molecules such that once the electron in the excited state has relaxed back to its lowest vibrational level, the excess vibrational energy can be transferred to the solvent molecule during collisions. Internal conversion is the main

pathway of deactivation from S_2 to S_1 however less efficient from S_1 to S_0 , because of the much larger energy gap between S_1 and S_0 .

Quenching is a general term for any process involving an external environmental influence (the quencher) that results in the deactivation of the excited state of a molecule in a non-emissive manner (step 8 and 9 could be either iii or iv). The quenching mechanism varies depending on the quencher. For example, fluorescence quenching by nucleobases and amino acids is most often a photoinduced electron transfer (PET).^{4,5} PET happens when the excited state of a fluorophore donates or accepts an electron from the quencher to form a radical ion pair which later decays to the ground state by charge recombination. The quenching can be divided further into 2 categories: Static and dynamic. Static quenching is when the fluorophore and quencher associate over timescales much longer than the lifetime of the unquenched excited state of the fluorophore. In contrast, dynamic quenching happens when the association between quencher and fluorophore is transient or stable in the timescale of the excited state lifetime.

Energy Transfer happens when the excited state transfers its energy to a second molecule due to weak interaction between the transition dipole moments of the two molecules. The mechanism of this transfer is strongly dependent on the distance between the excited fluorophore (donor) and the second molecule (acceptor).⁶

It should be noted that there are other nonradiative processes unique to the family of fluorophores. One such process of our interest is the formation of non-fluorescent photo isomer in cyanine, which leads to a major non-radiative will be discussed in depth later in this chapter.

1.2 Biophysical Applications of Fluorescence

Therefore, fluorescence spectroscopy has been a lucrative choice in the field of biophysics where people routinely attach fluorescent molecules (extrinsic fluorophores) to biomolecules (e.g., DNA, proteins) and study the fluorescent properties of the system to get both kinetic as well as at equilibrium information.⁷⁻¹⁰ As many of the above-mentioned deactivation pathways are dependent on the environment the molecule is in, monitoring the changes in deactivation rates can give insights about change in the environment of the fluorescent molecule or fluorophore. Hence, fluorescence is used to study the change in the environment *in vivo* and *in vitro* alike where the fluorophore is incorporated in the biological system. These changes, if monitored in a timescale where the biomolecular interactions happen, can give useful information about the dynamics of these interactions, for example, protein-DNA interactions.¹¹ Such techniques are around for a long time, however, newer techniques and materials are being discovered every year which has made fluorescence one of the most versatile tools in biophysical research and biomedical application. Additionally, this field has gained momentum with the development of single-molecule (SM) techniques such as super-resolution microscopy and the emergence of methods such as protein-induced fluorescence enhancement (PIFE) in the last two decades. One of the most important reasons to use SM experiments instead of ensemble experiments is the ability to observe the dynamics in the biological system, such as DNA-protein interactions, subunit movement in proteins, and translocation of biomolecules. Thus, SM techniques give us the capability to understand the structure-function-dynamics relationship of a biomolecule better. Therefore, SM helps us capture the physiological

complexity of a cell, making fluorescence techniques even more relevant for biological research. Two of these SM techniques relevant to the next chapters are as follows:

In the last decade, the SM field has radically overcome the classical diffraction limit by using super-resolution imaging techniques. The Nobel prize in chemistry 2014 was awarded to three scientists involved in the development of stimulated emission depletion (STED) and Photoactivated Localization Microscopy (PALM) super-resolution fluorescence microscopy (SRM) methods.¹²⁻¹⁴ The most common super-resolution imaging requires three steps. The first step is the activation of a subset of fluorophores in an optically resolvable way, followed by the determination of the positions of these fluorophores with sub-diffraction-limit precision. The third step is to repeat the first two steps to allow stochastically different subsets of fluorophores to be turned on and reconstruct an image from the positions of many activated molecules. One important factor in this cycle of events to reconstruct a super-resolution image is the number of photons detected per switching event. One of the main challenge in SM and super-resolution techniques today is that the quality of a super-resolution image is limited by the number of photons detected per switching event as localization precision, and therefore the structural resolution capability of single-molecule localization microscopy (SMLM), scales with the inverse square root of the single-molecule emitter intensity. The emitter intensity is an intrinsic property of the fluorophore (quantum yields) which specifically becomes a crucial problem due to the low quantum yield of fluorophores in the red region. Hence, in Chapters 3 and 4, efforts to improve the brightness for far-red and near-Infrared (IR) spectral range cyanine dyes will be discussed in further detail, respectively.

Furthermore, PIFE is a phenomenon where an increase in fluorescence intensity is observed when a protein binds to a nucleic acid in the proximity of a fluorescent probe.¹⁵ This technique has been used to study DNA-protein interaction and has a clear advantage over SM-FRET as PIFE doesn't require labeling of the protein, which can be difficult and can perturb the function of the protein. This technique is short-distance sensitive in the region where FRET is insensitive. Thus, these two techniques could be used together as synergistic multiscale molecular ruler and there have been a few reported studies which gain deeper insight into DNA- protein.¹⁶ This technique will be discussed in further detail in chapter 2, where the origin of this phenomenon will be discussed in photophysical terms.

1.3 Fluorophores

It's well known that not all biological materials have fluorescent components incorporated into them. However, there are a few naturally fluorescent amino acids (eg. phenylalanine, tyrosine, and tryptophan) that are present in proteins. Such fluorescent molecules or fluorophores are called intrinsic fluorophores. However, in the majority of cases, we need to introduce an artificial molecule in the biomolecule to a fluorescence study, and such fluorophores are called extrinsic fluorophores. The best thing about these extrinsic fluorophores is that there are a wide variety of commercially available options which one can choose from, depending on the kind of application, thus providing excellent tunability during experimental design. For example, there are both environment dependent as well as independent fluorophores available. One can choose a bright environment independent option if the sole aim is to get good-resolution imaging of a cell. However, if

one needs to study the dynamics, where the need is a signal which is sensitive to change in the environment, there are a variety of environment-dependent fluorophores available.

Fluorescent base analogues are small fluorescent molecules that resemble the shape of the natural nucleobases and H-bonding ability and do not seriously perturb the overall structure of the nucleic acid.¹⁷ Thus, these classes of fluorophores can give us information about the local environment of the DNA, more or less in its native behavior. The intrinsic fluorophores can be divided further based on their environment-dependent photophysical properties as environment-sensitive and environment insensitive.

Environment-sensitive base analogues are molecules that have quantum yield and lifetime dependent on factors such as hydrogen bonding, single- or double-stranded environment, and neighboring bases. One most commonly used environment-sensitive base analogue is 2-Aminopurine, which was discovered in 1969 and since then, routinely used for biochemical research. It is highly fluorescent in the free environment (quantum yield = 0.68¹⁸), which gets dramatically decreased due to quenching when placed in a DNA context. The quenching properties are highly dependent on the microenvironment of 2-AP and hence it can be used to extract useful information about nucleic acid structure and dynamics. Monitoring changes in such properties can give information about the dynamics of biochemical processes and one such application will be discussed in chapter 5 of this thesis.

Environment insensitive base analogue is the class of base analogues that have an environment-independent photophysics that is not perturbed much by its

microenvironment. This class of probes becomes important when fluorescence is being used merely for detection. One such example is tricyclic cytosine analogue (tC), which has a fluorescence quantum yield that is unaffected by its immediate surroundings.¹⁹

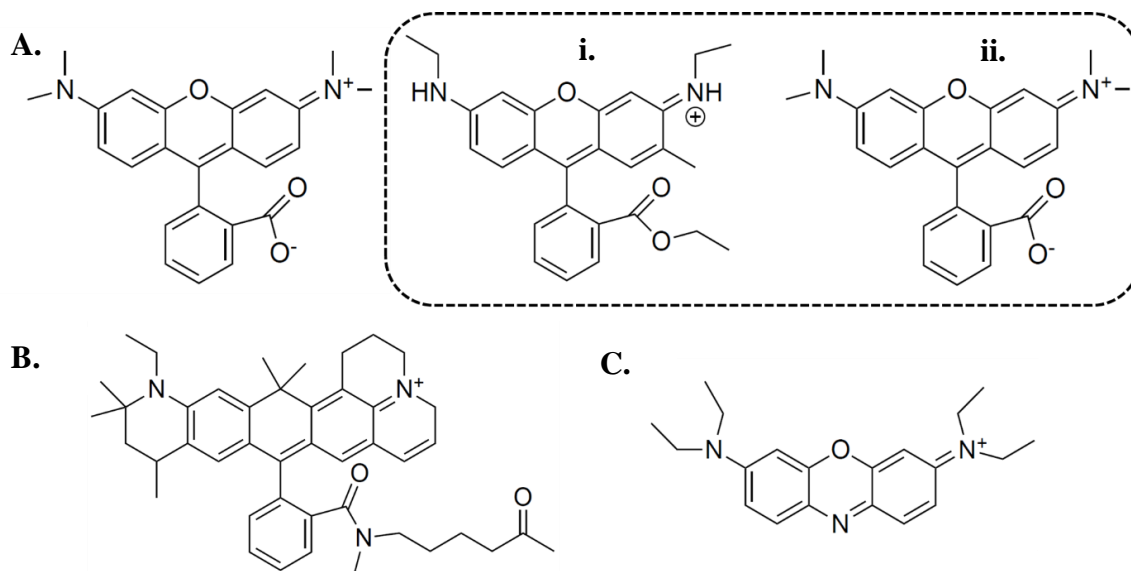


Figure 1.2: Fluorophore Structures. (A) General structure of rhodamine and inside dotted box (i) Rhodamine G, (ii) TMR, (B) ATTO 647N, and (C) General structure of oxazine.

Further, there are a wide variety of organic molecules that can be attached to biomolecules by having the reactive derivative of the fluorophore that selectively binds to a functional group contained in the target biomolecule. There are some popular families of fluorophores that share a similar structure frame and the most common families are shown here.

A. Rhodamine

This family is a subgroup of triarylmethane dyes which absorb in the 520-570 nm range. The properties are highly dependent on the alkylation of amino acid and on whether

the carboxyl group in the phenyl ring is esterified or not. The most commonly used dyes from this category are, Rhodamine 6G and tetramethyl rhodamine (TMR). One unique property of rhodamine around biomolecules is that it is efficiently quenched by guanosine and tryptophan. Also, self-quenching is observed when they form dimers.^{20,21}

B. Carbopyronin and Oxazine

These families have a very similar structure to Rhodamines, but the oxygen in the ring is replaced by a geminal dimethyl group for Carbopyronins (eg ATTO 647N), giving a red-shifted dye family. Similarly, a red shift is observed when the ring carbon of rhodamine is replaced by a nitrogen, and this class is known as oxazine. One distinctive property of oxazine dyes is their high electron affinity compared to other classes which lead to a high oxidation potential or resistance to oxidation by molecular oxygen, which makes them more resistant to photobleaching in aerated conditions.²²

C. Carbocyanine

In most basic form, cyanine dyes consist of two nitrogen atoms linked by a conjugated polymethine chain containing an odd number of carbon atoms as shown in figure 1.3. Heterocyclic rings can be attached at both ends to make the molecule more stable such as indole, quinoline, benzoxazole, or benzothiazole. Symmetric cyanines contain the same ring on both sides whereas asymmetric cyanines can have two different rings on each end. These groups can be designed to give specific properties such as adding sulfonates to increase the solubility in water and prevent aggregation. The most unique and advantageous part of using cyanine is its optical tunability, i.e. the absorption

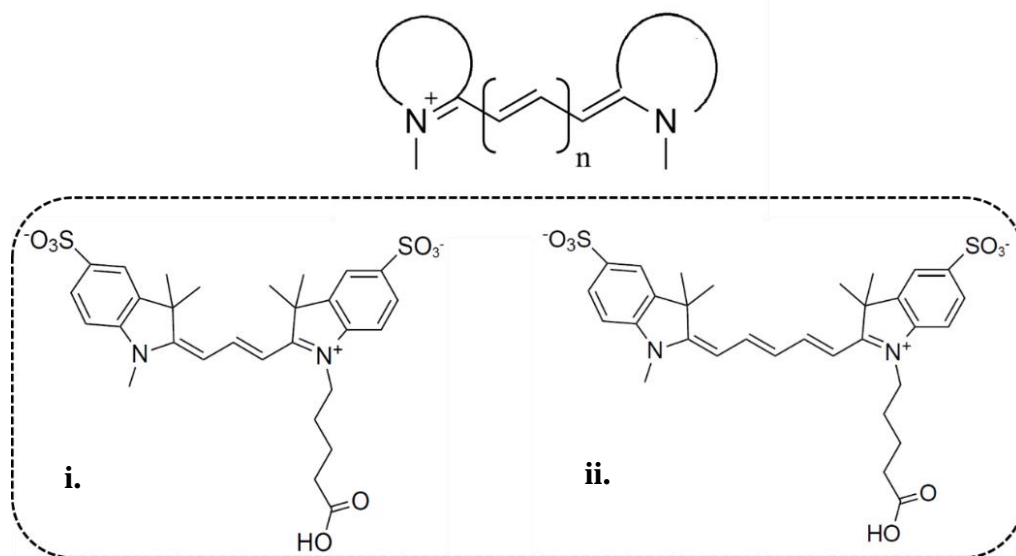


Figure 1.3: Basic Cyanine Structure. Two commonly used cyanines (i) Cy3 (green dye), (ii) Cy5 (red dye).

spectra can be shifted to the red by just increasing the length of the polymethine chain. The most commonly used cyanines in biophysical research are Cy3 (green) and Cy5 (red), which are both indocyanines that differ in the length of the polymethine chain as shown in the figure. The use of the term “Cy” for these dyes began in the late 1980s; the accompanying number refers to the number of carbon atoms in the polymethine chain. One interesting feature of cyanine is an enhancement in fluorescence when it gets stacked between DNA bases. This observation is well-explained by the photophysical landscape of cyanine which will be discussed in detail in the next section.

1.4 Photophysics of Cyanines

The energy landscape of the cyanine is shown in figure 1.4 which was proposed by Rulliere in 1976.²³ The ground state (S_0) and excited potential (S_1) energy levels are separated in energy and thus a transition can only happen if a photon with appropriate energy gets absorbed. Also, the potential energy of the states (y-axis) is dependent on the torsional angle between the two heterocycles (x-axis). As shown in the structure, cyanine contains a polymethine chain that can rotate (related to the x-axis of the energy landscape is this angle of torsion) about carbon-carbon double bonds to give rise to different structural isomer, i.e. cis (180°) and trans (0°). It's important to note that the cis form of cyanine is practically non-fluorescent for the dyes being studied in this work whereas the trans form is responsible for cyanine being fluorescent. In the ground state, the trans isomer (symbol N for native) is of lower energy and thus, most stable. Hence, most of the cyanines are in the trans isomer state. Upon photon absorption, there are multiple possible routes of deactivation from the excited state (S_1), i.e. fluorescence (f) and internal conversion (ic) the rate constants of these processes are denoted as k_f and k_{ic} , respectively. As shown in the figure, the process of going to the cis ground state from trans excited state is a two-step process, designated by rates k_{Nt} , and k_{tP} .

In this case, photoisomerization (isomerization from the excited state) can happen to cis state due to touching of energy surfaces at a point, which is explained by the “free-rotor” effect which is observed during extreme vibrations, in this case, severe twisting of the of a double bond.²⁴ A twisting vibration can escort the excited state energy surface to a

region in the ground state near the point where the two energy states are the closest called conical intersection as shown in figure 1.4. A conical intersection can be thought of as an

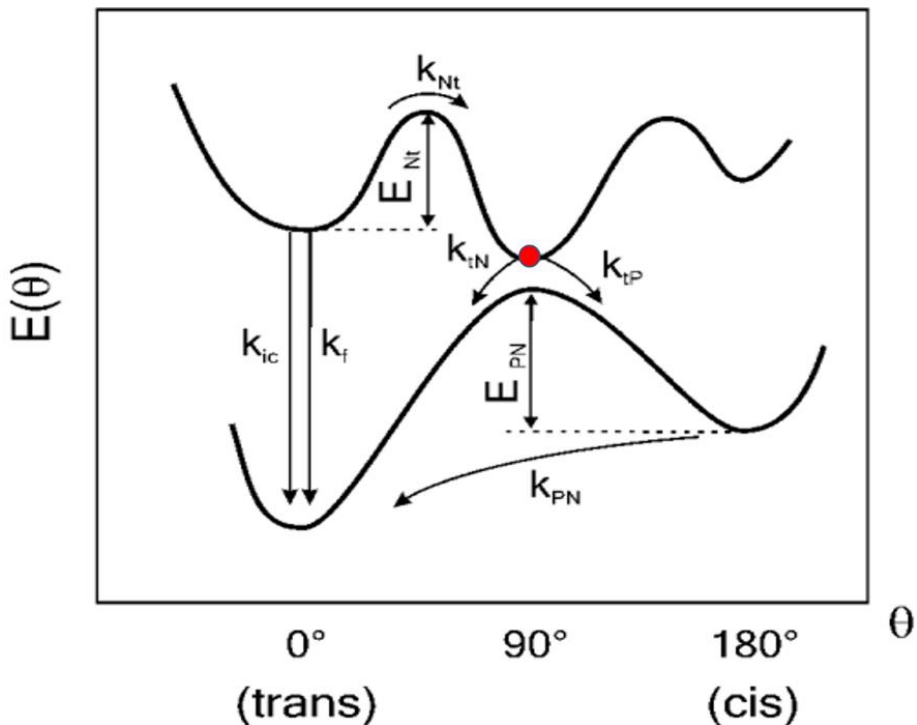


Figure 1.4: Potential Energy Diagram for Cyanine Photoisomerization. The energies of the ground and first singlet excited states are represented as a function of torsion angle (θ). N represents the normal form (trans isomer), t the twisted state, and P the cis photoisomer. k_{ic} and k_f represent the internal conversion and radiative fluorescence rates, respectively. The red dot represents the conical intersection. Adapted from reference 27 Copyright© Cambridge University Press 2010.

energy funnel between two electronic states where the probability of non-adiabatic, non-radiative jumps is high. If the twisting vibration causes vibronic mixing of excited state and ground state energy (wavefunctions), a radiationless transition from S_1 to S_0 is possible. These vibrations can also act as an energy acceptor of energy that is involved in the transition from S_1 to S_0 . In the case of C-C double bond rotation, the “free rotor” takes up the excess energy due to transition and begins to rotate. The twisting motion finally leads

to cis-trans isomerization, giving rise to a lower fluorescence as the cis form of cyanine dye is non-fluorescent. The quantum yield is a measure of fluorescence efficiency and given as the number of photons emitted as fluorescence over a given time, divided by the number of photons absorbed by the molecule. Thus, it can also be represented as a ratio of rate constant for fluorescence divided by the sum of rate constants of all the photophysical processes that can happen, and for cyanine dyes, can be written as:

$$\phi = \frac{k_F}{(k_f + k_{ic} + k_{Nt}(T, \eta))} \quad (1.7)$$

The k_{Nt} is a temperature (T) and viscosity (η) dependent process as it involves crossing an activation energy barrier. Low temperature and rigid intermolecular conditions or highly viscous solvents can inhibit the twisting motion which promotes radiationless transfer.²⁹ This can be thought of as a higher energy barrier E_{Nt} in case of higher viscosity solvent, as the movement of molecules in the neighborhood of the twisting C=C becomes difficult. Conjugation and binding to biomolecules also increase the fluorescence lifetime (τ) and quantum yield (ϕ) of short cyanines as it restricts the motion around the C=C, making the “free-rotor” less efficient. It is worth noting that twisting motion is severely hindered by structural constrained such as if C=C is part of a cyclic structure as these molecules are unable to adopt nuclear geometry that differ substantially from the initial geometry of S_0 due to rigidity and thus lack the closest point where transition from S_1 to S_0 can happen in their energy landscape.^{25–28} The k_{Nt} and k_{Pn} term is also dependent on temperature as with any activated process. However, owing to the temperature dependence of viscosity as well, k_{Nt} is not expected to have an Arrhenius behavior, it still fits this

description in the relatively small temperature range of our measurements.³⁰⁻³³ Thus, low temperatures decrease the non-radiative deactivation rates making the fluorescence efficiency better. Solvent polarity does not have a significant effect on the fluorescence lifetime and quantum yields of shorter cyanines, however, becomes important for longer, near-IR cyanines. This is not because the polarity changes the rates of photoisomerization, but because of another non-radiative process, internal conversion becomes the main non-radiative pathway and this pathway is highly dependent on the polarity of the solvent. This will be discussed in further detail in chapter 3.

For example, diC₂(3) which is a carbocyanine similar to Cy3 but without sulfonate groups has a $\phi = 0.042$ ³⁴ and $\tau = 162$ ps²⁹ in ethanol and it was observed that the photophysical properties of such dyes shows a strong dependence on the viscosity of solvent as well as temperature. The general trend is a short lifetime and low quantum yield in low viscosity solvents which increases with solvent viscosity. Also, to be noted is a molecule called Cy3BTM which has a restrained polymethine chain by installing a cyclic structure, which leads to a drastic increase in quantum yield 0.68 and a lifetime of 2.8 ns.³⁵ It should be noted that the rates of intersystem crossing are negligible³⁶ ($\phi < 5 \times 10^{-3}$) for cyanines and hence is not discussed further.²⁷

Cyanine dyes are one of the most robust classes of fluorescent probes used in the field of biophysics, more so in SM applications and their tunability make them useful for multiple applications.³⁷⁻³⁹ There is a series of cyanine dyes covering the whole visible spectrum changing the length of the polymethine chain. Unique to the cyanine dye class,

two-carbon homologation extends the absorbance maxima in roughly 100 nm increments. The indocarbocyanines, including the broadly utilized Cy3, Cy5, and Cy7 series, form the chemical backbone of many invaluable fluorescent reagents. The solubility of these dyes can also be altered conveniently by choosing the number of sulfonate groups and these variants are commercially available as derivatives for covalent labeling of proteins and nucleic acids.

These dyes have large absorption cross-sections (extinction coefficient exceeding $100,000 \text{ Lmol}^{-1}\text{cm}^{-1}$). They are remarkably photostable, have good quantum yields, and are compatible with existing instrumentation of single-molecule excitation (lasers) and emission (detectors). They also of unique well-studied properties needed for specific techniques; for example, the ability to be switched ‘on’ and ‘off’ by lasers of different frequencies for stochastic optical reconstruction microscopy (STORM) technique.⁴⁰

The low quantum yield of the fluorophore could be because of various non-radiative decay pathways from the excited state to the ground state of the molecule, which competes with the radiative pathway. As discussed in section 1.4, the most prominent non-radiative pathway for cyanine dyes is the ability of an excited-state electron to go from trans (fluorescent form) to cis (non-fluorescent) state which is known as photoisomerization. One way to eliminate this trans-cis photoisomerization is by rigidifying the backbone of the cyanine. This strategy should lead to the elimination of the pathway k_{Nt} as shown in figure 1.4 and equation 1.7, thus, increasing the quantum yield of the selected cyanine dye. This strategy was employed by Michael Cooper et al. in 2004,

applied the rigidization strategy for trimethine cyanine, Cy3BTM.³⁵ The quantum yield improved drastically from Cy3 (0.04) to Cy3B (0.67) in an aqueous solution. This absence of a non-radiative pathway of relaxation was also reflected in the mean fluorescent lifetime of the probe being 2.9 ns for Cy3B from 0.3 for Cy3. Cy3B has helped researchers in many SM techniques, and the popularity of this improved fluorophore inspired us to make better probes in the red region of the spectrum. Chapter 3 and 4 expand this approach on far-red (Cy5) and near-IR (Cy7) cyanines and the photophysical properties of these novel fluorophores will be discussed in detail there.

It is also important to note that other pathways of deactivation of the excited state become more prominent as we move more towards the red part of the spectrum, due to lower energy difference between the excited and the ground state. Further, a similar rigidization strategy was applied to near-infrared heptamethine dye where in contrast to the prior project, it was found that the photoisomerization of heptamethine cyanines does not contribute significantly to the deactivation pathway. In total, these studies clarified the role of photoisomerization on the heptamethine cyanine scaffold and will enable future efforts to optimize NIR dyes for diverse applications. The second part of the chapter will explore the same strategy applied to a near-infrared cyanine dye, Cy7, and how the observations are in contrast with results obtained for Cy5 rigidization; thus giving better insight into deactivation pathways which eventually will pave the way to design of better super-resolution fluorophores.

1.5 Techniques to Quantify Photophysical Properties

There are multiple fluorescent techniques that can be used to quantitate photophysical properties and they will be discussed with the instrumentation needed as well as important parameters while designing the experiment in this section.

A. Quantum Yield Measurement

As mentioned previously, quantum yield (ϕ) is given as the number of photons emitted as fluorescence over a given time, divided by the number of photons absorbed by the molecule. For measurement of absolute quantum yield, one needs to collect all the photons coming out of the sample, which is possible by using an integrating sphere detector.^{41,42}

These detectors are not commonly available in the lab and there is an indirect way to get quantum yield using conventional spectrophotometers. This method is called relative quantum yield which requires the collection of only a fraction of photons coming out as fluorescence. This method relies on a reference molecule whose quantum yield is known and measuring both, reference and given sample in the same conditions, thus having the same fraction of emitted photons measured, allowing the determination of quantum yield of the given sample relative to the other.

As seen in section 1.1, absorbance is given as $\log\left(\frac{I_0}{I(l)}\right) = \epsilon \cdot C \cdot l = A$ and the equation can be rewritten as $I(l) = I_0 10^{-A}$, Thus the intensity of light absorbed can be written as $I_0 - I(l) = I_0 (1 - 10^{-A})$. This gives quantum yield as a ratio of intensity

given as fluorescence divided by the intensity of light absorbed. The ratio of quantum yield leads of sample and reference leads to the final equation as:

$$\frac{\phi_S}{\phi_R} = \frac{I_S}{I_R} \times \frac{1-10^{-A_R}}{1-10^{-A_S}} \times \frac{n_S^2}{n_R^2} \quad (1.8)$$

ϕ = quantum yield, I = emission intensity, A = absorbance, n = refractive index, subscript S = sample, and R = reference.

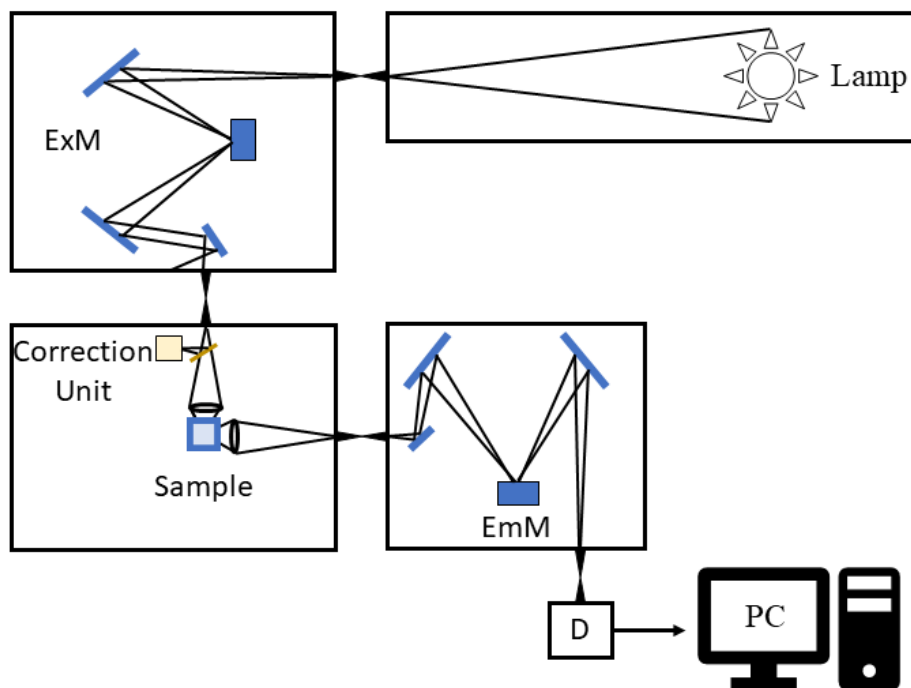


Figure 1.5: Setup for Fluorimeter Used for Steady-State Measurement.

The refractive indices of the solvents should be considered in the equation as they change the solid angle being detected during the measurement. Multiple factors are needed to be considered while doing a relative quantum yield measurement.^{41,43}

The standard sample chosen should ideally absorb and emit in the same spectral region as that of the sample to be quantified. This is because the photon flux of a lamp is wavelength-dependent and while, one can get the corrected signal for this, it is best to avoid a possible factor that can lead to inaccuracies. Thus, having a standard in the same region as the sample does not eliminate the need to use the corrected spectra but minimizes the possibilities of inaccuracies.

A fraction of incident photons gets scattered and when these photons reach the detector and contribute to the signal. The two major types of scattering are elastic and inelastic scattering depending on whether the energy of a photon is conserved or not. Rayleigh scattering is caused by the elastic interaction of light with particles smaller than the wavelength of light. As the energy is conserved, the scattered photons are of the same energy as that of the incident photons and hence, can be avoided by having the excitation wavelength lower than the range of emission wavelengths scanned in the experiment. Raman scattering is caused by the O-H stretching mode of water and the intensity of it goes by λ^{-4} . Thus, the raman scattering is the main concern in the UV and blue end of the spectrum. The raman scattering can be corrected by subtracting the sample spectrum with blank samples to negate the contributions of scattering to the measured fluorescence signals.

Inner filter effect is an artifact in the measurement of fluorescence intensity caused by high concentration and can be manifested in two ways: excitation and emission inner filter effect. The excitation inner filter effect as shown in the figure 1.6 (a) happens when

the intensity of light exposed to the sample changes due to a concentrated solution. If a solution is visualized as a collection of layers, as the light passes through the solution, the

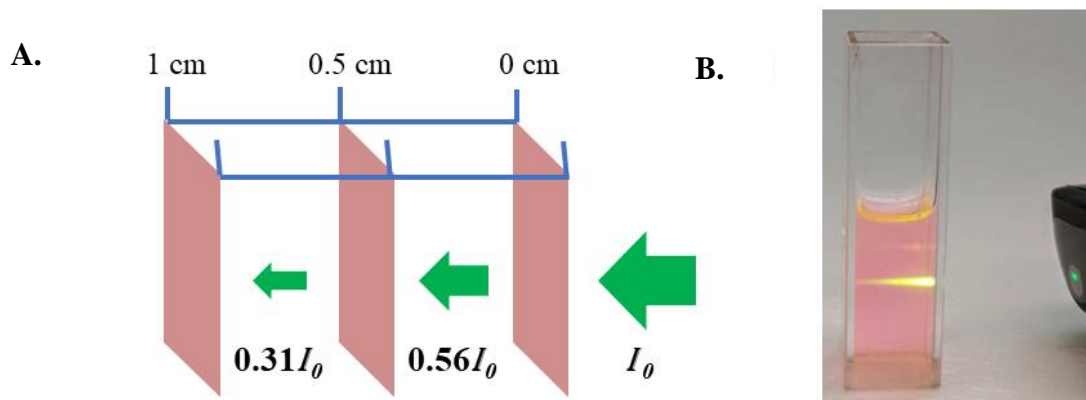


Figure 1.6: Inner Filter Effect. (A) Excitation inner filter effect where the thickness of the green arrow represents the intensity of excitation light, (B) Picture of rhodamine solution with fluorescence (yellow) observed along the path of the laser showing inner filter effect as a decrease in fluorescence going from right to left.

intensity received by each layer is decreased as some part is absorbed by the previous layer.

The detector channel of an instrument is focused to collect most photons from the center of the cuvette. The intensity at 0.5 cm will be $I(0.5) = I_0 10^{-\epsilon \cdot C \cdot 0.5} = I_0 10^{-A/2}$ where A is the absorbance of the solution measured with the standard 1 cm pathlength cuvette.

Therefore, the central part of the cuvette would be excited with an intensity of approximately $10^{-0.25I_0} \approx 0.56I_0$. the quantum yield measured in these conditions would be only about 56% of the value measured for a very dilute solution and a real picture of decrease in fluorescence intensity as the laser passes through more layers of solution and a manifestation of this theory can be seen in a real picture in figure 1.6 (b). Furthermore, an emission inner filter effect can happen when a photon emitted by the molecule is

reabsorbed by a molecule in its path to the detector. This happens due to an area of overlap between absorption and emission spectrum. This reabsorption leads to a decrease in the total number of photons observed and distortion of the spectrum.

Therefore, the fluorescence emission spectrum for the studies was collected for samples with $A \approx 0.05$ to avoid inner filter artifacts. To improve the precision in the determination of A for the calculation of quantum yield, absorbances were measured for solutions displaying $A \approx 0.5$ at the shoulder (i.e. excitation wavelength) of the spectrum and precise 1:10 dilutions were performed before the fluorescence determinations.

B. Lifetime Measurement

Time-correlated single-photon counting (TCSPC) uses a short pulse of light to excite a small number of molecules into the excited state.⁴⁴ Using triggering electronics, emitted photons are then detected and the arrival time of each photon is recorded to generate a histogram. The detailed electronic setup of the instrument is shown in figure 1.7 (a), which essentially has a built-in timer to record the time difference between the laser pulse and emitted photon. The Constant Fraction Discriminator (CFD) is used after the detector to extract precise timing information from the electrical detector pulses that may vary in amplitude. Similar to the detector signal, the sync signal must be made available to the timing circuit to start the timer accurately and hence, a CFD is used here as well. These sync and detector signal from CFD are fed to a Time to Amplitude Converter (TAC). This circuit is essentially a highly linear ramp generator that is started by one sync signal and

stopped by the detector signal. As shown in figure 1.7 (b), the result is a voltage proportional to the time difference between the two signals. The voltage obtained from the

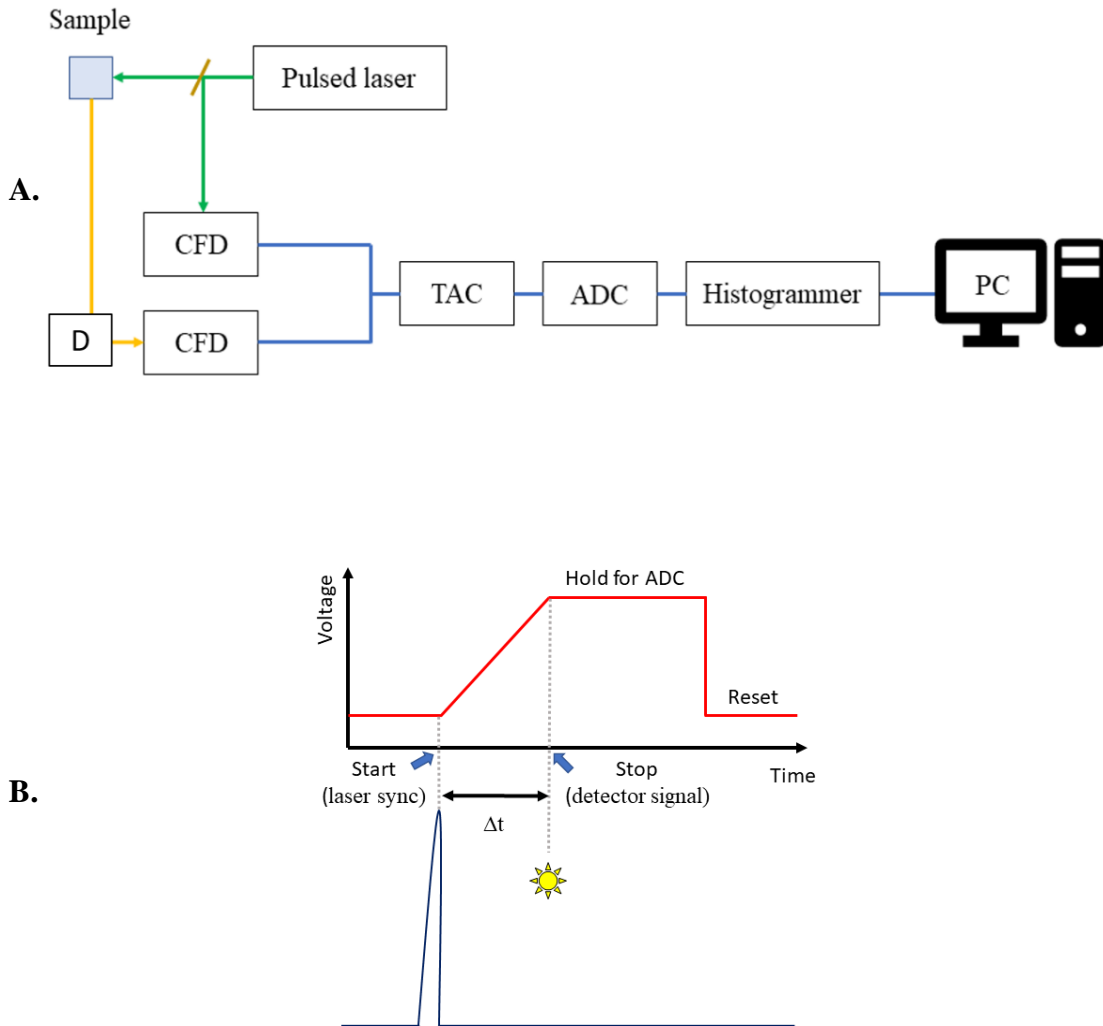


Figure 1.7: Working of TCSPC. (A) TCSPC setup where D detector, CFD = Constant Fraction Discriminator, TAC = Time to Amplitude Converter, ADC = Analog to Digital Converter and PC = Personal Computer, (B) Operation principle of a TAC.

TAC is then fed to an Analog to Digital Converter (ADC) which provides the digital timing value used to generate the histogrammer. Detector and electronics have a “dead” time for

at least some nanoseconds after a photon is detected during which they cannot process another photon coming to the detector. Therefore, if the number of photons occurring in one excitation cycle is greater than 1, the system would very often register the first photon but miss the following ones which lead to over-representation of early photons in the histogram, an effect called ‘pile-up’. Hence, it is crucial to keep the probability of cycles with more than one photon low and hence practically, the average count rate at the detector should be at most 1 to 5 % of the excitation rate.⁴⁵

Another important term to keep in mind is overall timing precision of the instrument, known as instrument response function (IRF). In ideal terms, infinitely sharp excitation pulse and infinitely accurate detectors and electronics would give rise to an infinitely narrow IRF. However, IRF generally is broader due to the convolution of multiple IRF sources such as laser source not having a delta function output, detectors having a finite accuracy, and the timing jitter of the electronic components.

Once collected, the histogram (lifetime decay) can be fitted to extract the lifetime. The rate of change of excited population (n^*) is described by:

$$\frac{dn^*(t)}{dt} = -k_{all}n^*(t) \quad (1.9)$$

where k_{all} is the rate constant of deactivation of the excited state via all the possible routes. $k_{all} = k_f + k_{nr}$ where subscript f is for fluorescence and nr is for all other non-radiative processes. The integration of this differential equation gives $n^*(t) = n_0 e^{-k_{all}t}$ which can be rewritten in terms of a lifetime as:

$$n^*(t) = n_0 e^{-t/\tau_{all}} \quad , \text{ where } k_{all} = \frac{1}{\tau_{all}} \quad (1.10)$$

The equation can be rewritten as $\tau_{all} = \frac{1}{k_f + k_{nr}}$, As k_f is practically constant for a given fluorescent molecule, the environment dependence of the lifetime for a given fluorophore comes from a change in k_{nr} depending on the environment.

There might be multiple population corresponding to different environment the fluorophore is experiencing, and each environment will have a specific lifetime. Un that case, the decay can be represented as sum of exponentials which can help in finding different populations in the sample. The components in the exponential fit indicate different populations of the molecular environment.

$$I(t) = A \sum_{i=1}^n \alpha_i e^{-t/\tau_i} \quad (1.11)$$

where n is the minimum number of terms that result in random residuals, A is a fitted amplitude, and α_i ($\sum_{i=1}^n \alpha_i = 1$) is the relative weight of the individual lifetime, τ_i . Intensity decays were fitted using ASUFIT, a MATLAB-based program developed at ASU (<http://www.public.asu.edu/~laserweb/asufit>) that uses a standard reconvolution procedure and nonlinear regression. Average lifetime $\langle \tau \rangle$ is calculated as $\langle \tau \rangle = \sum_{i=1}^n \alpha_i \tau_i$. The goal is to minimize the sum of squared differences between the simulated convolution and the experimentally measured decay. The goodness of the fit was judged by the χ^2 value and the randomness of the residuals which is mathematically given as:

$$\chi^2 = \sum_{i=1}^n \frac{1}{\sigma_i^2} [N(t_i) - I(t_i)]^2 \quad (1.12)$$

where $N(t)$ is the experimentally measured decay, $I(t)$ is the experimental decay, and $1/\sigma^2$ is the weight (reciprocal of the variance). Indicators of a good fit are a low χ^2 and randomness of the residuals.

One other important thing to keep in mind is emission monochromators having a polarization bias i.e. either horizontally or vertically oriented fluorescence will be transmitted more efficiently than the other orientation. Therefore, a special condition called the magic angle condition must be used so that the collected emission is proportional to the total emission. In the magic angle condition, the sample is excited with vertically polarized light (0°), and the emission is collected at the magic angle (54.7° with respect to the vertical direction).

C. Pump-Probe Measurement

Pump-probe method, laser flash photolysis, or transient absorption (TA) spectroscopy is used to detect the presence of non-fluorescent transient states with a lifetime longer than fluorescence. The principle of this technique lies in the fact that these transient states also absorb light. The sample under study is illuminated with a pulsed laser or pump, which excites the transient species into higher energy transient states. By measuring the absorption of the sample before and after the initial laser pulse one can detect the presence of these transient species. The change in absorbance ($\Delta A(\lambda)$) after the sample is excited with a pulsed laser is then plotted to see the dynamics of depletion of this transient state.

The schematic of the instrument is shown in figure 1.8. The probe source is generally a broad-spectrum lamp such as a xenon lamp, which allows to get an absorption spectrum in a wide wavelength range and allowing to monitor many wavelengths to find the absorbing transient. The instrument consists of a pulsed laser or pump operating at a repetition rate greater than the fluorescence lifetime. This pump laser is set at the maximum absorption wavelength of the sample and set at a high intensity such as to get a higher population of the excited state. One more way to increase the population of excited states and get a strong transient signal is to use concentrated solutions with $A > 1$. As described in the excitation inner filter effect section, the population of excited molecules decreases with the laser beam's distance inside the sample for a concentrated solution. Thus, the beam from the pump lamp must overlap the excitation beam (probe) closest to its entrance to maximize the transient signal. A set of filters can be placed after the probe lamp to select the wavelength range required for the transient spectrum. A neutral density filter can be used as well to control the intensity of the beam. A monochromator is used after the sample to select the monitoring wavelength and to reject the excitation laser (pump) wavelength. Lenses are used to focus the lamplight into the cuvette and then the monochromator slit. A photodetector is used to collect the signal which is then displayed on an oscilloscope and finally passed to a computer for analysis. In cases where the intensity coming from the monochromator can saturate the photodetector, an attenuator is used to decrease the magnitude of the intensity. The signal observed in TA spectroscopy is a difference between the absorption of the transient state before and after the excitation pulse and an example of such study will be seen in chapters 2 and 4.

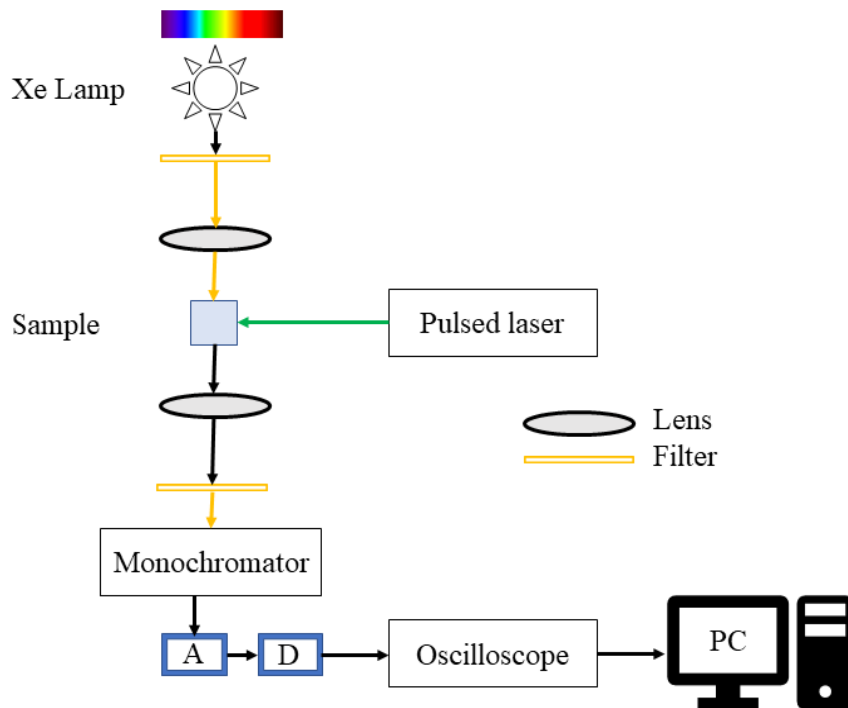


Figure 1.8: Schematic of TA Setup. “A” represents the attenuator and “D” represents the detector.

The data collected is 2-dimensional as it may be studied at either fixed time or fixed wavelength. Thus, a spectrum can be observed at a given time after the excitation to detect the presence of transient species in a different region of the spectrum. As the transient state relaxes back to the ground state, the population that may be excited to higher energy transient states decreases. Therefore, the change in intensity after the laser pulse can be plotted with respect to time and the depletion curve can help in determining the species present in the sample.

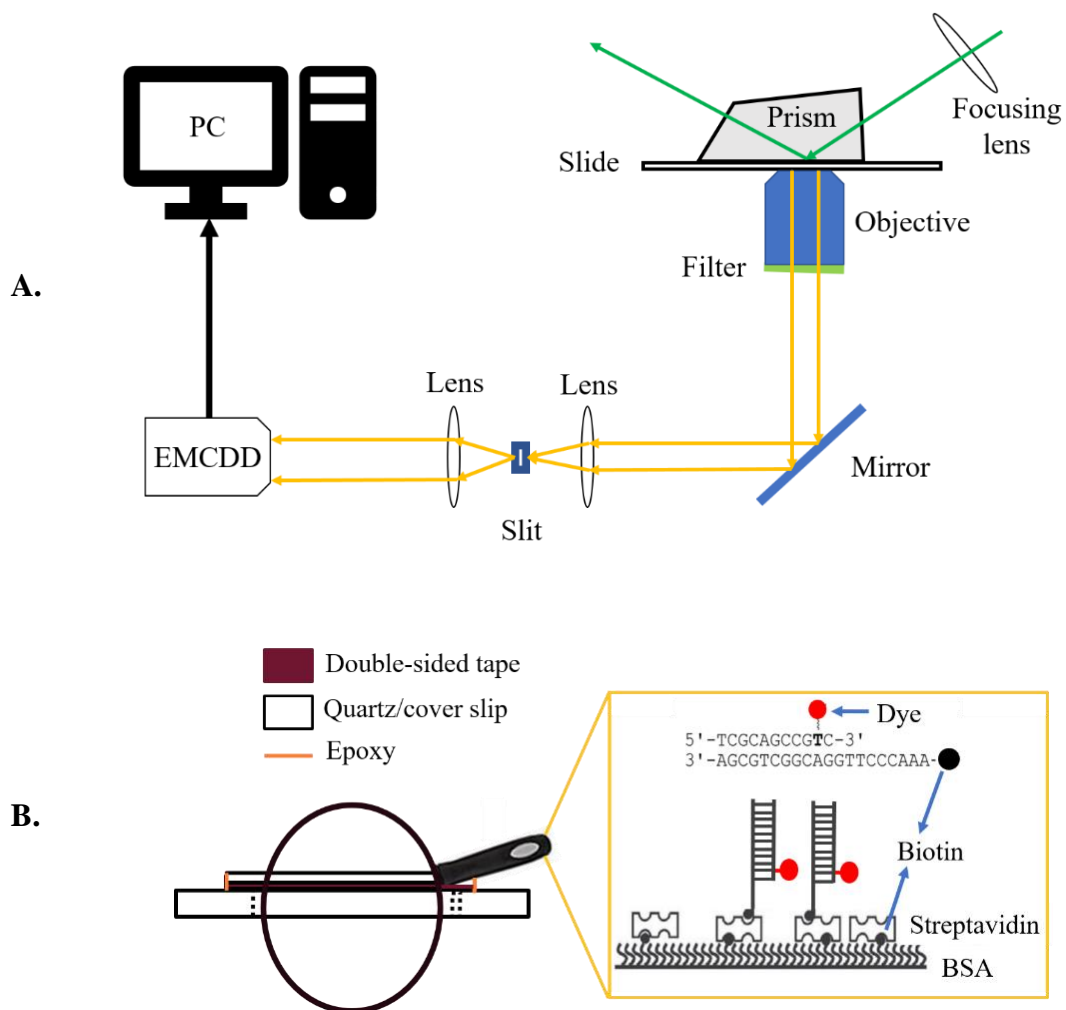


Figure 1.9: TIRF Setup and Slide Preparation. (A) Setup of TIRF instrument, (B) Schematic of the slide chamber with a zoomed-in image of the surface of the slide.

D. Total Internal Reflection Fluorescence (TIRF) Measurement

A total internal reflection fluorescence (TIRF) is used in chapter 2 to study the dynamics of dye-DNA interaction. TIRF is a single-molecule setup that allows looking at individual dye tagged with DNA. This is achieved by adjusting 2 parameters; illuminating just the surface of the slide rather than the whole slide (as in epifluorescence microscopy)

and by adjusting the density of dye-DNA conjugate on the surface of the slide. The setup of a home-built TIRF setup and the sample system is shown in figure 1.9 (a).

The dye being studied has excitation in the red and hence a laser of 639 nm was used in the setup. The angle at which the incident beam hits the sample chamber can be adjusted by changing the angle of excitation optics. The total internal reflection happens at an angle where the light starts reflecting, instead of refracting at the interface between two materials with different refractive indices. The incident angle for which this total internal reflection can be achieved is dictated by Snell's law as $\theta_c = \sin^{-1}\left(\frac{n_1}{n_2}\right)$ where θ_c is the critical angle at which light needs to be incident to get total internal reflection going from medium 1 to medium 2 with different refractive indices n_1 and n_2 respectively.

The total internal reflection creates an evanescent field between medium 1 (quartz) and 2 (water) which illuminates the surface of the sample chamber. This exponentially decaying intensity generally has a depth in the range of 200 nm which is enough to illuminate just the inner surface and a sample can be observed by immobilizing the DNA to the surface by conjugation or bridging chemistry. A commonly used strategy for immobilizing is used in this study where a solution of biotin-BSA (bovine serum albumin) is flown in the chamber followed by streptavidin, which has 4 binding sites for biotin. A dye-DNA conjugate, modified with biotin on the 5' end is flown in next to attach the DNA to the streptavidin, thus immobilizing it on the surface (figure 1.9 (b)). The chamber is washed with buffer after each step to avoid any non-specific binding on the surface. The fluorescence after excitation is collected using a water immersion objective with 60 X

magnification and numerical aperture of 1.20 followed by an emission filter to eliminate any excitation laser intensity from the signal. A large mirror follows to collect all the fluorescence coming from the objective and optical components are used to focus the image onto the photoactive area of electron-multiplying charged coupled device camera (EMCCD) chip which is connected to the computer. Acquisitions are done over a time range which is larger than the timescale of photobleaching of fluorophore (more than 100 seconds). These acquisitions or movies can then be analyzed to understand the dynamics of the system under study and chapter 2 will cover how such data can be used to identify different states and the dwell times.

1.6 Scope and Contribution

Chapter 2 investigates a relatively new class of hemicyanine called Dy dyes (part of DyLight Fluor dye family sold primarily by Dyomics GmbH Germany), Dy630, and Dy632, and evaluates their potential as red-absorbing PIFE probes. An in-depth study is conducted to evaluate the photophysical properties of free dye as well as when placed on DNA which makes a dye good PIFE probe. The experimental data and analysis were done by the author and Dr. Monika Ciuba who contributed equally to the publication. This study highlights results that shed light on the optimal design principles for ideal probes for PIFE applications, opening up new avenues for the technique's broad applicability in biophysical studies.

Chapter 3 is a collaborative work between multiple labs led by Dr. Martin J. Schnermann where the goal is to find a novel fluorophore in the far-red region of the

spectrum for super-resolution imaging. This fluorophore is expected to have a better brightness than the existing pentamethine variant, as it is designed to eliminate a major non-radiative process caused by photoisomerization. The author is a secondary author in this paper and their role is to capture the spectroscopic properties of the novel fluorophore in comparison with the parent pentamethine in different solvents and temperatures. The photophysical characterization of this newly synthesized dye elicits the rigidity of the molecule as contributing to the circumvention of non-radiative decay, thus, improving brightness.

In Chapter 4, a similar rigidization strategy was applied to near-infrared heptamethine dye where in contrast to the prior project in chapter 3, it was found that the photoisomerization of heptamethine cyanines does not contribute significantly to the deactivation pathway. The author is a primary coauthor in this paper and conducted the photophysical characterization of the novel and parent heptacyanine to elucidate non-radiative pathways present in this class of dye and the contribution of photoisomerization to the brightness.

Chapter 5 is an ongoing work which aims to answer the fundamental question of how the physics of DNA can impact its biological function. The relationship of the local sequence context with local DNA flexibility and repair efficiency of base-flipping DNA repair proteins such as UDG is being studied using DNA base analog 2-AP. This project hypothesizes that UDG activity is dictated by the intrinsic local deformability of the DNA sequence around the uracil. Specifically, sequences that maintain uracil in a rigid DNA

context should be a poorer substrate for UDG. To test these hypotheses, fluorescence, nuclear magnetic resonance (NMR) measurement of nucleotide dynamics and molecular dynamics (MD) simulations will be combined with collaborations with Dr. Wade Van Horn (NMR) and Dr. Arjan Van Der Vaart (Computational work).

CHAPTER TWO

METHODS AND APPLICATIONS IN FLUORESCENCE

“PHOTOPHYSICAL PROPERTIES OF THE HEMICYANINE DY-630 AND ITS POTENTIAL AS A SINGLE-MOLECULE FLUORESCENT PROBE FOR BIOPHYSICAL APPLICATIONS”

2.1 Abstract

Protein-induced fluorescence enhancement (PIFE) is an increasingly used approach to investigate DNA-protein interactions at the single molecule level. The optimal probe for this type of application is highly photostable, has a high absorption extinction coefficient, and has a moderate fluorescence quantum yield that increases significantly when the dye is in close proximity to a large macromolecule such as a protein. So far, the green-absorbing symmetric cyanine known as Cy3 has been the probe of choice in this field because the magnitude of the increase observed upon protein binding (usually 2–4 –fold) is large enough to allow for the analysis of protein dynamics on the inherently noisy single-molecule signals. Here, we report the characterization of the photophysical properties of the red-absorbing hemicyanine dye Dy-630 in the context of its potential application as a single-molecule PIFE probe. The behavior of Dy-630 in solution is similar to that of Cy3; the fluorescence quantum yield and lifetime of Dy-630 increase with increasing viscosity, and decrease with increasing temperature indicating the existence of an activated nonradiative process that depopulates the singlet state of the dye. As in the case of Cy3, the results of transient spectroscopy experiments are consistent with the formation of a

photoisomer that reverts to the ground state thermally in the microsecond timescale. Unfortunately, experiments with DNA samples paint a more complex scenario. As in the case of Cy3, the fluorescence quantum yield of Dy-630 increases significantly when the dye interacts with the DNA bases, but in the case of Dy-630 attachment to DNA results in an already long fluorescence lifetime that does not provide a significant window for the protein-induced enhancement observed with Cy3. Although we show that Dy-630 may not be well-suited for PIFE, our results shed light on the optimal design principles for probes for PIFE applications.

2.2 Introduction

Advances in single-molecule fluorescence detection over the last fifteen years have opened up the possibility of investigating unprecedented dynamic aspects of biological molecules.⁴⁷⁻⁵³ Among its many applications, single-molecule fluorescence experiments have been successfully used to investigate the dynamics of proteins that translocate or diffuse along nucleic acids.⁵⁴⁻⁵⁶ A common approach for these studies is single-molecule Förster resonance energy transfer (sm-FRET), where a donor and an acceptor fluorescent probe are attached to the protein and the nucleic acid, and their fluorescence intensities are monitored continuously as a function of time.⁵⁷⁻⁵⁹ FRET efficiency increases as the protein approaches the fluorescent label placed on the nucleic acid, and the analysis of the temporal intensity fluctuations of both the donor and acceptor yields information about translocation or diffusion rates. The main drawback of this approach is the need for labeling the protein, which in general requires mutagenesis to place a unique cysteine in the location of interest.

This can be costly and time-consuming, and even if successful, may result in impaired activity due to the mutation itself or the presence of the fluorophore.

There is, therefore, an increasing interest in single-molecule fluorescence approaches that do not involve protein labeling. This requires that the fluorescent label on the nucleic acid is sensitive to the proximity to the protein, so that diffusion or translocation of the protein along the nucleic acid (i.e. changes in the protein-label proximity) result in changes in the fluorescent intensity of the probe. In this way, the temporal behavior of the fluorescence intensity fluctuations of the probe can be analyzed in terms of the rates of translocation or diffusion of the protein on the nucleic acid. This strategy was first used in a single-molecule study of the translocation of the protein RIG-I along dsRNA.⁶⁰ The intensity of the fluorescent dye Cy3 (Fig. 2.1B) was shown to increase in a distance-dependent fashion when the protein was within c.a. 3 nm from the nucleotide containing the fluorescent label. This phenomenon has been dubbed protein-induced fluorescence enhancement (PIFE),⁶¹ and used in various studies of motor proteins that move along DNA or RNA.⁶²⁻⁷⁰ The increasing number of publications using this approach suggests that the strategy is gaining momentum as an attractive single-molecule approach to investigate a large variety of DNA-protein dynamic interactions.⁶⁰⁻⁷⁸ The dye Cy3 has been the dye of choice for this type of single-molecule studies due to its high extinction coefficient, photostability, and modest quantum yield. While a high fluorescence quantum yield is usually a desirable property in single-molecule research, the optimum PIFE dye has large extinction coefficient but only a modest quantum yield in the absence of the protein so that the brightness is sufficient for single-molecule detection before protein binding, but low

enough to provide a significant dynamic range for increase when the protein is bound in close proximity. The fluorescence quantum yield of Cy3 free in solution is $\phi_F = 0.09$, and $\phi_F \sim 0.2$ when bound to DNA (depending on sequence, secondary structure, etc.).⁷⁹ Because the extinction coefficient of the dye is remarkably large for a green-absorbing fluorophore ($\epsilon = 150,000 \text{ M}^{-1} \text{ cm}^{-1}$),⁸⁰ the modest quantum yield of $\phi_F \sim 0.2$ is sufficient to provide excellent brightness for single-molecule experiments and in fact, Cy3 has been a long-time favorite in the single-molecule field.⁵⁶ The fluorescence intensity of Cy3 bound to DNA has been observed to increase by a factor of 2-2.5 and as much as 4 in experiments where a protein is bound in close proximity to the dye.³⁵ An increase of this magnitude is needed to allow for the analysis of the inherently noisy single-molecule trajectories in terms of changes in dye-protein proximity.

The photophysical properties of symmetric cyanine dyes such as Cy3 have been investigated for decades.^{79,82-87} The influence of solvent viscosity on the fluorescence quantum yield of these dyes has been interpreted in terms of a potential energy surface that describes the photoisomerization of the cyanine in the excited state.^{82,85,88} Following light absorption, the singlet-excited state deactivates by competing processes, including fluorescence and rotation around a C-C bond of the polymethine chain (photoisomerization). Photoisomerization is the most efficient non-radiative decay pathway, and therefore the efficiency of bond rotation in the excited state determines the fluorescence quantum yield of the dye. The main influence of the solvent in the isomerization pathway is through a viscous force that hinders the rotation of the C-C bond. As a consequence, an increase in solvent viscosity decreases the efficiency of

photoisomerization and results in an increase in the lifetime of the singlet excited state and the fluorescence quantum yield.⁸²⁻⁸⁶ The excited state of the trimethine cyanine dyes (e.g. Cy3) in fluid solution is characterized by a short lifetime and a low quantum yield due to very efficient isomerization in the excited state. This efficiency has been shown to decrease when bond rotation is sterically hindered by interactions with biomolecules; the fluorescence quantum yield of Cy3 increases when bound to DNA, and a further increase is observed when a protein binds to the DNA in the proximity of the dye.^{79,89-92} Indeed, our study of Cy3 photophysics using complexes of DNA and Klenow fragment (a protein) demonstrated that the enhancement of Cy3 fluorescence due to the protein (PIFE) correlates with a decrease in the efficiency of photoisomerization and occurs in conditions in which the dye is sterically constrained by the protein.⁹²

So far, single-molecule applications of PIFE have been limited to Cy3 because no other photostable single-molecule probe displays such marked protein-dependent changes in fluorescence quantum yield. The research described in the present manuscript is part of our ongoing efforts to expand the palette of options for single-molecule PIFE, especially in the red region of the spectrum where scattering and autofluorescence are reduced. The pentamethine symmetric cyanine Cy5 (Fig. 2.1B) would appear as an obvious candidate for a red-absorbing PIFE probe, but the increase in fluorescence intensity upon protein binding has been shown to be significantly lower than that observed for Cy3 under otherwise identical conditions.⁶¹ This is not surprising given that the quantum yield of bond rotation from the singlet excited state is significantly higher for the trimethine cyanines than for their pentamethine counterparts.^{79,82} The higher efficiency of photoisomerization

of the shorter cyanines results in a lower singlet state lifetime in fluid solution, and a more pronounced environmental sensitivity towards factors that restrict bond rotation. For example, the quantum yield of Cy3 is 13 times higher in glycerol than in water at room temperature, but the increase observed for Cy5 is only 1.4-fold.⁸⁰ Covalent attachment of Cy3 to antibodies was reported to result in a 3-fold increase in quantum yield, while the change for Cy5 was negligible.⁹³ The fluorescence properties of the red-absorbing symmetric carbocyanines such as Cy5 are therefore not sensitive enough to viscosity and steric interactions to make these dyes useful as PIFE single-molecule probes.

In this manuscript we report the photophysical characterization of the hemicyanine dye Dy-630⁹⁴ (Fig. 2.1C) in the context of its potential use as a red-absorbing dye for single-molecule PIFE applications. Although this dye resembles Cy5 in its spectral properties, its photophysical properties are closer related to those of the green-absorbing cyanine Cy3. For example, the fluorescence lifetime of Dy-630 in aqueous solution was reported as $\tau_F = 0.2$ ns,^{94,95} which is almost the same as Cy3 ($\tau_F = 0.18$ ns)⁸⁹ and significantly shorter than the corresponding value for the red-absorbing symmetric cyanine Cy5 ($\tau_F = 0.91$ ns).⁹⁵ The lifetime of Dy-630 covalently bound to the protein BSA is $\tau_F = 2.6$ ns,⁹⁶ a value that represents a 13-fold increase with respect to the value measured for the dye in aqueous buffer. Fluorescence lifetimes in 40% glycerol are 1.39 ns for Cy5 and 0.62 ns for Dy-630, which represent 1.5-fold and 3-fold increases with respect to the values measured in water, respectively.⁹⁵ Similarly, the average lifetimes of Cy5 and Dy-630 conjugated to biotin increase by 1.7-fold and 3.1-fold when streptavidin (a large protein) binds to the biotin moiety, respectively.⁹⁵ These published observations suggest the

existence of an efficient non-radiative channel for the deactivation of the excited state of Dy-630 that, as in the case of Cy3, results in fluorescence quantum yields and lifetimes that are very sensitive to viscosity and steric interactions with proteins. Here, we report the photophysical characterization of Dy-630 in solution and on DNA, and discuss its potential use as a red-absorbing dye for PIFE applications.

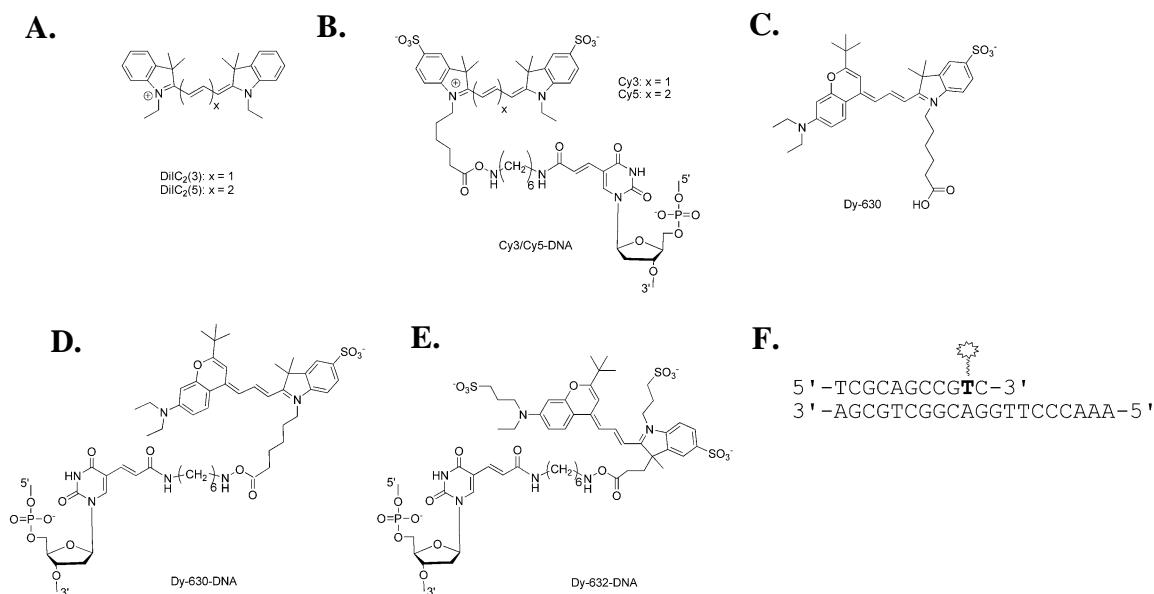


Figure 2.1: Chemical Structures of Dyes Used. (A) Symmetric cyanines DiIC₂(3) and DiIC₂(5). (B) Cy3 and Cy5 bound to DNA. (C) Asymmetric cyanine Dy-630. (D) and E Dy-630 and Dy-632 bound to DNA. (F) DNA sample. T represents a modified thymine covalently bound to a fluorescent dye as shown in panels B, D, and E.

2.3 Methods

A. Materials and Chemicals

Dy-630 (carboxylic acid, Fig. 2.1C) was purchased from Sigma-Aldrich (CAS Number: 375395-99-6). The following DNA nucleoside monophosphates (dNMPs) were purchased from Sigma-Aldrich (St Louis, MO): 2'-deoxyadenosine 5'-monophosphate (dAMP), 2'-deoxycytidine 5'-monophosphate sodium salt (dCMP), 2'-deoxyguanosine 5'-

monophosphate sodium salt hydrate (dGMP), and thymidine 5'-monophosphate disodium salt hydrate (dTMP). DiIC₂(5) was a gift of Dr. Martin J. Schnermann (Laboratory of Protein Dynamics and Signaling, NIH). DiIC₂(3) (1,1'-Diethyl-3,3,3',3'-tetramethylindocarbocyanine iodide) was purchased from Sigma-Aldrich (St. Louis, MO).

The following DNA strands were purchased from IBA GmbH (Germany): 5'-TCGCAGCCG**T**C-3' (primer), 5'-/AAACCCTTGGACGGCTGCGA-3' (template) and 5' biotin/AAACCCTTGGACGGCTGCGA-3' (biotinylated template). The bold case T represents the fluorescently labeled modified thymine shown in Fig. 2.1. The biotinylated template was used to prepare the DNA samples used in the single-molecule experiments. To prepare the DNA samples, the primer strand was mixed with 1.25 equivalents of template strand in 10 mM TRIS buffer (pH = 7.4), heated to *c.a.* 90°C for 5 minutes, and slowly cooled down to room temperature. Klenow fragment (KF) was purchased from New England Biolabs (KF exo⁻, catalog number M0212M, Ipswich, MA). The concentration of KF was calculated from the specific activity provided by the suppliers as 77 μM. DNA-KF complexes were prepared by mixing 1 μM of the primer/template DNA with 1.25 equivalents of KF in the buffer supplied by New England Biolabs (NEBuffer 2, 10 mM Tris-HCl, 50 mM NaCl, 10 mM MgCl₂, 1 mM DTT, pH 7.9 at 25°C). Samples were allowed to equilibrate for 30 min. on the bench before experiments. The residual concentration of glycerol (from the enzyme storage buffer) was less than 4% in all cases.

B. Absorption and Steady-State Fluorescence Spectroscopy

Absorption spectra were acquired using a Shimadzu UV-1700 PharmaSpec UV-VIS spectrophotometer. Steady-state fluorescence spectra were acquired on a PTI Quantamaster 4/2005SE spectrofluorimeter. Samples were contained in semi-micro quartz cells with a 10 x 4 optical path length. For the fluorescence experiments, the temperature was controlled using a water circulator. Temperature was measured inside the cuvette with a thermocouple. Emission scans were corrected for wavelength-dependent detector responsivity using correction curves determined with a calibrated light source.

Fluorescence quantum yields (ϕ_F) were determined using reference standards as $\phi_F = \phi_{F,R} \frac{I (1-10^{-A_R}) n^2}{I_R (1-10^{-A}) n_R^2}$, where the subscript R refers to the standard used as a reference, I represents the integrated corrected fluorescence spectrum, A is the absorbance of the solution at the excitation wavelength used to determine I , and n is the refractive index of the solvent. Absorbances at the excitation wavelength (typically the shoulder of the absorbance spectrum) were kept around $A \sim 0.05$ in all fluorescence experiments to avoid inner filter artifacts. To improve the precision in the determination of A for the calculation of ϕ_F , absorbances were measured for solutions displaying $A \sim 0.5$ at the shoulder of the spectrum and precise 1:10 dilutions were performed before the fluorescence determinations. This method results in significantly more reproducible results compared to the direct measurement of the low absorbance values ($A < 0.1$) of the dilute solutions needed in the fluorescence experiments. The standards used in each case are listed in the captions of Tables 2.1 and 2.2. Excitation wavelengths for the quantum yield

determinations were 510 nm (Cy3 and DiIC₂(3)) and 590 nm (Cy5, Dy-630, Dy-632 and DiIC₂(5)).

C. Time-Resolved Fluorescence Spectroscopy

Time-resolved fluorescence decays were acquired using a Time-Correlated Single Photon Counting (TCSPC) setup. The excitation light was a Fianium supercontinuum laser (SC-450-4-PP) operating at 20 MHz equipped with an Acousto-Optic Tunable Filter (AOTF) to select the excitation wavelength. A polarizer in the excitation pathway was used to excite the sample with vertically-polarized light. Samples were contained in semi-micro quartz cells with a 10 x 4 optical path length. The emission polarizer was set at the magic angle (54.7° with respect to the excitation) for the lifetime measurements and to 0° and 90° for the anisotropy measurements. The detector was a Hamamatsu MCP-PMT R3809U-50 photomultiplier tube and data was recorded with a Becker and Hickl TCSPC Timing Card (B&H SPC830). The instrument response function (IRF) was measured by scattering excitation light off a 3% Ludox solution. Fluorescence intensity decays were analyzed in terms of equation 1:

$$I(t) = A \sum_{i=1}^n a_i e^{-t/\tau_i} \quad (2.1)$$

Where n is the minimum number of terms that result in random residuals, A is a fitted amplitude, and a_i ($\sum_{i=1}^n a_i = 1$) is the relative weight of each individual lifetime, τ_i . Intensity decays were fitted using ASUFIT, a MATLAB-based program developed at ASU (<http://www.public.asu.edu/~laserweb/asufit>) that uses a standard reconvolution procedure

and nonlinear regression. The goodness of the fit was judged by the χ^2 value and the randomness of the residuals.

D. Single-Molecule Fluorescence

A home-made total internal reflection single-molecule instrument (TIRF) was used to acquire single-molecule traces of Dy-630-DNA, Dy-632-DNA and Cy5-DNA. A CUBE 639 nm 40 mW laser (Coherent Inc, Santa Clara, CA) was used as the excitation source. The laser was guided by mirrors to the sample stage, where it was focused by a plano convex lens onto the flat side of a Pellin Broca fused silica prism (Eksma Optics, Lithuania). The prism rested on top of a sample chamber which was placed on top of a UPLSAPO 60XW water immersion objective (60x, 1.20 NA, Olympus Corp.). The emitted light collected by the objective was passed through an emission filter and a mechanical slit, and then focused onto the photoactive area of an Andor iXon Ultra 897 EMCCD camera (Andor Technology, Belfast, UK).

Sample chambers were prepared from quartz slides and borosilicate glass coverslips using double-sided tape as a spacer. Chambers were sealed using epoxy adhesive. DNA molecules were immobilized at the surface of the quartz slide as follows. A 1 mg/mL solution of biotin-BSA in 1X T50 buffer (10 mM TRIS pH 8.0, 50 mM NaCl) was flowed into the sample chamber and incubated for 20 min. The sample chamber was then flushed with excess 1X T50 buffer, and a 0.2 mg/mL solution of streptavidin was flowed into the chamber and incubated for 2 min. The chamber was flushed again with excess buffer, and the biotinylated DNA samples (10 pM in 1X T50 buffer) were flowed

in, incubated for 2 minutes, and then rinsed with excess buffer. Finally, an imaging buffer consisting of 1X T50 buffer with 2 mM Trolox, 0.8% glucose, and 1 μ L of glucose oxidase per 100 μ L of solution was flushed in. Fresh imaging buffer was flushed into the chamber every 20 – 30 minutes.

Single-molecule images were acquired with 100 ms time resolution. The iSMS software⁹⁷ was used to localize molecules, calculate background, and produce the intensity trajectories. The vbFRET package implemented in MATLAB⁹⁸ was used to calculate the idealized traces used to determine dwell times.

2.4 Results and Discussion

The terms “Cy-dyes” are commonly used to designate different derivatives of the symmetric indotricarbocyanines and indopentacarbocyanines (Fig. 2.1). Unfortunately, the terms Cy3 and Cy5 are often used for both the sulfonated and non-sulfonated molecules, which are not chemically identical compounds. To avoid confusion, in this work we use the terms Cy3 and Cy5 only for the sulfonated derivatives of the dyes, and the common historical names diIC₂(3) and diIC₂(5) for the nonsulfonated cyanines (Fig. 2.1).

A. Absorption and Emission Properties of Dy-630

The absorption and emission maxima of Dy-630 in ethanol are almost the same as the corresponding values for the symmetric pentamethine cyanine diIC₂(5) (Fig. 2.10 and Table 2.1). However, unlike diIC₂(5), Dy-630 has an additional absorption band around 470 nm which makes this dye compatible with the 488 nm line of the argon ion laser.⁹⁴ The

steady-state fluorescence anisotropy values of Dy-630 in glycerol at 7°C are negative when the sample is excited at the blue band, with a fundamental fluorescence anisotropy close to $r_0 = -0.1$ (Fig. 2.11). This value indicates that the orientation of the transition dipole moment of the 470 nm-band is displaced by about 66° with respect to the transition dipole moment of the main absorption band.

Dy-630 is more prone to aggregation in water than diIC₂(5). The dye self-associates in water at high micro-molar concentrations, as evidenced by a blue-shifted absorption band that increases with increasing dye concentration and is absent in the spectrum measured in ethanol (Fig. 2.12). No signs of aggregation were observed for diIC₂(5) in water at the same concentrations, or for either dye in ethanol (Fig. 2.12).

Fluorescence quantum yields and fluorescence lifetimes were determined at room temperature in a variety of solvents as described in Materials and Methods. The fluorescence quantum yield and lifetime of Dy-630 depend strongly on solvent viscosity (η), as is the case for diIC₂(3) and other symmetric trimethine cyanines, and to a lesser extent for diIC₂(5) and other pentamethine cyanines (Fig. 2.2A and Table 2.1).^{82-85,99} The quantum yield of Dy-630 in ethanol at room temperature was determined as $\phi_F = 0.082$, a fraction of the corresponding value for the red-absorbing symmetric cyanine diIC₂(5) ($\phi_F = 0.18$). While the fluorescence quantum yields of all dyes are significantly higher in glycerol ($\eta = 934$ cp) than in ethanol ($\eta = 1.07$ cp), the increase observed for Dy-630 (6.2-fold) is much more pronounced than the value measured for diIC₂(5) (1.3-fold), and similar to the increase observed with the green-absorbing symmetric cyanine diIC₂(3) (8.3-fold).

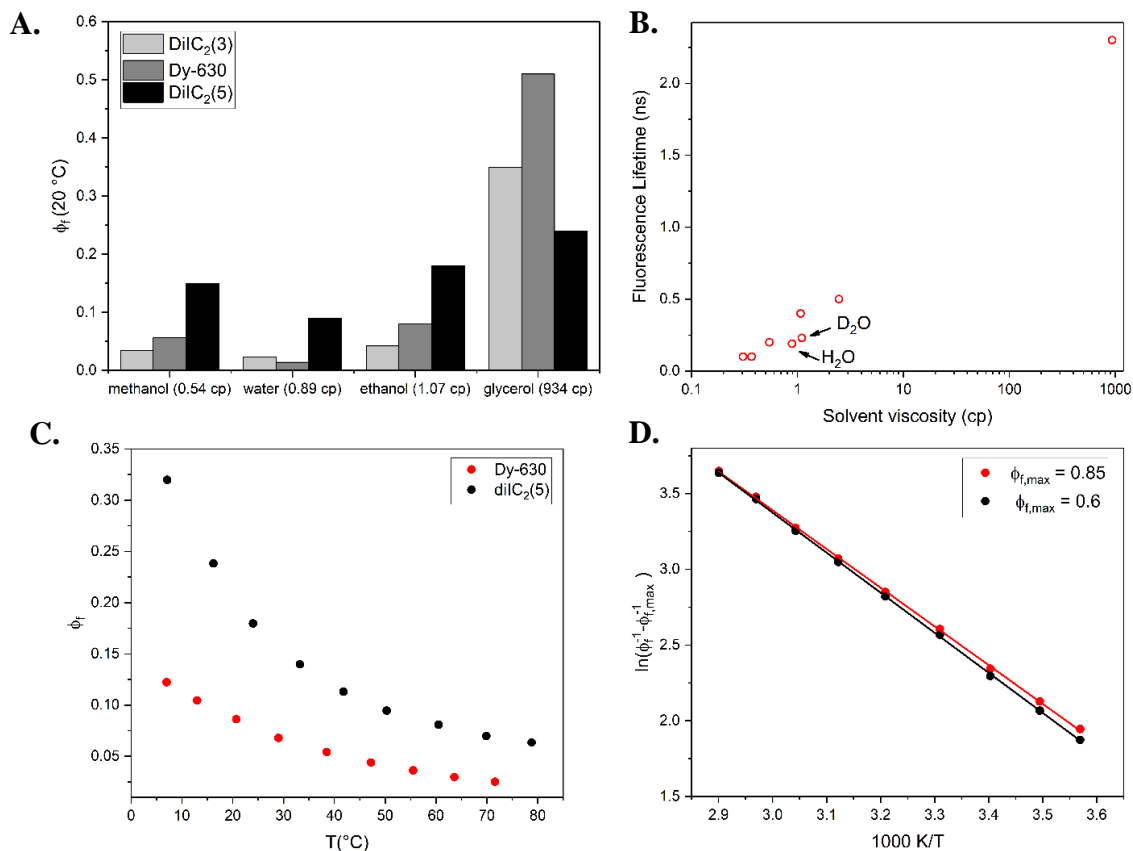


Figure 2.2: Photophysical Properties of Dyes. (A) Fluorescence quantum yield (ϕ_F) of DiIC₂(3), Dy-630, and DiIC₂(5) at room temperature in methanol, water, ethanol and glycerol (see also Table 2.1). Values in water are lower than predicted on the basis of solvent viscosity (see text). (B) Fluorescence lifetime of Dy-630 in solvents of increasing viscosity (η): acetone ($\eta = 0.306$ cp)¹⁰², acetonitrile ($\eta = 0.369$ cp)¹⁰², methanol ($\eta = 0.544$ cp)¹⁰², water ($\eta = 0.89$ cp)¹⁰³, ethanol ($\eta = 1.07$ cp)¹⁰², D₂O ($\eta = 1.10$ cp)¹⁰³, 50 % ethanol in water ($\eta = 2.46$ cp),¹⁰⁴ and glycerol ($\eta = 934$ cp)¹⁰². The abscissa is plotted in logarithmic scale for clarity. (C) Fluorescence quantum yield of Dy-630, and DiIC₂(5) in ethanol as a function of temperature. (D) Dy-630 quantum yields in ethanol plotted according to Equation 2.2 assuming two different values of $\phi_{F,max}$ (see text).

Fluorescence lifetimes for Dy-630 show a similar dependence on solvent viscosity (Table 1 and Figure 2B.), although values of ϕ_F and τ_F in water are lower than what would be expected based solely on viscosity (Table 1, Figs 2A and 2B). Quenching of fluorescence by water has been previously reported in the literature for the symmetric cyanines (e.g. Cy5, Cy7)⁹⁶ and other fluorescent dyes,¹⁰⁰ and interpreted in terms of a

hydrogen-bond assisted nonradiative deactivation pathway of the fluorescent state. The quantum yields of the red-absorbing symmetric cyanines Cy5 and Alexa Fluor 647 are *c.a.* 20% greater in D₂O than in H₂O, and this is often cited as evidence of the hydrogen bond-mediated nature of the quenching mechanism.^{96,100} We observed a similar 1.2-fold increase in the lifetime of Dy-630 when H₂O was substituted by D₂O (Fig. 2.2B), but we note that the viscosity of D₂O at room temperature is 1.24-fold greater than the viscosity of H₂O, so the observed increase in fluorescence lifetime in D₂O does not necessarily provide support for the hydrogen-bond assisted deactivation pathway.

The fluorescence quantum yield of Dy-630 also depends strongly on temperature, as is the case of the symmetric cyanines,^{82,85,86,89,99} indicating that the main deactivation pathway is an activated process. Fluorescence quantum yields were determined in ethanol in the range 7-70°C as described in Materials and Methods, and shown in Fig. 2.2C. Results were analyzed following the formalism used previously for symmetric cyanines, including Cy3, diIC₂(3) and diIC₂(5).^{82,89,101} Assuming that the kinetic rate constant for photoisomerization (bond rotation from the first singlet excited state) can be expressed in terms of the Arrhenius equation, the dependence of ϕ_F with temperature can be expressed as:

$$\ln[\phi_F^{-1} - \phi_{F,max}^{-1}] = \ln A - E_a/RT \quad (2.2)$$

where ϕ_F is the temperature-dependent fluorescence quantum yield of Cy3, $\phi_{F,max}$ is the fluorescence efficiency that would be measured in the absence of photoisomerization, E_a represents the activation energy for bond rotation in the excited state, and A is a constant

that depends on the local microscopic friction and the radiative lifetime of fluorescence.^{82,89} Fig. 2.2D shows the $\phi_F(\text{ethanol})$ values measured for Dy-630 plotted according to equation 2.2 assuming $\phi_{F,max} = 0.85$ (as reported for Cy3)⁸⁹ or $\phi_{F,max} = 0.6$ (as reported for diIC₂(5)).⁸² The impact of $\phi_{F,max}$ on the slope is small, so precise knowledge of this quantity is not needed to obtain E_a . Agreement with equation 2.2 is excellent, as judged by the linearity of the plot, and the activation energy obtained from the slope is 21 kJ/mol (assuming $\phi_{F,max} = 0.85$). This value is similar to the one reported for diIC₂(3) in ethanol (19.7 kJ/mol)⁸⁵, and lower than the value reported for the red-absorbing symmetric cyanine diIC₂(5) (25 kJ/mol).⁸²

Together, these results are consistent with an isomerization deactivation mechanism similar to the one reported for the symmetric dyes. Further support for this model was obtained from transient spectroscopy experiments as discussed next.

B. Laser Flash Photolysis

In the ground state, the symmetric cyanines such as Cy3 and Cy5 exist in the all-*trans* form shown in Fig. 2.1.¹⁰⁵ Following light absorption, the singlet excited state can deactivate efficiently by rotation around a C-C bond of the polymethine chain to form a *cis* ground-state photoisomer that eventually returns to the thermodynamically stable all-*trans* ground state.^{79,86,99} The dynamics and spectral properties of the transient *cis* isomers of these cyanines have been investigated by laser flash-photolysis.^{89,99,106,107} The absorption

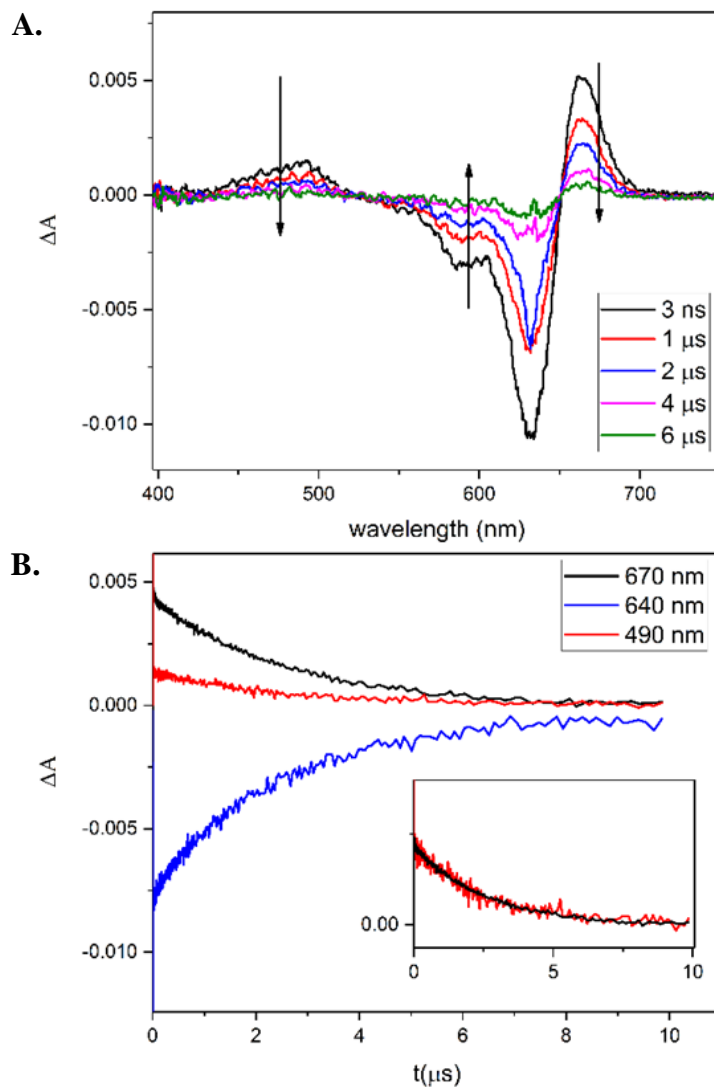


Figure 2.3: Transient Absorption Data for Dy-630. (A) Transient spectra of Dy-630 in ethanol measured at different times after excitation. The data at earlier times is dominated by stimulated emission of the *trans* excited state and is omitted for clarity. (B) Kinetic traces measured at 490 nm (red), 640 nm (blue) and 670 nm (black). All traces fit with a single decay constant of 2.5 μs . Inset: Traces measured at 490 nm (red) and 670 nm (black) normalized arbitrarily to emphasize their identical kinetic behavior.

spectrum of the *cis* isomer is *c.a.* 20 nm red-shifted with respect to the spectrum of the ground *trans* state, and its fluorescence quantum yield is negligible.^{106,108,109} The rate constants of the thermal back-isomerization reaction that eventually returns to the

thermodynamically stable all-*trans* ground state.^{79,86,99} The rate constants of the thermal back-isomerization reaction (k_{biso}) have been reported as $k_{\text{biso}} = 10^5 \text{ s}^{-1}$ for diIC₂(3) in propanol at room temperature,¹⁰⁶ and $k_{\text{biso}} = 10^3 \text{ s}^{-1}$ for diIC₂(5) in ethanol.⁸²

We investigated the potential formation of a transient Dy-630 photoisomer using transient absorption spectroscopy as we have done in the past to investigate photoisomerization of the green-absorbing cyanine Cy3.⁹² A solution of Dy-630 in ethanol was excited at 630 nm and probed with a white light source. Transient absorption spectroscopy measures the change in absorbance ($\Delta A(\lambda)$) after the sample is excited with a pulsed laser. Fig. 2.3A shows transient spectra measured in the 3 ns–10 μs range after excitation. The data at earlier times is dominated by stimulated emission from the *trans* excited state, and are not included in the figure for clarity. The negative ΔA signal observed around 640 nm coincides with the absorption spectrum of the *trans* ground state of Dy-630, and is consistent with the depletion of the ground state due to the generation of the singlet-excited state. The positive signals around 490 nm and 670 nm indicate the generation of transient states that decay back to the ground state in the microsecond-timescale. Individual kinetic traces at three wavelengths are shown in Fig. 2.3B. The decay constant for the three signals is 2.5 μs , and the fact that the transient measured at 490 nm decays with the same rate constant than the transient measured at 670 nm (Fig 2.3B, inset) indicates that the two bands belong to the same species. This transient has the same characteristics observed for the *cis* isomer of the symmetric cyanines, namely a *c.a.* 15 nm red-shift in absorption and a μs -timescale lifetime.^{82,89,106,110-112} Interestingly, the 2.5 μs lifetime measured for the isomer of Dy-630 is similar to lifetimes reported for green-absorbing symmetric trimethyne

dyes ($\sim 1\text{-}5\ \mu\text{s}$ depending on conditions),^{89,106,111,112} and shorter than the values reported for the red-absorbing symmetric pentamethyne dyes ($\sim 100\ \mu\text{s}$).^{82,110,111}

C. Interactions between Dy-630 and the DNA Nucleobases

In previous work we reported the increase of fluorescence quantum yield and lifetime of Cy3 and diIC₂(3) in solutions containing nucleoside monophosphates (dNMPs, N = A,G,T,C).¹⁰¹ Changes were more pronounced for the purines (dAMP, dGMP) than the pyrimidines (dTMP, dCMP), suggesting that Cy3–nucleoside $\pi\text{-}\pi$ interactions decrease the efficiency of photoisomerization of the cyanine, thereby increasing the efficiency of fluorescence. Here, similar experiments were performed with the red-absorbing dyes diIC₂(5) and Dy-630. Fluorescence quantum yields and lifetimes were measured in the presence of increasing concentrations of dNMPs. As previously observed with the trimethine cyanines,¹⁰¹ the fluorescence quantum yield of the red-absorbing dyes increases in solutions of dNMPs, and the increase is more pronounced with the purines (Fig. 2.4A). The maximum increase was observed for Dy-630 in 100 mM dAMP (3.7-fold). The corresponding values for the symmetric cyanines diIC₂(3) and diIC₂(5) are 1.9-fold¹⁰¹ and 1.2-fold (Fig. 2.4B), respectively. Lifetime measurements with Dy-630 in solutions of dAMP or dGMP show a trend similar to that observed in the steady-state measurements. Fig. 2.5A shows the time-resolved intensity decays measured in 50 mM and 100 mM solutions of dAMP and dGMP. As observed in the steady-state measurements, the average fluorescence lifetime increases with increasing dNMP concentration, and it is more pronounced for dAMP than for dGMP. At least three exponential terms are needed to fit

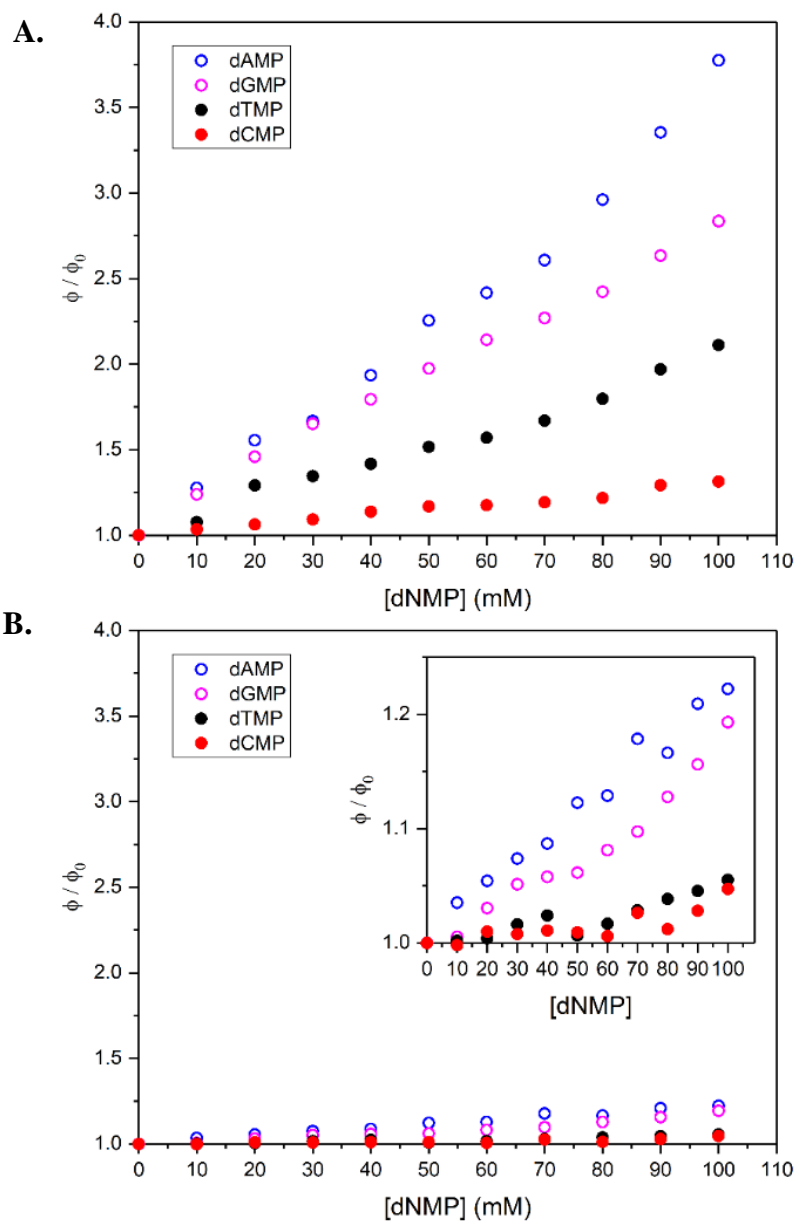


Figure 2.4: Steady-State Data of Dy630 with dNMP. Relative fluorescence quantum yields of Dy-630 (panel A) and DiIC₂(5) (panel B) plotted as a function of increasing concentrations of dNMP. dAMP (open blue circles), dGMP (open magenta circles), dTMP (filled black circles) and dCMP (filled red circles). Values are relative to the quantum yield of the dye in the absence of dNMPs (ϕ_0). The concentration of dye is 5 μM in all cases. Panels A and B have the same scale for a more direct comparison. The insert of panel B shows the same data in a narrower scale.

the decays in the presence of dNMPs. All decays acquired with varying concentrations of dAMP and dGMP can be fitted globally with the same three lifetimes: $\tau_1 = 0.19$ ns, $\tau_2 = 0.65$ ns, and $\tau_3 = 1.66$ ns.

The normalized amplitudes (a_i , Equation 2.1) vary depending on the nature of the nucleobase and its concentration (Fig. 2.5B for dAMP, and Fig. 2.13 for dGMP). These data show that Dy-630 associates with the dNMPs in a manner similar to that observed previously for the green-absorbing cyanines, but the effect on the fluorescence quantum yield and lifetime of the dye is greater for Dy-630 than for DiIC₂(3). The shortest lifetime can be interpreted as a population of free (non-interacting) molecules, while the other two can be interpreted in terms of populations of dyes interacting weakly (τ_2) and strongly (τ_3) with the nucleobases. We note that extracting association constants from these data is hindered by the fact that nucleotides self-associate in solution at the high concentrations used in the experiments.^{113,114} About 30% of the dAMP molecules are expected to be part of dimers or higher order assemblies at the highest dAMP concentration used in Fig. 4, so the measured quantum yields reflect interactions between the dye and a distribution of dAMP self-assembled species.¹¹⁵

Even though the increase of Fig. 2.4A is indicative of dye-dNMP interactions, the opposite is not necessarily true. The fact that the quantum yield of diIC₂(5) does not change significantly in the presence of dNMPs does not rule out dye-nucleobase interactions, but suggests that interactions do not result in a significant change in the lifetime of the excited state of the dye. Interactions between symmetric cyanines and dNMPs or DNA have been

previously established by measurements of changes in the diffusion coefficient of the dyes¹¹⁵ and by NMR.^{116,117}

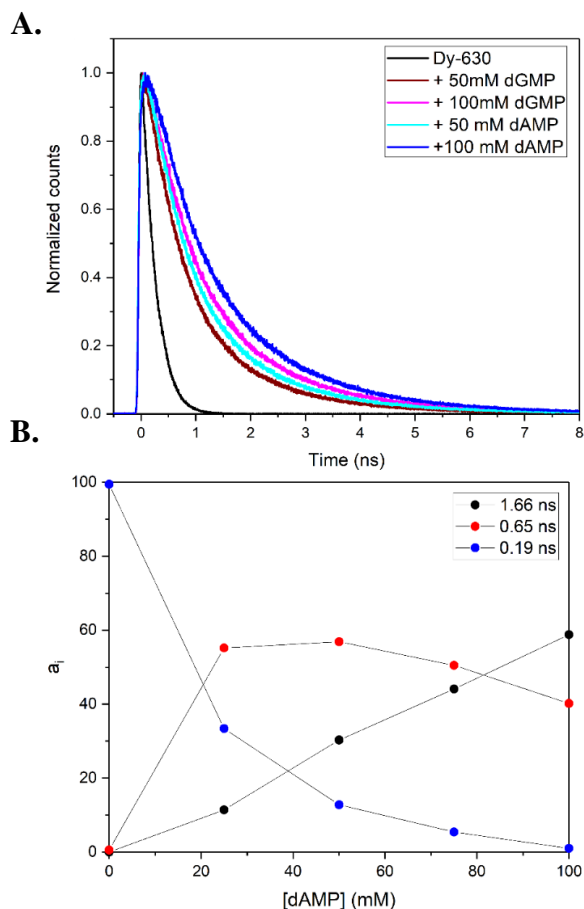


Figure 2.5: Lifetime Data of Dy630 with dNMP. (A) Normalized fluorescence intensity decay of Dy-630 in aqueous buffer (black) and in solutions of 50 mM or 150 mM dAMP or dGMP, as indicated in the figure legend. (B) Relative normalized amplitudes ($\sum_i a_i = 1$) for the three fluorescence lifetimes obtained from a global fit of the time resolved fluorescence decays measured at different dAMP concentrations. Data points in panel B are connected by lines just to guide the eye.

D. Fluorescence Properties of Dy-630 Bound to DNA

The fluorescence quantum yield and lifetime of Cy3 on DNA depend strongly on DNA sequence, DNA secondary structure, and the type of linker used to attach the dye to

the DNA base.⁸⁹⁻⁹¹ In this work, we characterized the fluorescence properties of Dy-630 bound to a DNA substrate similar to the one we used in our previous investigation of the photophysical mechanism of the PIFE phenomenon for Cy3 bound to DNA (Fig. 2.1F).⁹² A comprehensive study of the variables that affect the fluorescence properties of this dye on DNA (e.g. sequence and secondary structure) is beyond the scope of this work, and will be the subject of future research. The quantum yield and lifetime of Dy-630 increase significantly when the dye is bound to DNA and two exponential terms are required to fit the intensity decay of the Dy-630-DNA sample (Table 2). A similar trend was observed for Cy5 bound to the same DNA sample, but changes with respect to the dye free in solution were not as marked as in the case of Dy-630.

Addition of the protein Klenow fragment (KF) to Dy-630-DNA, which binds at the DNA primer-template junction where the dye is located, results in a modest increase in average lifetime (1.08-fold, Table 2.3). Binding of the protein was verified by time-resolved fluorescence anisotropy (Fig. 2.14), and the enzyme was shown to be biochemically active on the Dy-630-DNA construct (Fig. 2.15). Therefore, the modest enhancement observed upon protein addition is not due to impaired protein binding and is an indication that the fluorescence properties of the dye are not greatly changed by its proximity to the protein. This result is discouraging in the context of using Dy-630 as a PIFE probe. In comparison, the fluorescence intensity decay of Cy3 bound to the same DNA template requires three lifetimes (Table 2.2), the shortest of which is very close to the lifetime of the free dye in aqueous buffer (180 ps)⁸⁹. The fractional amplitude of the short lifetime of Cy3 decreases significantly when KF binds to the DNA substrate, resulting

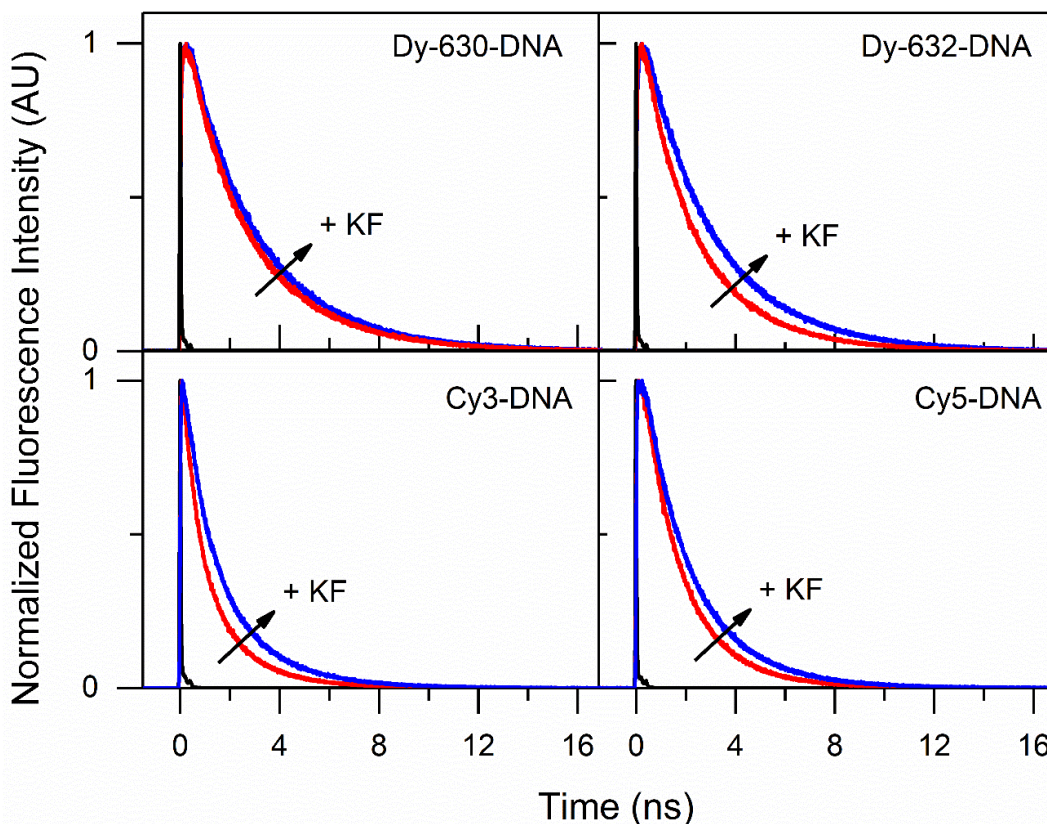


Figure 2.6: Lifetime Data of Dy-630-DNA with KF. Normalized fluorescence intensity decays of the four dyes bound to DNA before (red) and after (blue) addition of 1.25 equivalents of KF. Instrumental response functions are shown in black.

in a 1.45-fold increase in the average lifetime that leads to the increase in brightness commonly described as PIFE (Table 2.3). These results suggest that Cy3 is a good probe for PIFE applications because a significant fraction of the dye molecules retain a short lifetime when bound to DNA. This short lifetime is consistent with efficient photoisomerization and indicate weak dye-DNA interactions. In contrast, in the case of Dy-630-DNA, dye-DNA interactions appear to be stronger, resulting in the loss of the fraction of dyes with short lifetime that are responsible for the PIFE phenomenon in Cy3.

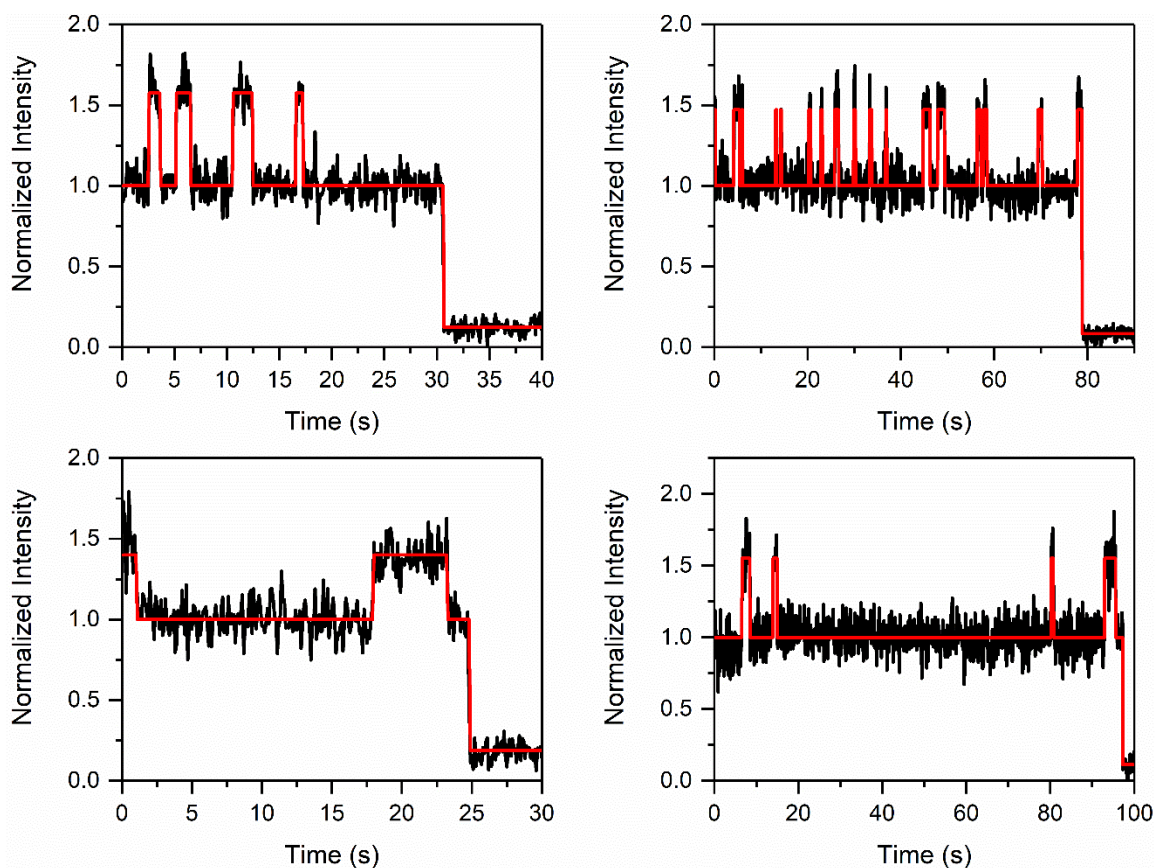


Figure 2.7: Single-Molecule Traces of Dy-630-DNA. Representative single-molecule fluorescence traces of Dy-630-DNA (black) and idealized traces obtained using the vbFRET package (red).

Based on this, we hypothesized that increasing the negative charge on the Dy-630 dye could be a strategy to decrease dye-DNA interactions and regain the population of dyes with the short lifetime necessary for the substantial protein-induced enhancement observed with Cy3. The dye commercialized as Dy-632 shares the same chromophore with Dy-630 but has two additional negative charges (Fig. 2.1). The fluorescence intensity decay of Dy-632-DNA also shows two lifetimes significantly longer than the lifetime of the dye in fluid solution (Table 2), but the two lifetimes are somewhat shorter than the lifetimes measured with Dy-630, and the normalized amplitude of the shorter lifetime (a_2 , Table 2.2) is higher

for Dy-632 than for Dy-630. These results suggest that although Dy-632 still experiences an environment that leads to a reduced efficiency of isomerization, the additional charges alleviate the impact of the interactions with the DNA bases to some extent. Consistent with this, addition of KF to Dy-632-DNA results in a 1.27-fold increase in the average lifetime (Fig. 2.6 and Table 2.3). Although this value is greater than the increase observed with Dy-630, it is lower than the value measured with the symmetric cyanine Cy5 (1.33-fold increase, Fig. 2.6 and Table 2.3) and significantly lower than the value measured for Cy3, the archetypical PIFE dye. Single-molecule fluorescence experiments were carried out next to gain more insights into the photophysical behavior of Dy-630 and Dy-632 bound to DNA, and to assess their potential as single-molecule probes. Experiments were performed using a prism-type total internal reflection single-molecule instrument (TIRF) as described in Materials and Methods. Singly tethered Dy-630-DNA molecules were excited continuously and images were averaged and saved every 100 ms. Representative time traces from individual molecules are shown in Figs. 7 and 8. Individual traces were normalized so that all average intensities in the low-fluorescence state are the same and equal to an arbitrary intensity of one. Both dyes are photostable under this experimental conditions, and can be imaged for tens of seconds before photobleaching using the same buffers commonly used for imaging Cy3 and Cy5 (see Materials and Methods). Visual inspection indicates the presence of at least two states with distinct average fluorescence quantum yield that interconvert in the second-timescale. Only one state was observed in experiments using the same DNA but labeled with Cy5 (Fig. 2.16). All traces were analyzed using the vbFRET package implemented in MATLAB⁹⁸ to generate and fit

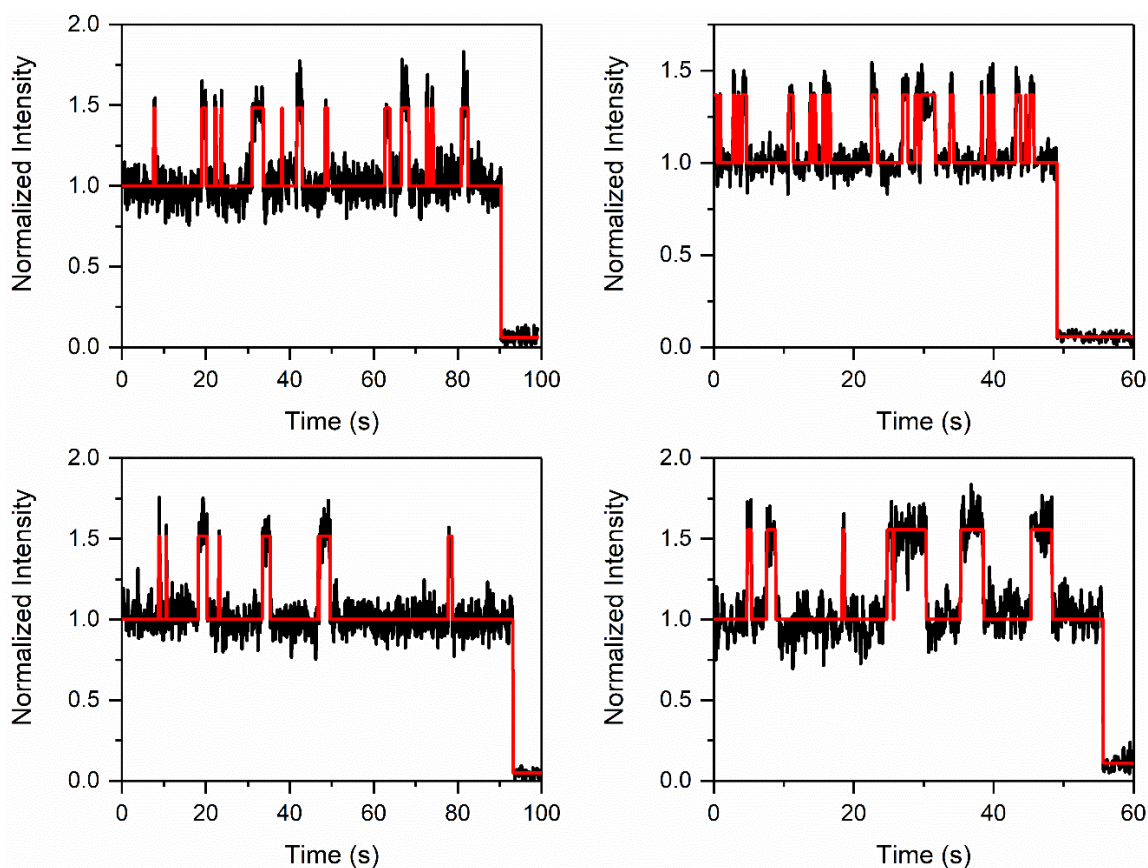


Figure 2.8: Single-Molecule Traces of Dy-632-DNA. Representative single-molecule fluorescence traces of Dy-632-DNA (black) and idealized traces obtained using the vbFRET package (red).

idealized molecular traces (shown in red in Figs. 2.7 and 2.8). Dwell times for the high-fluorescence state (H) and the low-fluorescence state (L) were obtained from the idealized traces of *c.a.* 50 individual molecules. Histograms are shown in Fig 2.9.

The kinetic rate constants for the conversion between H and L and between L and H were calculated as described in the supplemental materials as $k_{HL} = 0.91 \text{ s}^{-1}$ and $k_{LH} = 0.18 \text{ s}^{-1}$ (Dy-630), and $k_{HL} = 1.14 \text{ s}^{-1}$ and $k_{LH} = 0.27 \text{ s}^{-1}$ (Dy-632). Both dyes spend more time in the low-fluorescence state, and sulfonation of the Dy-fluorophore (i.e. Dy-632 vs

Dy-630) results in a reduction of the time the dye spends in both the H and L states. These results suggest that both states represent fluorophores that interact with the DNA, although to a different extent. Comparison of the single-molecule data with the ensemble lifetime data is not straightforward. The lifetime data of both Dy-630 and Dy-632 shows a larger population of dyes with a long lifetime (greater a_1 in Table 2.2), while the single-molecule data indicates that the dyes spend most of the time in a state with a lower fluorescence intensity. Although we cannot fully interpret the differences observed in both types of experiments, we note that the single-molecule intensities are measured under continuous laser illumination, and are therefore proportional to the photostationary concentration of *trans* isomers in the excited state. This concentration is not only proportional to the lifetime of the emitting species, but depends also on the fraction of dark (*cis*) isomers that are generated under continuous illumination. The rate of the thermal *cis-trans* reaction ($\sim 1/2.5 \mu\text{s}$) in fluid solution, Fig. 2.3) is much slower than the rates of the photophysical steps, so the fraction of *cis* isomers that accumulates in photostationary conditions can be quite high.¹¹⁸ Furthermore, this fraction may be higher for molecules with a higher fluorescence lifetime due to lower rates of isomerization in both directions. Therefore, the relative intensities measured in single-molecule conditions may be quite different from the relative lifetimes of the corresponding populations.

2.5 Discussion

We characterized the photophysical properties of the hemicyanine Dy-630 in the context of its potential applications as a single-molecule fluorescent probe for PIFE

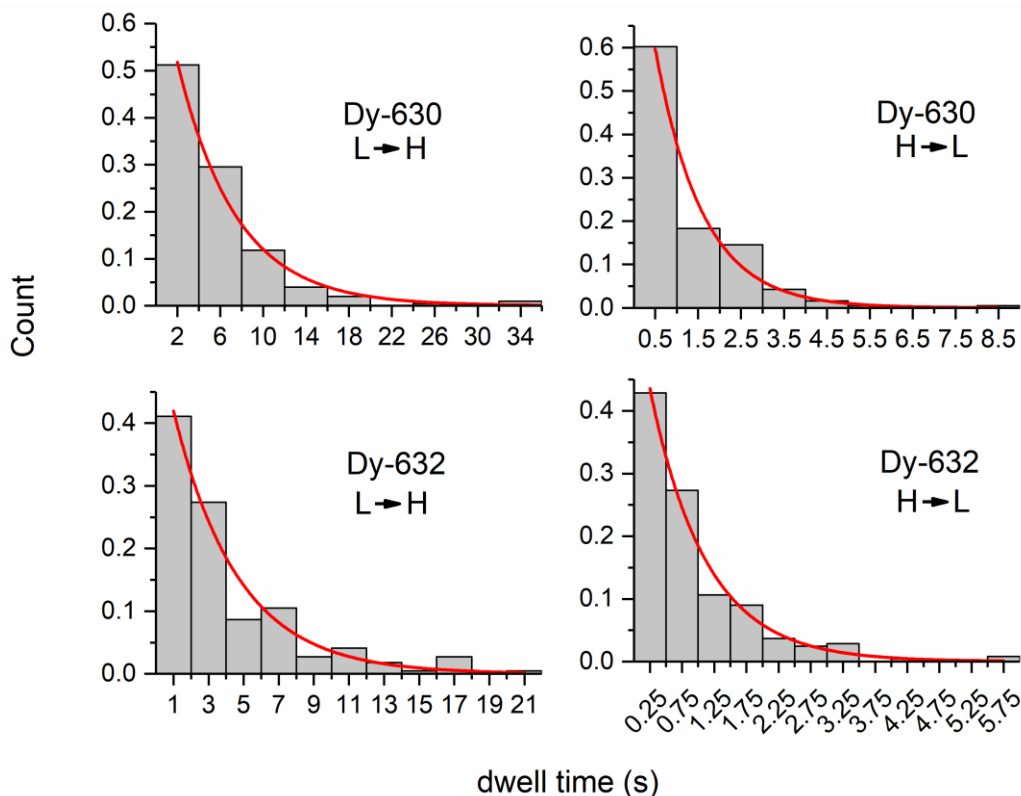


Figure 2.9: Dwell Time Analysis of Dy-630-DNA and Dy-632-DNA. Histograms of dwell times obtained from the single-molecule traces of Dy-630-DNA (top) and Dy-632-DNA (bottom). L→H refers to the dwell times in the low-intensity state, and H→L refers to the dwell times in the high-intensity state. Red lines are fits according to the model described in the Supplemental Materials.

applications. To date, Cy3 remains the most popular single-molecule dye for PIFE because in addition to its excellent single-molecule properties (i.e. brightness and photostability), its fluorescence quantum yield is highly sensitive to interactions with DNA and proteins. We have shown that Cy3 performs well in this type of single-molecule application because binding to DNA does not completely eliminate photoisomerization.^{89,91,92,115} The time-resolved decays of Cy3 bound to DNA show a fraction of the amplitude with a short lifetime that is similar to that of the dye free in solution, consistent with a fraction of dyes that do not interact strongly with the DNA and are therefore able to isomerize in the excited

state. The interaction of a Cy3-DNA sample with a protein results in a steric restriction of increases the lifetime of the excited state and therefore the quantum yield and brightness of the dye (PIFE).⁹²

We investigated the red-absorbing cyanine Dy-630 as a potential PIFE dye for red laser excitation. Dy-630 and Cy3 share a 3-carbon polymethine chain in their structures, but the absorption and fluorescence spectra of the first are closer to that of the pentamethine. The behavior of Dy-630 in solution is indeed similar to that observed with the trimethine dyes Cy3 and diIC₂(3). The fluorescence quantum yield and lifetime of Dy-630 increase with increasing viscosity, and decrease with increasing temperature in a way the photoisomerization process, which is consistent with the existence of an activated nonradiative process that depopulates the singlet state of the dye (Fig. 2). dye Cy5. In simple terms, we hypothesized that Dy-630 would be a probe with the spectral properties of Cy5 and the desirable photophysical properties of Cy3.

The results of the transient spectroscopy experiments show the formation of a transient species with an absorption spectrum shifted *c.a.* 30 nm to the red that decays back to the ground state within a few microseconds in fluid solution (Fig. 2.3). These results are consistent with the formation of a photoisomer with properties similar to those of the symmetric tricarbocyanines Cy3 and DiIC₂(3), and suggest that Dy-630 could be a promising candidate for PIFE in the red region of the spectrum. Further experiments with DNA samples, however, paint a more complex scenario. As in the case of Cy3, the quantum yield of Dy-630 increases significantly when the dye interacts with the DNA nucleoside monophosphates (dNMPs) in solution (Fig. 4), and in fact the enhancement is significantly

Table 2.1: Spectroscopic and Photophysical Properties of Dy-630, diIC₂(5), and diIC₂(3) in Pure Solvents.

	Dy-630	diIC ₂ (5)	diIC ₂ (3)
λ^{maxabs} (ethanol)	636 nm ^(a)	639 nm ^(b)	546 nm ^(b)
ϵ_{max} (cm ⁻¹ M ⁻¹)	2.00×10^5 ^(c)	2.00×10^5 ^(b)	1.33×10^5 ^(b)
λ^{maxem} (ethanol)	660 nm ^(a)	664 nm ^(b)	563 nm ^(b)
ϕ_F (ethanol)	0.082 ^(a,§)	0.18 ^(a,*) , 0.21 ^(d)	0.042 ^(e)
τ_F (ethanol)	0.37 ^(a)	0.81 ^(a)	0.162 ^(f)
E_a (kJ/mol)	21 ^(a)	25 ^(g)	19.7 ^(f)
ϕ_F (water)	0.014 ^(a,§)	0.09 ^(a,*)	0.023 ^(a,**)
τ_F (water)	0.19 ^(a)	0.41 ^(a)	0.08 ^(h)
ϕ_F (glycerol)	0.51 ^(a)	0.24 ⁽ⁱ⁾	0.35 ^(a)
τ_F (glycerol)	2.3 ^(a)	1.8 ⁽ⁱ⁾	1.5 ^(a)

λ_{max}^{abs} : Absorption maximum; ϵ_{max} : extinction coefficient at λ_{max}^{abs} ; λ_{max}^{em} : fluorescence maximum; ϕ_F : fluorescence quantum yield; τ_F : fluorescence lifetime; E_a : activation energy for photoisomerization (Equation 2.2). (a) This work, (b) In ethanol from reference 73, (c) Reference 74, (d) Reference 41, (e) diIC₂(3) BF₄ from reference 61, (f) Reference 39, (g) Reference 36, (h) Reference 55, (i) Reference 75

§ relative to oxazine 1 in ethanol ($\phi_F = 0.15$)¹²², * relative to diIC₂(5) in methanol ($\phi_F = 0.15$)¹²¹, ** relative to diIC₂(3) in ethanol ($\phi_F = 0.042$)¹⁰⁷

more pronounced in the case of Dy-630. Although this appeared to be promising at first, time resolved-experiments using dAMP (Fig. 2.5) show that the short lifetime (consistent with a population that can isomerize efficiently) has a negligible fractional contribution at about 100 mM dAMP. Consistent with this observation, the short lifetime is also absent in the Dy-630-DNA sample where the dye is covalently attached to the DNA (Table 2). In contrast, in the case of Cy3, about 37% of the dye molecules decay with a short lifetime similar to that measured for the dye in fluid solution. We have shown that this is the fraction that gives a window for the fluorescence enhancement observed when a protein binds in the proximity of the dye. Indeed, addition of Klenow fragment to the Cy3-labeled template-primer DNA sample used in this work results in a significant reduction of the fractional contribution of the short lifetime and a concomitant increase in the average fluorescence lifetime of the dye (Table S1). Instead, in the case of Dy-630, protein binding has only a small effect in the fluorescence lifetime of the dye.

These results indicate that Dy-630 is not a useful probe for PIFE because, in contrast to Cy3, its fluorescence lifetime on DNA is already too high due to loss of a significant population of dyes exhibiting a lifetime similar to that of the free dye. Increasing the negative charge on the dye by means of sulfonation (Dy-632) results in an increased sensitivity of the dye to protein binding, but the enhancement is too low for practical single-molecule applications. In addition, although these probes display good photostability and brightness under single-molecule conditions, the two distinct intensity levels observed in the experiments with the DNA samples in the absence of protein (Figs. 7 and 8) suggest that the dye interacts with the DNA strands in two different modes that inhibit

isomerization to varying extents. These fluctuations in fluorescence intensity greatly limit the usability of Dy-630 in single molecule applications. Yet, Dy-630 interactions with the DNA bases are sequence-dependent, and may also be different for different modes of attachment and dye position within the DNA construct. Therefore, we do not dismiss the possibility that this dye may be useful in other situations, perhaps when attached to the end of the DNA strand and far away from the junction between the double helix and the single-stranded template.

Table 2.2: Fluorescence Quantum Yields and Lifetimes of Cy5, Dy-630, and Dy-632 Covalently Bound to DNA. All measurements were performed in 10 mM TRIS buffer (pH = 7.4) at room temperature.

	ϕ_F	τ_1 (ns)	a_1	τ_2 (ns)	a_2	τ_3 (ns)	a_3	$\langle\tau\rangle^*$ (ns)
Cy3-DNA	0.23 ^(**)	2.1	0.22	1.0	0.41	0.2	0.37	0.95
Cy5-DNA	0.39 ^(§)	2.0	0.58	1.0	0.42	-	-	1.6
Dy-630-DNA	0.50 ^(§)	3.0	0.73	1.3	0.27	-	-	2.5
Dy-632-DNA	0.44 ^(§)	2.6	0.68	1.1	0.32	-	-	2.1

$$* \langle\tau\rangle = \sum_i a_i \tau_i$$

** relative to diIC₂(3) in methanol (Table 1)

§ relative to oxazine 1 in ethanol ($\phi_F = 0.15$)¹²²

2.6 Conclusions

The results presented in this work complement previous work from our laboratory characterizing the photophysics of trimethine carbocyanines on DNA and the phenomenon

of protein-induced fluorescence enhancement. The photophysical properties of the red-absorbing dye Dy-630 in solution resemble those of Cy3, the archetypical PIFE dye for single-molecule applications with green-excitation. However, the behavior of Dy-630 on the primer-template DNA sample used in this work is complex and indicates that the dye interacts with the DNA bases in at least two distinct modes that affect the fluorescence quantum yield of the dye to different extents. This results in fluorescence fluctuations in the second timescale that precludes the use of this dye as a PIFE probe. Together, the results of this and previous work shed light on the optimal probe design principles for PIFE applications. The ideal PIFE probe has a fluorescence quantum yield that changes significantly when the dye is in a sterically-restricted environment. Furthermore, the dye should have an intermediate fluorescence quantum yield when bound to the DNA that is high enough to be measured at the single-molecule level before protein binding, but low enough to allow for a significant range of increase. The moderate fluorescence quantum yield of Cy3 on DNA is the result of a complex fluorescence lifetime decay that includes a fraction of bright dyes (long lifetime, restricted isomerization) and a significant fraction of less fluorescent dyes (short lifetime, efficient isomerization). The latter provides the opportunity for a further increase when the dye is located in a sterically-restricted environment. In the case of Dy-630, our results show that the quantum yield of the dye on the particular DNA construct used in this work is already too high to allow for a substantial further increase upon protein binding. This, together with the fluorescence fluctuations observed at the single molecule level, rule out Dy-630 as a useful probe for PIFE applications in the red region of the spectrum.

2.7 Acknowledgments

We acknowledge use of the UltraFast Laser facility at Arizona State University. We thank Gabe Salmon and George Brockett for their help during the initial stages of the project.

CHAPTER THREE

JOURNAL OF THE AMERICAN CHEMICAL SOCIETY

“CYANINE CONFORMATIONAL RESTRAINT IN THE FAR-RED RANGE”

3.1 Abstract

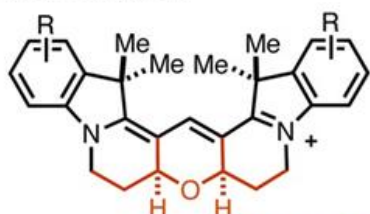
Far-red cyanine fluorophores find extensive use in modern microscopy despite modest quantum yields. To improve the photon output of these molecules, we report a synthetic strategy that blocks the major deactivation pathway: excited-state trans-to-cis polyene rotation. In the key transformation, a protected dialdehyde precursor undergoes a cascade reaction to install the requisite tetracyclic ring system. The resulting molecules exhibit the characteristic features of conformational restraint, including improved fluorescence quantum yield and extended lifetime. Moreover, these compounds recover from hydride reduction with dramatically improved efficiency. These observations enable

efficient single-molecule localization microscopy in oxygenated buffer without addition of thiols. Enabled by modern organic synthesis, these studies provide a new class of far-red dyes with promising spectroscopic and chemical properties.

3.2 Main Text

Single molecule localization microscopy (SMLM) techniques like photoactivated localization microscopy (PALM) and direct stochastic optical reconstruction microscopy (Dstorm) enable three-dimensional (3D) imaging of cellular components with nearly molecular resolution.^{123–125} Localization precision, and therefore the structural resolution capability of SMLM, scales with the inverse square root of the single molecule emitter

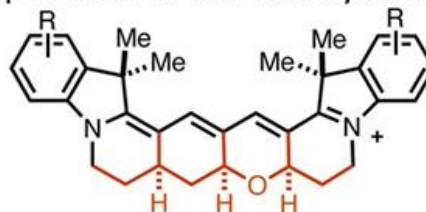
A. Prior Studies



Trimethine
Cyanine
(black)
e.g. Cy3
 $\Phi_F(\text{H}_2\text{O}) = 0.09$

Restrained
Variant
(black + red)
e.g. Cy3B
 $\Phi_F(\text{H}_2\text{O}) = 0.85$

B. Application to Far-Red Cyanines



Pentamethine
Cyanine
(black)
e.g. Cy5, AF647

Restrained
Variant
(black + red)
These studies

C. Retrosynthetic Analysis

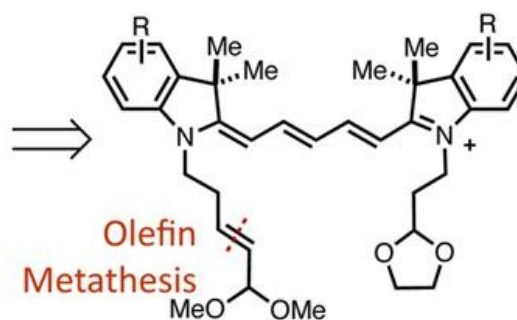
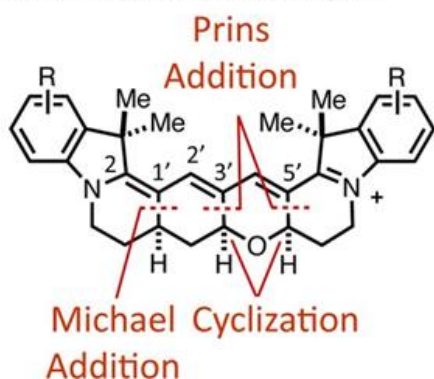


Figure 3.1: Structural Information of Fluorophores. (A) Conformational restraint applied to trimethine cyanines, (B) application to far-red cyanines (these studies), and (C) retrosynthesis.

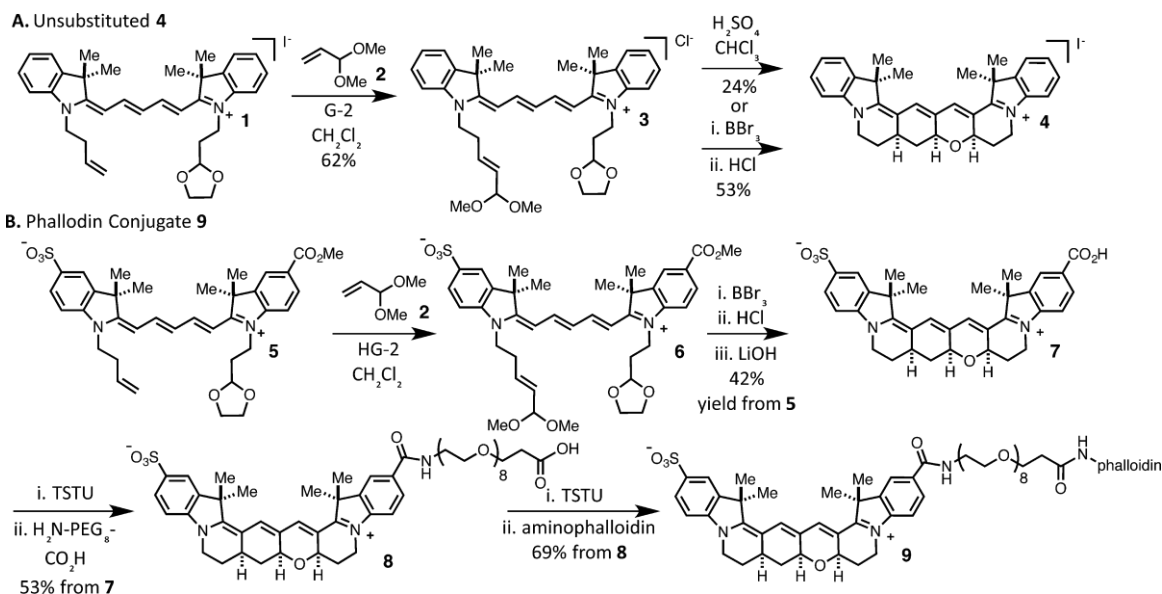
intensity.¹²⁶ Consequently, SMLM fluorophores should provide high photon yields in the on state, while exhibiting low to absent background fluorescence in the off state. Small molecules, in combination with various targeting strategies, are often uniquely well-suited to these applications.¹²⁷ Indocyanines are among the most useful fluorescent small molecules, uniquely spanning the visible to near-infrared range through successive 2-carbon homologation.¹²⁸⁻¹³⁰ Far-red variants, including Cy5 and Alexa 647 (AF647), are the most common chemical component of Dstorm methods.¹³¹⁻¹³³ However, fluorescence quantum yields (ϕ_F) are modest, typically below 0.2 in aqueous solution.¹³⁴ Cyanine excited state deactivation involves trans- to cis-polyene rotation that competes extensively with photon emission.^{134,135} In the trimethine series, which emits in the green region of the spectrum, this pathway has been obstructed through installation of fused 6-membered rings to the polymethine bridge, leading to dramatically improved ϕ_F (Figure 1A).¹³⁶⁻¹³⁸ Extending this approach to the far-red cyanines could provide needed brighter fluorophores in this spectral range, but requires the synthesis of a complex fused tetracyclic ring system (Figure 1B). Here we describe the first synthetic strategy to assemble conformationally restrained pentamethine indocyanines. The key reaction is a cyclization cascade of a protected dialdehyde precursor, which is accessed through chemoselective olefin metathesis (Figure 1C). The resulting far-red fluorophores exhibit improved fluorescence quantum yields and extended lifetimes relative to unrestrained pentamethine cyanines. In addition, we find these constrained cyanines recover from hydride reduction with superior efficiency relative to existing far-red cyanines. These observations enable SMLM,

providing resolution and photon output in oxygenated phosphate- buffered saline (PBS) exceeding that obtained with conventional cyanines in the optimized photoswitching buffers used in dSTORM.^{131,139}

The retrosynthetic analysis is shown in Figure 1C. In the key reaction, a protected dialdehyde undergoes intramolecular Michael addition followed by a dihydropyran ring-forming cascade. The latter sequence, but not the Michael addition, is analogous to that employed in the assembly of the Cy3B scaffold.¹³⁶ As the cyanine polyene is incompatible with nucleophilic olefination methods, a critical challenge is the chemoselective introduction of the sensitive α,β -unsaturated aldehyde motif (or synthetic equivalent). A cross-metathesis reaction was ultimately found to provide a suitable means to install an unsaturated acetal.¹⁴⁰

We first targeted the unsubstituted restrained indocyanine 4 (Scheme 1A). Precursor 1 was assembled through the conventional route from N-alkylated indolenines (see SI). Cross-metathesis using the Grubbs second-generation catalyst (30 mol %),¹⁸ and acrolein dimethyl acetal (2, 10 equiv) in CH_2Cl_2 at 40 °C provided 3 in 62% yield following SiO_2 purification. Compound 3 underwent tetracyclization in a 4:1 mixture of CHCl_3 :7 N H_2SO_4 at 70 °C to provide 4 as a single diastereomer in 24% yield. This structure, including the syn-syn ring junction stereochemistry, was assigned by NMR analysis. In examining alternative cyclization conditions, we found that exposing 3 to BBr_3 in CH_2Cl_2 at -78 °C provided 4 and a second compound, which was obtained in a variable ratio (~1:1 to ~2:1). The inseparable mixture

Scheme 3.1: Synthetic Route to 4 (A) and 9 (B)



exhibits a single $[M]^+$ ion signal, complex NMR signals in the dihydropyran region, and a single far-red UV–vis absorbance maximum. Compound 4 and the second compound, tentatively assigned to be a diastereomer, can be equilibrated to homogeneous 4 in 1:3 MeOH:0.3 M HCl at 60 °C with an improved two-step yield from 3 of 53% (Figure 1A). Computational analysis indicates the lowest energy diastereomer containing an anti-ring junction is diastereomeric to 4 adjacent to C5' of the polyene. Of note, simply subjecting 3 to the MeOH:HCl equilibration conditions provided only trace quantities of 4.

To gain access to a conjugatable variant, we adopted a related strategy starting from cyanine 5 (see SI for synthesis). Cross- metathesis using Hoyveda-Grubbs second-generation catalyst (50 mol %)¹⁴¹ proceeds efficiently between 5 and 2 at rt to provide 6, which was used without extensive purification (Scheme 1B). Though the tetracyclization cascade of 6 was incompatible with the biphasic aqueous acidic conditions, the use of BBr_3

in CH₂Cl₂ at -78 °C provided a similar mixture to that obtained with 4. Equilibration in 1:3 MeOH:0.3 M HCl at 60 °C gave the methyl ester which, after saponification and reverse phase purification, provided 7 in a useful four-step yield of 42%. To prepare bioconjugates, 7 was converted to the carboxylic acid 8 through a straightforward amide coupling sequence. Phalloidin conjugate 9 was then obtained by NHS-ester generation and amide bond formation. To our delight, compounds 4 and 7 exhibit the characteristic features of conformational restriction. The ϕ_F is increased from 0.15 (MeOH) with 10 (Figure 2A) to 0.69 (MeOH) and 0.55 (PBS) with 4 and 7, respectively (Figure 2B). This occurs with a shift in λ_{\max} of approximately 25 nm in both cases (Figure 2B,C). Both fluorescence lifetime and ϕ_F are largely solvent viscosity insensitive, unlike with the conventional pentamethine cyanine 10 that is subject to photoisomerization. Moreover, also unlike with 10, the emission of 4 is insensitive to temperature (Figure 2D). This is also due to photoisomerization in 10, which becomes more efficient at higher temperatures. The substantially longer lifetimes of 4 and 7 relative to the unrestrained cyanine 10 point to significant potential for fluorescence lifetime imaging microscopy (FLIM).¹⁴²

Motivated by these auspicious properties, we then investigated if these fluorophores could be applied in SMLM experiments. A central feature of SMLM is the photoactivation or conversion of fluorophores between fluorescent and non-fluorescent states.¹⁴³ Three modes of cyanine reactivity have been applied in this context: reversible formation of (1) thiol- and (2) phosphine-polyene adducts, as well as (3) sequential reduction/oxidation of the imine-like C2-N double bond.¹⁴⁴⁻¹⁴⁷ Noting that the reactivity of existing cyanines in these chemistries varies widely,^{133,147} we examined the new molecules. In an unanticipated

consequence of conformational restraint, the UV-light induced regeneration of **4** following NaBH_4 reduction is dramatically enhanced relative to unrestrained cyanines. Treatment of **4** and **10** with 2.0 equiv of NaBH_4 afforded the corresponding reduced product.¹⁴⁸ Strikingly, photolysis of a 20 μM solution in 4:1 PBS:DMSO with UV light (365 nm, 5 mW/cm^2) provides 38% maximal cyanine absorbance recovery with **4** after 5 min, but only a 6% maximal recovery after 30 min with **10** (Figure 2E). Of note, the degree of recovery in these ensemble studies is lower than seen in the microscopy studies below, which were carried out at much lower concentration. In examining other types of cyanine photoconversion, we found the phosphine adducts observed with conventional pentamethine cyanines, such as AF647, are not observed with **7**. Suggesting that the thiol

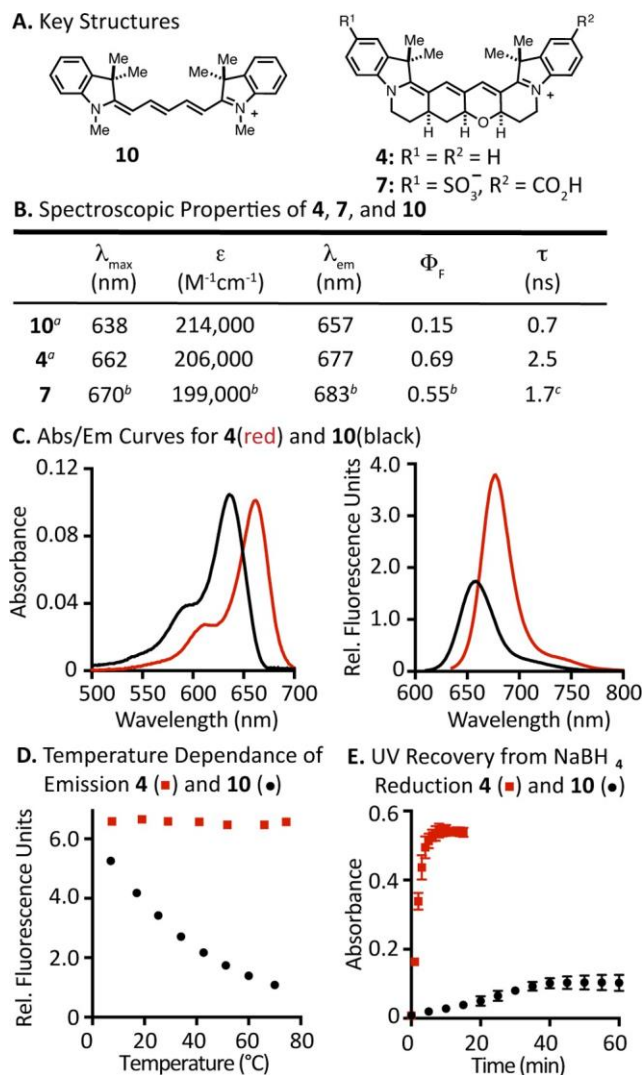


Figure 3.2: Photophysical Properties of Parent and Restrained Fluorophore. (A) Key structures and (B) their spectroscopic properties. (C) Absorbance/emission curves for 4 and 10 (750 nM in MeOH). (D) Temperature Dependence of the Emission of 4 (red ■) and 10 (black ●) (in EtOH) (E) UV recovery of 20 μ M 4 (red ■) and 10 (black ●) (in 4:1 PBS (50 mM, pH 7.4):DMSO) following NaBH₄ reduction (2.5 mM in 1:1 DMSO:MeOH). Absorbance at λ_{max} (4 at 640 nm and 10 at 660 nm) as a function of 365 nm irradiation time (5 mW/cm²). ^aIn MeOH. ^bIn pH 7.4 PBS. ^cIn H₂O.

adducts are also disfavored by ring constraint, SMLM with 9 under typical STORM conditions (high thiol, deoxygenated buffer) did not afford a useful reconstruction. Phalloidin conjugate 9 was applied to visualize cellular F- actin in initial wide-field studies. These efforts included comparisons to the commercially available Alexa Fluor 647-phalloidin conjugate (AF647-phalloidin), which has been used extensively. We observed that reduction and UV-activation of 9 provides dramatically improved recovery relative to AF647-phalloidin. We also found that photostability of 9 was nearly indistinguishable from that of AF647-phalloidin.

We then applied the phalloidin conjugate 9 to 3D PALM-like super-resolution imaging. We utilized a biplane imaging scheme (BP)²⁷ in combination with TRABI²⁸ to simultaneously precisely quantify single molecule intensities and perform TRABI-BP imaging. Labeling and reduction (26 mM NaBH₄) with subsequent imaging in non-degassed PBS provided high quality 3D super-resolved images of the actin cytoskeleton (Figure 3.3). In TRABI-BP experiments, we detected on average 5181 photons per frame

(median) from single activated dyes, whereas tracking emitters that are active in consecutive frames yielded a conflated photon count of 6961 (median) before photobleaching or conversion to a non-fluorescent form. This corresponds to experimentally measured localization precisions of 5–7 nm laterally and ~20 nm axially. Excitation with either 640 or 660 nm light can be employed, with the latter providing somewhat improved photon yield. We also found that while the UV-laser can accelerate the recovery, the photoactivation rate obtained using solely the excitation laser (either 640 or 660 nm) was sufficient to generate an emitter density suitable for SMLM. Interestingly, in SMLM experiments, recovery of the reduced state proceeds almost quantitatively if 405 nm light is applied only for very short time periods. By contrast, when AF647-phalloidin

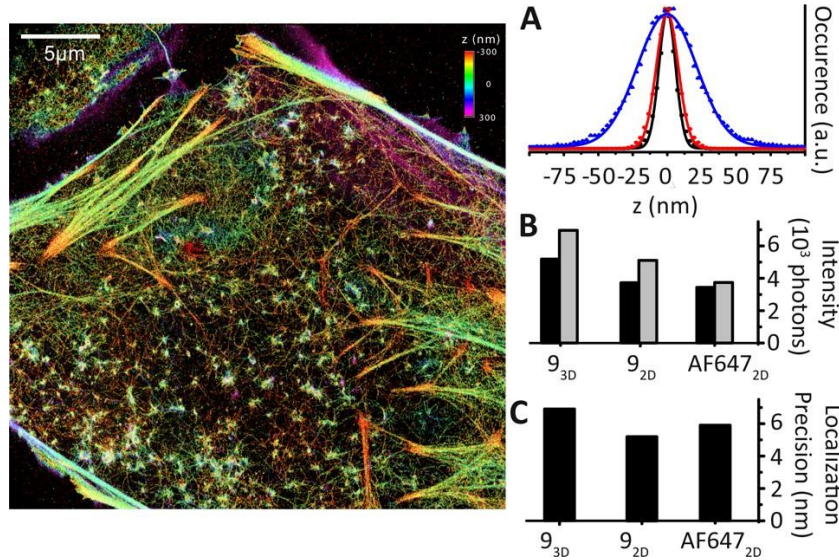


Figure 3.3: Super-Resolution Imaging Data. Left: High quality 3D TRABI-BP SMLM image of F-Actin in a U2OS cell with 9-phalloidin in PBS buffer. Right: (A) Lateral (x: black, y: red) and axial (blue) localization precisions calculated from the data illustrated on left. Marks indicate data points and solid lines indicate Gaussian fits to the data. (B) Comparison of single molecule photon intensities regarding single frame (black) and tracked (gray) median values of data illustrated in 93D (left) and comparable measurements (right). (C) Comparison of single molecule localization precisions regarding single frame (black) and tracked (gray) median values of data illustrated in 93D (left) and comparable measurements (right).

in 2D imaging modes of 9 (center) and AF647 (right) in standard dSTORM photoswitching buffer. (C) Experimentally determined lateral localization precisions of 93D (6.9 nm), 92D (5.2 nm), and AF6472D (5.9 nm).

was subjected to the reduction/recovery sequence, no reconstruction could be obtained. We have compared the images obtained with 9 using the reductive method with AF647 under standard dSTORM buffer conditions. Conjugate 9 gave similar, if slightly improved, photon counts relative to AF647-phalloidin (9: 3721 per frame, 5107 tracked; AF647:3422 per frame, 3737 tracked) and localization precisions of 5.2 and 5.9 nm, respectively (Figure 3.3).

In summary, we have developed a cascade cyclization strategy that appends a tetracyclic system to the pentamethine cyanine polymethine bridge. Conformational restraint improves. In summary, we have developed a cascade cyclization strategy that appends a tetracyclic ring system to the pentamethine cyanine polymethine bridge. Conformational restraint improves fluorescence quantum yield and prolongs lifetime, while also enhancing recovery from hydride addition. These properties enable PALM-like SMLM, providing excellent photon counts without recourse to high thiol, deoxygenated buffer. The combination of these new cyanines and reductive caging may be useful in other contexts, including live-cell localization and tracking experiments. Additionally, the improved recovery of the new variants may be enabling for sensing reactive oxygen species (ROS), another context where cyanine reduction/oxidation has been used.¹⁴⁸

These studies provide the chemical framework to create fluorophores targeting a range of applications. For example, the installation of additional sulfonates or other polar functional groups is likely a prerequisite for antibody labeling at high density.¹⁵¹ The

application of strategies to mitigate photo-bleaching reactions could extend the time window for observation.^{152–155} These and related efforts are the subject of ongoing investigation.

3.3 Acknowledgments

M.J.S. thanks Dr. Joseph Barchi, NCI-CCR, for NMR assistance and Dr. James Kelley, NCI-CCR, for mass spectrometric analysis. This work was supported by the Intramural Research Program of the National Institutes of Health, National Cancer Institute, Center for Cancer Research. M.S. acknowledges funding by the DFG (ReceptorLight TRR 166). Dr. Luke Lavis, Janelia Research Campus, Howard Hughes Medical Institute, is acknowledged for assistance with fluorescence quantum yield determination and helpful discussions.

CHAPTER FOUR

THE JOURNAL OF ORGANIC CHEMISTRY

“DEFINING THE IMPACT OF CYANINE CONFORMATIONAL RESTRAINT IN THE NEAR-INFRARED RANGE”

4.1 Abstract

Appending conformationally restraining ring systems to the cyanine chromophore has been used to create exceptionally bright fluorophores in the visible range. Here we report the first application of this strategy to molecules in the near-infrared (NIR) range. We detail the preparation of the unsubstituted restrained heptamethine indocyanine bearing a unique pentacyclic ring system appended to the polymethine chromophore unit. Time-resolved absorption spectroscopy and fluorescence correlation spectroscopy verify that, unlike the corresponding parent unrestrained variant, the restrained molecule is not subject to photoisomerization. The room temperature emission efficiency and the fluorescent lifetime of the restrained cyanine are not extended relative to the parent cyanine, even in viscous solvents. This indicates that, in contrast to prior reports, the photoisomerization of heptamethine cyanines does not contribute significantly to the excited state chemistry of these molecules. We also find that the fluorescence lifetime of the restrained heptamethine cyanine is nearly temperature insensitive and is significantly extended at moderately

elevated temperatures relative to the parent cyanine. Finally, computational studies have been used to evaluate the impact of conformational restraint on atomic and orbital structure across the cyanine series. In total, these studies clarify the role of photoisomerization on the heptamethine cyanine scaffold, demonstrate the dramatic effect of restraint on the temperature sensitivity of these dyes, and will enable future efforts to optimize NIR dyes for various applications.

4.2 Introduction

Optical imaging in the near-infrared (NIR) range benefits from reduced autofluorescence and enhanced tissue penetration.¹⁵⁶ Improving the photon output of NIR fluorescent probes would be an enabling advance for many imaging applications. This is challenging because, as observed across multiple scaffolds, strategies that shift absorbance maxima towards longer wavelengths result in decreased fluorescence quantum yield (ϕ_F).^{157,158,159} Increased internal conversion as the S_0 - S_1 energy gap is decreased is a major element of this issue. However, chemical features embedded within the various dye classes also have dramatic effects on the emission properties of NIR dyes. As the magnitude of ϕ_F results from the interplay of multiple dye- and solvent-dependent pathways, it is important to clearly define the link between structure and emission efficiency.¹⁶⁰

Cyanine dyes are broadly used fluorescent probes, with applications that span single molecule to bulk tissue imaging.¹⁶¹⁻¹⁶² Unique to the cyanine dye class, two-carbon homologation extends the absorbance maxima in roughly 100 nm increments. The indocarbocyanines, including the broadly utilized Cy3, Cy5, and Cy7 series, form the

chemical backbone of many invaluable fluorescent reagents.¹⁶³⁻¹⁶⁴ While these dyes are defined by an exceptionally high absorbance cross-section, emission competes with a trans-to-cis photoisomerization pathway that can limit the photon output.^{161-162, 165}

Fusing a polycyclic ring system to block the possibility of photoisomerization is an appealing strategy. This approach was implemented first on the trimethine series by Wagoner et al. and, more recently, by us on the synthetically challenging pentamethine series.¹⁶⁶⁻¹⁶⁷ The resulting dyes are dramatically brighter with the tri- and penta-methine derivatives exhibiting $\sim 8\times$ and $\sim 4\times$ greater room temperature ϕ_F values, respectively (Figure 3.1A).¹⁶⁶⁻¹⁶⁷ The improved brightness of these restrained dyes is consistent with various spectroscopic observations suggesting photoisomerization is a major component of the excited state chemistry of these molecules.^{161-162, 168}

Given the need for brighter NIR fluorophores, improving the photon output of heptamethine cyanines is an important objective. However, the role of photoisomerization was less clear in this case and several seemingly paradoxical findings had been reported. Studies using a benzoxazole heptamethine cyanine observed a strong temperature dependence on emission, which was ascribed to increased photoisomerization with elevated temperature.¹⁶⁹ Also consistent with a role for photoisomerization, albeit non-quantitatively, transient spectroscopy studies directly observed the isomerized species, as does as an approach using gas phase mass spectrometry.¹⁷⁰⁻¹⁷¹ By contrast, a study looking at two highly substituted heptamethine cyanines found that room temperature emission was independent of solvent viscosity.¹⁶⁰ This observation suggests that, at least in these examples, the contribution of photoisomerization to non-radiative singlet state deactivation

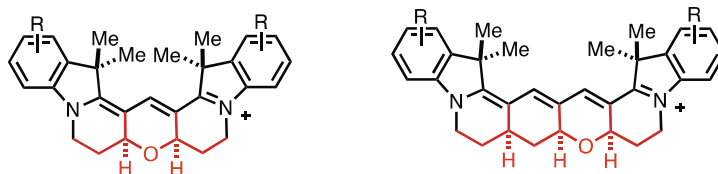
is insignificant. Finally, a single theoretical study found that the activation energy for isomerization in the excited state increases with polymethine length, potentially suggesting a less important role of photoisomerization for heptamethine cyanines compared to the shorter variants.¹⁶⁶

To address the ambiguity regarding the excited state photochemistry of these broadly used molecules, we have prepared and evaluated a conformationally restrained heptamethine cyanine. We detail the first preparation of the parent indocyanine, **2**, through an acid-catalyzed reaction that forms the pentacyclic ring system from an acyclic precursor in a single step (Figure 3.1B). Time-resolved transient absorption spectroscopy and fluorescence correlation spectroscopy (FCS) both confirm that, unlike the conventional heptamethine cyanine, compound **2** does not undergo excited-state isomerization. However, at ambient temperature, the restrained and parent cyanines exhibit similar ϕ_F and lifetimes (τ_F). Moreover, τ_F does not correlate with solvent viscosity in either molecule. Notably, however, the τ_F of **2** is nearly insensitive to temperature, and at moderately elevated temperatures significantly exceeds that of the highly temperature sensitive unrestrained variant **1**. This later observation is attributed to the temperature dependence of internal conversion and not photoisomerization, as suggested previously. Finally, computational studies analyze the impact of chromophore length and conformational restraint on orbital and atomic structure across the tri-, penta-, and heptamethine cyanine series. In total, these studies provide mechanistic insights that clarifies the relative contribution of polymethine isomerization and the role of solvent and temperature on the internal conversion kinetics in this important series of fluorescent probes.

4.3 Results and Discussion

In considering the design of a restrained heptamethine cyanines, several possible (poly)-dihydropyran and carbocyclic ring systems are feasible. We first examined the approach shown in equation 1, which involves the condensation of malonyldialdehyde with compound **4** or its partially cyclized variant. Despite examining a range of protic and Lewis acids with several malonyldialdehyde precursors, no stable polycyclic compounds were isolated. We then developed the retrosynthetic disconnection shown in Figure 3.1B

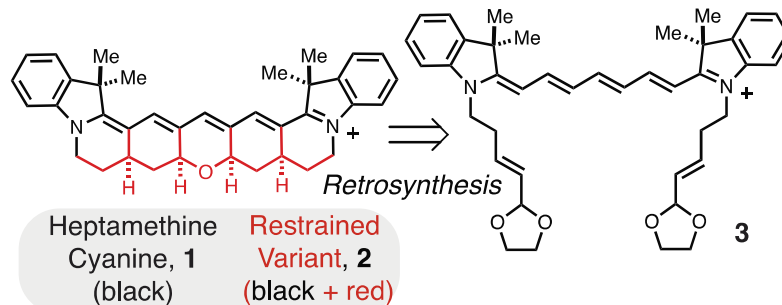
A. Prior Work - Cyanine Restraint in the Visible Range



Trimethine Cyanine (black) e.g. Cy3	Restrained Variant (black + red) e.g. Cy3B
$\Phi_F = 0.09^a$	$\Phi_F = 0.85^a$

Pentamethine Cyanine (black) e.g. Cy5	Restrained Variant (black + red)
$\Phi_F = 0.15^b$	$\Phi_F = 0.69^b$

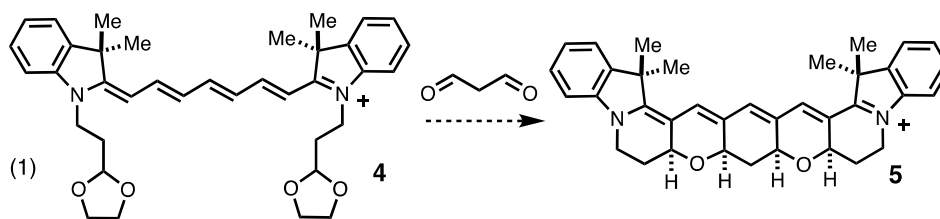
B. These Studies - Restrained Heptamethine Cyanines



Heptamethine Cyanine, 1 (black)	Restrained Variant, 2 (black + red)
--	---

Figure 4.1: Restrained Cyanine Structure. Prior restrained cyanines (A) and this study (B).
^a ϕ_F values in H₂O.^{166,172-173} ^b ϕ_F values in MeOH.¹⁶⁷

to compound **3**, which only contains a single dihydropyran ring. Notably, in our earlier synthesis of the pentamethine cyanine the introduction of carbocyclic ring and only single dihydropyran ring was critical to creating a stable molecule.¹⁶⁷ In this approach, we envisioned carrying out a tandem Michael addition/Prins-cyclization cascade from precursor **3** (Figure 3.1B). While this route is similar to that used to prepare the pentamethine variant, the pentacyclization reaction on the more hydrolytically sensitive heptamethine chromophore stands out as the critical, and likely highly challenging step.



The synthesis of **2** was carried out as shown in Scheme 1. We found that previously reported **6** could be converted to **6** in useful yield using the Hoveyda-Grubbs II catalyst.¹⁶⁷ Indolenine **7** and cyanine precursor **8** were combined efficiently to form cyanine **4** using standard cyanine preparative conditions (Ac₂O, Et₃N, DCM). The pentacyclization reaction proved difficult to optimize, but was ultimately found to proceed in modest, albeit reproducible yield through a two-step sequence involving initial formation of an mixture of diastereomers in 1:1 1 M HCl; THF at rt, followed by conversion to single, all-syn product **2**, 1:1 0.3 M HCl:MeOH at 60 °C.

We first evaluated the impact of conformational restraint using spectroscopic methods that directly assesses photoisomerization. As an unrestrained comparison for **2**, we have used the simplest heptamethine indocyanine hexamethylindotricarbocyanine

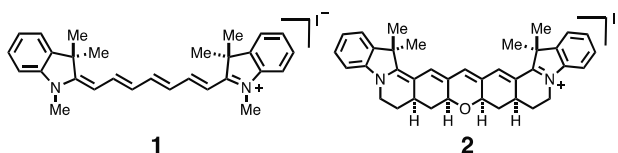
which have been previously used to characterize photoisomerization in Cy5 and other unrestricted cyanines.^{175,176} While the decay of the conformationally restrained **2** can be fitted with a pure diffusion model (Figure 3.2B), the decay of the parent heptamethine cyanine **1** shows a component with a small amplitude in the μs timescale not observed for **1** when measured under the same conditions. Fluctuations in the μs timescale were also observed in FCS studies of Cy5 and other unrestricted cyanines and attributed to photoisomerization. Although the amplitude of the fast component observed with **1** is quite small, the fact that this component is absent in the FCS decay of the restrained compound **2** suggests it is indeed due to the formation of a dark isomer. Together, the transient spectroscopy and FCS experiments indicate that photoisomerization occurs in **1** but not in **2**. We note that neither transient spectroscopy nor FCS are suitable methods to determine the efficiency of photoisomerization of **1** in a quantitative manner because the absorption cross sections of the isomers are unknown. Yet, the fact that signals are quite small suggests that the efficiency of isomerization may be small compared to the efficiency of other photophysical processes that depopulate the singlet excited state, including fluorescence and internal conversion.

We then examined the impact of conformational restraint on the emission properties of **1** and **2**. As shown in Table 3.1, the room-temperature ϕ_F and τ_F values are similar between the two dyes. The magnitude of differences between the two dyes is maximally greater by only 25% for the ϕ_F **2** in H_2O and is typically less than 10%. This is in stark contrast to the trimethine and pentamethine members of the family, where the restrained cyanines are significantly more fluorescent than their parent compounds. This suggests

that, in contrast to the shorter cyanines, isomerization does not play a major role in deactivating the excited state of **1**. Indeed, the excited state lifetime of **1** does not increase with increasing solvent viscosity as has been observed for many trimethine and pentamethine cyanines.¹⁷⁷ For example, while the fluorescence lifetime of trimethine indocyanine is *c.a.* 18-fold greater in glycerol than in water, the fluorescence lifetime of **2** is shorter in glycerol ($\tau_F = 0.83$ ns) than in all measured solvents except water.¹⁷⁸

Table 4.1: Spectroscopic and Photophysical Properties of **1** and **2**.

A. Key Structures



B. Spectroscopic Properties of **1** and **2**

	Solvent	λ_{\max} (nm)	ϵ (M ⁻¹ cm ⁻¹)	λ_{em} (nm)	Φ_F	τ (ns)
1	Methanol	740	270,000	772	0.24	0.91
	Glycerol	751	165,000	776	0.26	0.83
	DCM	756	266,000	788	0.46	1.6
	H ₂ O ^a	736	107,000	771	0.064	0.37
	D ₂ O ^a	735	136,000	771	0.20	0.97
2	Methanol	782	265,000	803	0.29	0.93
	Glycerol	794	134,000	808	0.28	0.83
	DCM	775	303,000	811	0.40	1.7
	H ₂ O ^a	775	106,000	795	0.081	0.38
	D ₂ O ^a	770	107,000	791	0.18	1.2

^aw/ 5% DMSO.

To analyze the role of solvent in greater detail, the rate constant for non-radiative deactivation (k_{nr}) was calculated from ϕ_F and τ_F as $k_{nr} = (1-\phi_F)/\tau_F$. Experiments with

various trimethine and pentamethine cyanines show an excellent correlation between k_{nr} and solvent viscosity. This observation has been interpreted in terms of frictional effects on the photoisomerization reaction of the unrestrained cyanines.^{177, 179} In contrast, k_{nr}

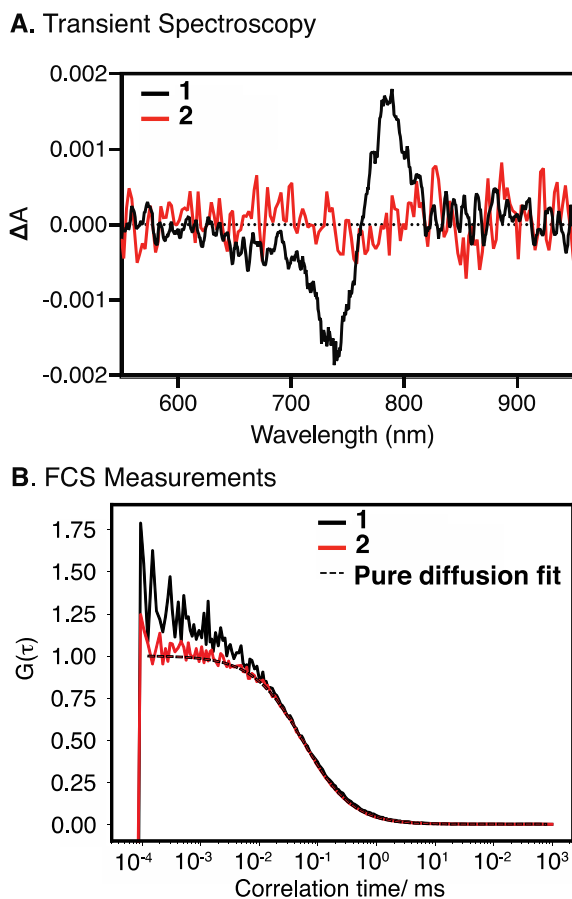


Figure 4.2: Transient Absorption of Parent and Restrained Fluorophore. Transient difference spectrum (A, in ethanol) and FCS (B, in aqueous buffer containing ROXS photostabilization system) measurements of **1** and **2**. The difference spectrum was recorded 50 ns after excitation. The FCS curve of **2** can be described by pure diffusion fit, while in the FCS curve of **1** we observed an additional component in the microsecond time scale which we attribute to photoisomerization.

values do not correlate with solvent viscosity for either **1** or **2** (Figure 3.3A). Most dramatically, k_{nr} values for **1** are almost the same in glycerol ($\eta = 1,412$ cp) and methanol

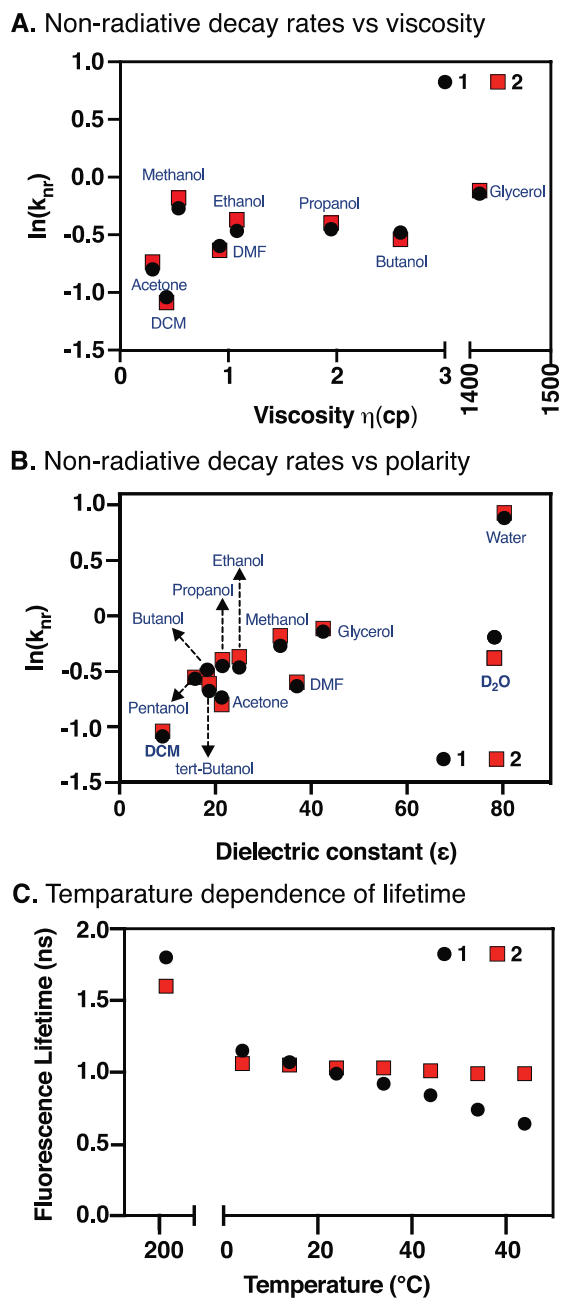


Figure 4.3: Solvent and Temperature Dependence of Parent and Restrained Fluorophore. Relationship between $\ln(k_{nr})$ vs. (A) viscosity and (B) dielectric constant. (C) Temperature dependence of fluorescence lifetime of **1** and **2** (in EtOH). Note the huge break in the x-axis of figure 3.3A to accommodate the glycerol data point.

($\eta = 0.54$ cp), and the differences between **1** and **2** are very small. These observations indicate that the rate-limiting step in the deactivation of the excited state of **1** does not involve large molecular rearrangements. Instead, there is a clear correlation between k_{nr} and solvent polarity (Figure 3.3B), which has not been observed in studies of the shorter cyanine dyes. Values of k_{nr} are higher in protic solvents compared to aprotic solvents of the same dielectric constant, suggesting hydrogen-bond assisted contributions to the non-radiative deactivation process. Differences are particularly striking for τ_F and ϕ_F in D₂O vs. H₂O for **1** and **2** (Figure 3.3B), as observed previously by Heilemann et. al. for several cyanines.¹⁸⁰ Overall, these observations highlight the significant role that internal conversion plays for singlet-state deactivation in the NIR range, and the dramatic role of solvent in mediating this process.

We then examined the role of temperature on the photon output of these dyes. Temperature-dependent lifetime measurements of **1** and **2** in ethanol are shown in Figure 3.3C. The τ_F of **2** is fairly insensitive to temperature, but the τ_F of **1** decreases with increasing temperature. Interestingly, this observation is similar to that made in the trimethine and pentamethine series, where this observation was linked to the photoisomerization of these dyes. In fact, this dependence has been used to calculate the activation energy of photoisomerization.¹⁸¹ However, in the case of **1**, this interpretation is inconsistent with the observation made above that τ_F and k_{nr} are independent of solvent viscosity. To resolve this apparent disconnect, we suggest the observed differences between **1** and **2** are due to temperature effects on the internal conversion rate of **1**, which are minimized in the conformationally restrained compound, **2**. Thus, conformational

restraint, which rigidifies the heptamethine cyanine chromophore, also limits the impact of increased temperature on internal conversion. It is interesting to note that the τ_F measured at 77 K is lower for **2** than for **1**, (1.6 vs. 1.8 ns, respectively), indicating that conformational restriction has a negative impact on the intrinsic radiative lifetime of the dye. This rationalizes the observation that the two dyes have very similar lifetimes at room temperature despite the fact that k_{nr} increases more steeply with temperature for **1** than for **2**.

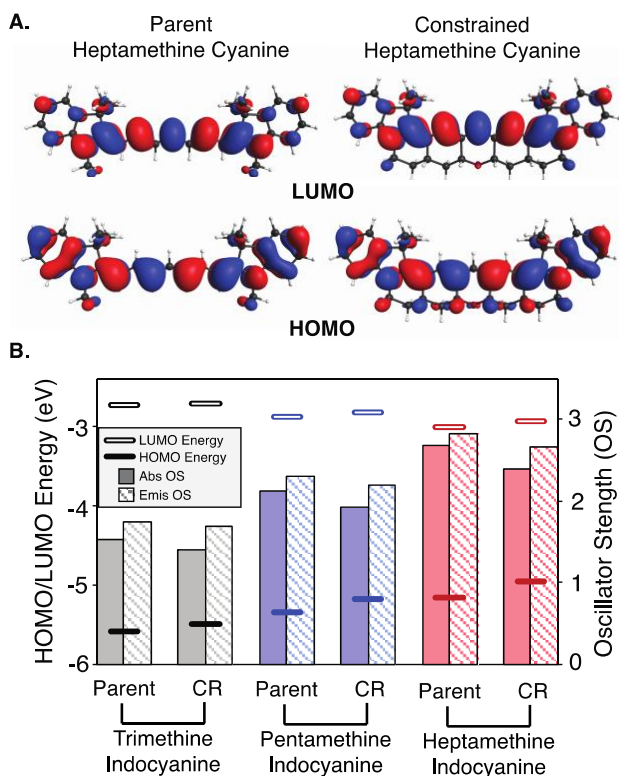


Figure 4.4: Computational Studies for Energy Levels. (A) HOMO/LUMO plots for **1** and **2** (contour values = 0.02 (electron/bohr³)^{1/2}); (B) computed B3LYP-PCM HOMO (lower bars) and LUMO (higher bars) energies (in eV, left axis scale) and TDDFT-B3LYP-PCM oscillator strengths (OSs) for absorbance (solid columns) and emission (striped columns) (right axis scale). Parent = conventional cyanine; CR = conformationally restrained cyanine.

These experimental results prompted us to carry the first computational analysis seeking to compare restrained and conventional cyanines. Full details and data are provided in the Supporting Information but in outline we have used time-dependent density functional theory^{182,183} with the B3LYP functional¹⁸⁴⁻¹⁸⁶ (TDDFT-B3LYP) and occupation restricted multiple active space with second-order perturbation theory (ORMAS-PT2).^{187,188} Solvent water effects were included via the polarizable continuum model (PCM)¹⁸⁹⁻¹⁹¹ and the GAMESS package was used for all calculations.^{192,193} We note that TDDFT methods have been used broadly to predict various aspects of cyanine chemistry, despite a systematic overestimation of orbital energies.^{195,196} In earlier efforts, we found that ORMAS-PT2-PCM accurately modeled modified heptamethine cyanine absorbance energies¹⁹⁷ and we sought to further compare the two methods in these studies. We found that both methods predict absorbance and emission energies that match exactly the experimentally observed trends, viz. 1) trimethine > pentamethine > heptamethine and 2) conventional > restrained. Overall, ORMAS-PT2-PCM absorbance energies are closer to experimental than TDDFT-B3LYP-PCM (mean unsigned errors (MUEs) are 0.143 and 0.377 eV, respectively) but surprisingly emission predictions are even more accurate for both (MUEs = 0.078 and 0.057, respectively). It is not clear why computed emission energies are more reliable, however, we note that the error differences cause TDDFT-B3LYP-PCM Stokes shifts to be less accurate than ORMAS-PT2-PCM. Nonetheless, both methods predict the correct trends and importantly (for discussion below) TDDFT singlet excited states represent almost pure single electron jumps from highest occupied molecular

orbital to lowest unoccupied molecular orbital, i.e., HOMO \rightarrow LUMO (see Supporting Information).

We then examined orbital structure to understand why there is a red shift when going from the parent to restrained cyanine, and why its magnitude increases when going from trimethine to pentamethine to heptamethine. As shown in Figure 3.4A, the B3LYP-PCM HOMOs and LUMOs appear mostly similar for the representative heptamethine case, albeit with a notable difference. Specifically, in the HOMO of the restrained variant, there is additional orbital density on the CH σ -bonds adjacent to the unsaturated chromophore. However, when examining the orbital energies (Figure 3.4B) we find that HOMOs become destabilized when going from parent to restrained and that this destabilization gets larger with increasing cyanine length. LUMO energies decrease with cyanine length and increase slightly when going from conventional to restrained but these changes are smaller than for the HOMOs. These orbital energy changes serve to explain the bathochromic shift of the restrained structures. In examining the impact of restraint on the structure of these compounds, we observed a clear trend in which the bond lengths of the core chromophore are slightly lengthened upon constraint (up to 0.008 Å) due to a compression of the bond angles (up to 4°). The magnitude of these effects correlates with chromophore length, being greatest in the heptamethine series.

Finally, we looked at TDDFT-B3LYP-PCM oscillator strengths, which is a dimensionless value to express the quantum probability of the transition between ground and excited states (Figure 3.4B). These values decrease by about 5-10% upon ring constraint, which may explain why the absorbance cross-section (ϵ) of the restrained dyes

are modestly lower across the series. This feature likely results, at least in part, from HOMO delocalization onto the CH σ -bonds adjacent to the unsaturated chromophore leading to loss of pure π symmetry and an energy penalty due to introduced nodes. Additionally, reduced excited state oscillator strengths suggests that the emission (ϕ_F) of the restrained dyes are somewhat lower than might be expected for simply removing the isomerization component of a typical cyanine. The impact of this computational observation is particularly apparent in low temperature emission comparison of **1** and **2**, where isomerization has been prevented in both cases and the τ_F of **1** exceeds that of **2**. In total, these studies demonstrate that conformational restraint impacts not only the capacity for photoisomerization, but also imposes notable effects on chromophore and orbital structure.

4.4 Conclusion

Here we detail the application of cyanine conformational restraint on the heptamethine scaffold. These studies reveal several features that distinguish the heptamethine cyanines from their trimethine and pentamethine congeners. First, while solvent viscosity strongly correlates with emission for unrestrained tri- and penta-methine cyanines, it does not in either the parent or restrained heptamethine case. This observation serves as conclusive evidence that photoisomerization does not meaningfully impact the room temperature excited state chemistry of the broadly used heptamethine cyanine dyes. While solvent viscosity is independent, solvent polarity strongly correlates with heptamethine emission – a trend that is not true for shorter cyanines. This latter observation highlights the outsized role of solvent-mediated pathways, particularly aqueous solvents,

have on internal conversion rates of these NIR fluorophores. Finally, despite not impacting photoisomerization, restrained, but not unrestrained, heptamethine cyanines exhibit nearly temperature independent emission. This indicates that the rigidifying ring system dramatically decreases the temperature dependence of internal conversion. The minimal temperature sensitivity of these dyes may have significant utility.

These studies have significant bearing on the future design of NIR dyes for biological use. As indicated by our computational studies, the placement of CH-bonds adjacent to the polymethine chromophore can impact HOMO/LUMO orbital structure and oscillator strength. These effects should be considered, along-side the standard considerations of unsaturated chromophore design. Furthermore, studies seeking to improve the photon output of NIR dyes, particularly in aqueous biological settings, should be conscious of the magnitude of solvent effects on internal conversion kinetics. One solution to this issue is the use of encapsulation strategies using engineered proteins or other organic/inorganic frameworks that serve to alter the local environment. While these have been studied extensively with visible range fluorophores,^{197,198} related efforts with NIR fluorophores are likely to be constructive and merit further investigation.

4.5 Acknowledgements

M.J.S. thanks Dr. Joseph Barchi, NCI-CCR, for NMR assistance and Dr. James Kelley, NCI-CCR, for mass spectrometric analysis. This work was supported by the Intramural Research Program of the National Institutes of Health, National Cancer Institute, Center for Cancer Research. Dr. Luke Lavis, Janelia Research Campus, Howard

Hughes Medical Institute, is acknowledged for assistance with fluorescence quantum yield determination This project has been funded in whole or in part with Federal funds from the National Cancer Institute, National Institutes of Health, under Contract No. HHSN261200800001E. M.L. acknowledges use of the UltraFast Laser Spectroscopy Facility at ASU.

CHAPTER 5

MOLECULAR BASIS OF DNA SEQUENCE-DEPENDENT URACIL REMOVAL EFFICIENCY INVESTIGATED BY FLUORESCENCE

5.1 Introduction

Studying the interlinkage between the physical properties of DNA and sequence dependence of DNA repair efficiency is a critical step towards understanding the molecular aspects of biomolecular functions. Base Excision Repair (BER) pathway which is responsible for repairing most DNA impurities caused by alkylation, oxidation and deamination of nucleobases from the DNA, keeping it mutation free. Uracil-DNA glycosylase (UDG) eliminates uracil (U) impurities from the DNA sequence by cleaving the N-glycosidic bond creating an abasic site which initiates the Base excision repair (BER) pathway, thus repairing the DNA.^{199,200} While previous studies point towards a DNA sequence dependence of how efficiently uracil is removed from the DNA, there is no clarity on physical basis of this dependence.²⁰¹⁻²⁰⁴ The goal of this study is to elucidate the physical properties of DNA which influence these sequence dependent uracil removal efficiency from DNA.

Fluorescence techniques can help in this respect by reporting about the local environment in desired parts of molecules through monitoring the changes in their environment-dependent photophysical properties.

5.2 UDG Function

Uracil is one of the four naturally occurring nucleobases in the nucleic acid RNA, where uracil base-pairs with adenine and replaces thymine during DNA transcription. However, uracil acts as an impurity in the DNA sequences introduced by spontaneous deamination of cytosine and incorporation of dUMP during replication. Cytosine deamination caused mutagenesis creates U:G mismatch whereas the dUMP incorporation in DNA sequence leads to U:A that can be cytotoxic and have reduced binding affinity of some transcription factors as compared to A:T, which can affect the gene expression.²⁰⁵ The mechanism of how UDG aids removal of uracil from the DNA sequence by cleaving the glycosidic bond follows a “pinch-push-pull” mechanism as shown in figure 5.1.^{206,207}

At first, the primary binding of UDG will almost inevitably be with undamaged DNA. After that, the enzyme engages in scanning until it either finds a lesion or falls off DNA. This scanning for uracil happens by UDG binding to the strand and slightly bending the DNA. A slight compression is created by a trio of serine residues, thus positioning the bases for detection and creating stress on the DNA.

The stress caused in the first step can be relaxed by the insertion of a conserved leucine side chain into the minor groove. This penetration into the DNA (push) and complementary interactions from the uracil recognition pocket facilitate final productive binding (pull). This recognition pocket shape complements the uracil structure, allowing for high substrate specificity. This specificity comes due to the pocket being small to fit in purines. The side chain of Tyr147 sterically interferes with the thymine C5 methyl group, making the complex unstable. Further, a specific hydrogen bond between the uracil O2

carbonyl and asparagine (Asn 204) discriminates against a cytosine substrate, which lacks the necessary carbonyl. It is worth noting that even though favorable interactions between UDG pocket.

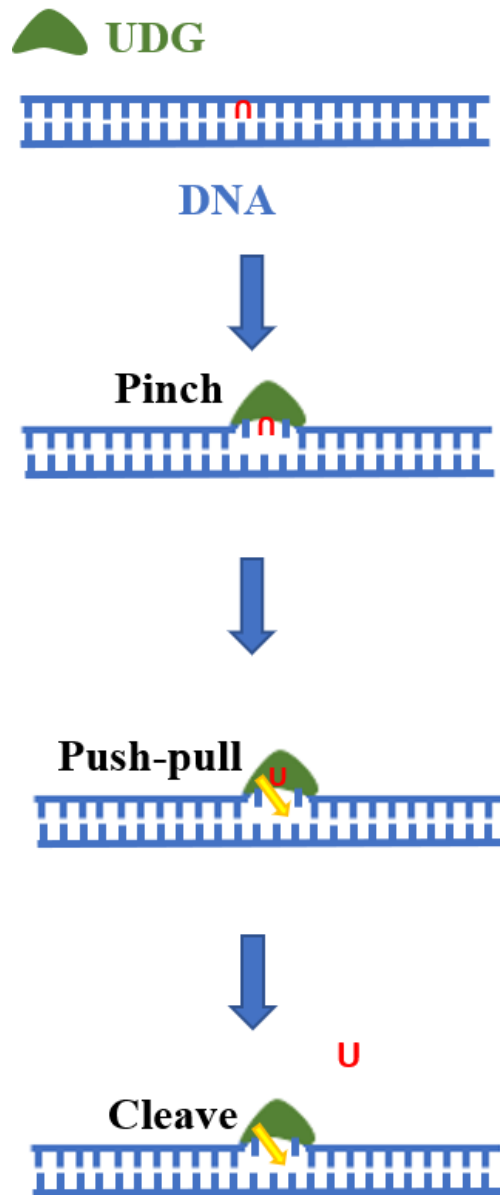


Figure 5.1: UDG Activity Mechanism. The red U in the sequence represents Uracil.

This recognition pocket shape complements the uracil structure, allowing for high substrate specificity. This specificity comes due to the pocket being small to fit in purines. The side chain of Tyr147 sterically interferes with the thymine C5 methyl group, making the complex unstable. Further, a specific hydrogen bond between the uracil O2 carbonyl and asparagine (Asn 204) discriminates against a cytosine substrate, which lacks the necessary carbonyl. It is worth noting that even though favorable interactions between UDG pocket and uracil, the flipping step requires major conformational changes that involve breakage of hydrogen bonds uracil forms with the complementary sequence base and the loss of stacking interactions.²⁰⁸ Once the Uracil is flipped out of the sequence, cleavage of the glycosidic bond proceeds, which is mediated by nucleophilic attack of water on the C-N glycosidic bond.²⁰⁹

5.3 Sequence Dependence and Interlink to Flexibility

Although the cleavage mechanism is well understood, detailed knowledge of efficiency and sequence specificity in DNA contexts remains a field of study. There have been studies to investigate sequence specificity of uracil removal and a paper in 1993 and 1995 strongly indicated that sequence specificity of DNA repair *in vitro* by uracil-DNA glycosylase from calf thymus and *E. coli*, respectively.^{201,204} Rate of removal of uracil by UDG from different contexts of DNA duplex varied by more than 10-15-fold. It was also observed that the sequence context on the uracil containing sequent was contributing more to this difference than the pairing of U in the complementary sequence (U:A or U:G). A general trend observed in both the studies indicated that contexts of 5'-(A/T)UA(A/T)-3' are generally good substrate for uracil removal were as 5'-(A/T)UA(A/T)-3' and 5'-

(G/C)U(T/G/C)-3' were poor substrates, respectively. 5'-TUA-3' gave the highest uracil removal rates and a U with a T to its 3' is usually poorly repaired and always so when guanine (G) or C is found 5' to the U. A:T-richness tends to improve repair whereas G:C richness has the opposite effect. Most recently, an experimental approach based on the large-scale photolithographic synthesis of uracil-containing DNA oligonucleotides was conducted in a study to comprehensively probe the context-dependence of uracil excision efficiency of UDG.²⁰² However, the physical basis to why this sequence dependence is observed is still not studied systematically. Our work attempts to relate this sequence-dependence to the local flexibility of DNA in the context of uracil.

As mentioned in the push-pull mechanism, there is an energy penalty for DNA bending and base flipping, caused by the distortion of base stacking and breakage of hydrogen bonds. These interactions are dependent on the physical properties of the DNA and there is evidence of this both in computational as well as the experimental studies. According to the computational studies, the base stacking energy is dependent on the base step and varies from -3 to -5 kcal/mol in an aqueous solution.²¹⁰ A molecular dynamics study shows coupling between DNA bending and base opening.²¹¹ Further an energy study shows that the stability of the flipped out base state is higher in the context of bent DNA.²¹² Together these studies suggest that more flexible DNA sequences would be a better substrate for UDG.

Although there have been separate studies of flexibility dependence and context-dependence of UDG activity, no systematic study has been done to correlate these studies. A study in 2002 did a computational analysis in terms of bending force constants showing

that AUA/TAT sequence has a lower bending force constant and hence more flexible than the GUG/CAC sequence.²¹³ This work correlates these flexibility parameters to the efficiency of uracil removal for the first time, although in a limited manner, as a comparative study between two oligonucleotides. This study also attempts to understand the molecular basis for the differences in fluorescence quenching of 2-AP in the two sequence contexts where 2-AP replaces adenine opposite the uracil. However, there are shortcomings in both the experimental lifetime results due to poor time-resolution of TCSPC setup and in the interpretation of this data as will be discussed in the next section.

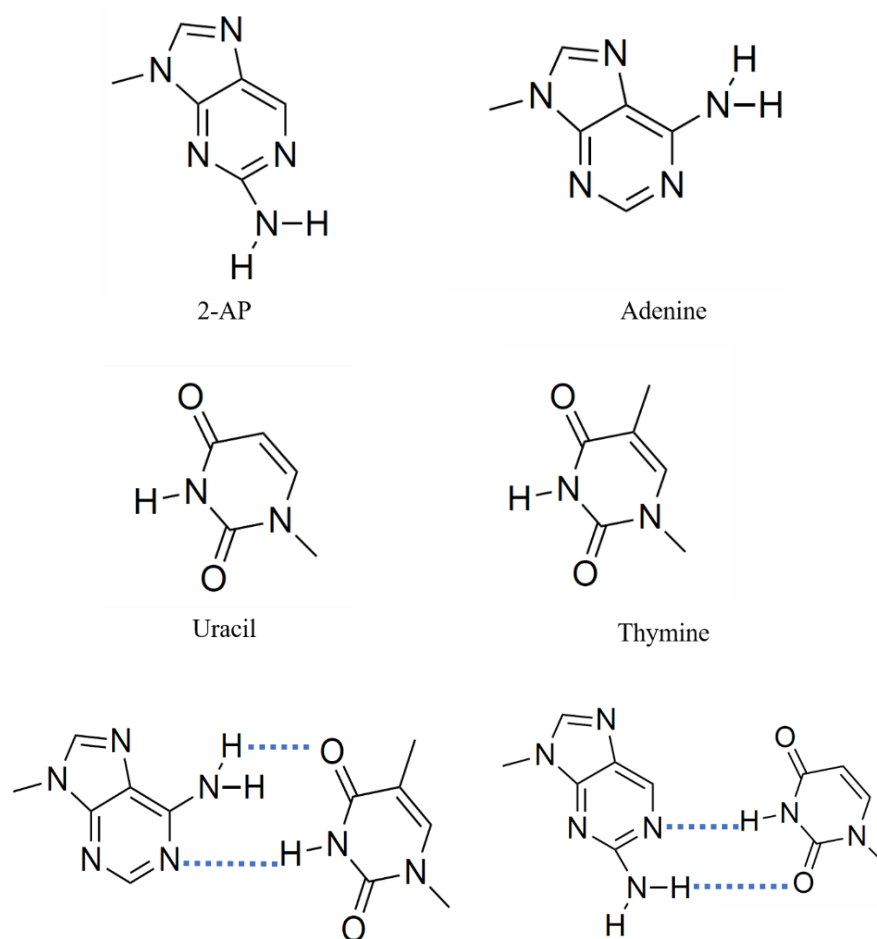


Figure 5.2: Structures and Hydrogen-Bonding. Structure of 2-AP, adenine (A), uracil (U), and thymine (T). The bottom panel shows hydrogen-bonding between A:T and 2-AP:U.

Apart from these, the study was conducted for a comparison of two sequences and is limited in a broader understanding of the molecular basis to Uracil removal efficiency by UDG.

5.4 Photophysical Properties of 2-Aminopurine

To study DNA physical properties using fluorescence spectroscopy, a fluorescent probe must be introduced into the system. The probe that is both used in this chapter is 2-aminopurine (2-AP). This molecule is a structural analogue of adenine (6-aminopurine) and can be inserted into the DNA duplex in place of one of the native DNA bases during the preparation of synthetic DNA. 2-Aminopurine (2-AP) and adenine are only different in the position of the exocyclic amine group as shown in figure 5.2, but the quantum yield of 2-AP is about a thousand times better than adenine with a quantum yield of 0.68 for 2-AP in aqueous solution, compared with $\sim 10^{-4}$ for adenine.²¹⁴ It is reported that Watson-Crick base-pair are formed between 2-AP and thymine (shown in figure 5.2) in the crystal structure of duplex and it has shown that the presence of 2-AP has a negligible effect on base stacking through NMR studies. Furthermore, the absorption maximum at $\sim 303\text{nm}$, lies to the red of the absorption of the nucleic bases and aromatic amino acids, allowing the excitation of 2-AP selectively in presence of DNA, RNA, and proteins.

The huge difference between the photophysical properties of 2-AP and adenine has been explained by the presence of a conical intersection between S_1 and S_0 in the energy landscape of adenine which facilitates non-radiative transition.²¹⁵ The possible explanation for why radiative pathway is more prevalent in 2-AP is that the conical interaction, however present in 2-AP, is blocked due to potential energy barriers, thus making the radiative pathway more prevalent. A supporting study showed that the height of the barrier to the

conical intersection is increased by hydration of 2-AP molecule and was in line with the experimental observation of increased quantum yield in polar solvents.²¹⁶ This picture of 2-AP energy landscape was challenged by a study later where it was shown that 2-AP is barely fluorescent ($\phi_F = 0.005$) in the gas phase.^{217,218} These computational studies further provided the evidence of decay to a close-lying $^1n\pi^*$ dark state is the main route of non-radiative transition in 2-AP and the polarity dependent properties are because $^1n\pi^*$ is shifted to higher energy, contributing to non-radiative decay less. However, there are no definitive experimental studies for the effect of solvation on the relative energies of the first excited state and $^1n\pi^*$ states. There is also evidence of intersystem crossing to the long-lived lowest triplet and its significant contribution to the polarity dependent and hydrogen-bonding dependent sensitivity of 2-AP photophysics.²¹⁹

5.5 2-AP as a Probe of the DNA Duplex

The fluorescence response of 2-AP is extremely sensitive to its molecular environment. Hence, it is potentially an ideal probe of the structure and function of DNA and has been employed in many studies over the last few decades.²²⁰⁻²²⁹ When 2-AP is substituted for a natural base in DNA, it displays an emission band with a maximum at ~370 nm that is unchanged in spectral characteristics from that of the free 2-AP. However, stacking in the polynucleotide duplexes causes quenching of 10 to 100-fold (based on the context the base analogue is placed in) relative to the free base as shown in figure 5.3. It is known that the photophysical properties of 2-AP are dictated by the π -stacking interactions and inter-strand hydrogen bonding that the molecule experiences to a great extent. Several papers have reported upon how this quenching efficiency is dependent on how the 2-AP is

stacked in the sequence, and thus, on the local DNA conformation.^{222,226,227,230} Furthermore, perturbation in the DNA duplex structure due to causes such as protein binding increases the 2-AP emission intensity and hence, been used for many protein activity assays, some studying intensity-based studied for base flipping proteins.^{231–233}

Researchers in past have studied the complex relationship between environment of 2-AP and its photophysical behavior to monitor base flipping. While different studies gave an increase in the intensity caused by base flipping, the real picture of conformations that 2-AP can take in DNA duplex is difficult to interpret as the fold increase using different base-flipping proteins has been determined to be different. For example, increases in fluorescence intensity of 54-fold and 14-fold are observed for M.HhaI and M.TaqI both, respectively, despite using saturating enzymatic conditions.²³² Both these proteins are from the class of methyltransferase where the mechanism involves base flipping in the DNA sequence. The specific interactions that can be formed between the 2-AP and its environment are complex and cannot be answered by steady-state fluorescence intensity. The population of 2-AP is a mixture of different conformation in the DNA duplex and cannot be interpreted from an average signal from steady-state measurement.

Thus, a time-resolved measurement can help probe this issue better. The lifetime measurements of 2-AP fluorescence have been used as an important source of information for the structure and dynamics of its environment. An interesting feature of 2-AP photophysics lies in not only a dramatically shortening of fluorescence decay lifetime when placed in a DNA context (shown in figure 5.3) but also a heterogeneous, multi-exponential decay function which is in strong contrast to free 2-AP, which has a mono-exponential

decay with lifetime being 10.2 ns.²³⁴ The 2-AP placed in a DNA context gives four components in the exponential fit, pointing towards a widely heterogeneous population of 2-AP being present. The trend in the lifetime component is the more stacked 2-AP is in the sequence, the shorter the lifetime, and this trend is represented as a cartoon in figure 5.4. The fact that the increase in intensity is not so great for flipping by M.TaqI as it is for M.HhaI (54-fold and 14-fold are observed for M.HhaI and M.TaqI, respectively) cannot be readily explained from steady-state data alone. In contrast, the time-resolved decay response of 2-AP to base flipping by M.TaqI is dissimilar to that seen for base flipping by M.HhaI in terms of the population distribution of different components, representing different orientations of 2-AP in the sequence.^{224,235} The shortest component corresponds to the most stacked and hence, most quenched sequence, and the longest lifetime component corresponds to the freest and hence, least quenched component. The fluorescence response of the 2-AP population complexed by M.HhaI is dominated by a slow ~11 ns component, whereas that of the 2-AP population complexed by M.TaqI decays much more rapidly, with an average lifetime of around 0.5 ns. Most notably, the very short decay component, characteristic of a stacked 2-AP population is completely absent from the decay of the MTaqI-complexed DNA duplex which was the majority of the population in DNA alone (81%). Therefore, the differences that are observed in the time-resolved and steady-state fluorescence responses of these systems to base flipping are not related to whether the base flipping is happening or not but are derived from the fact that the 2-AP is being flipped into distinct atomic environments in M.HhaI and M.TaqI. This study thus,

highlights that 2-AP can be used to get more insight into the local environment and is very sensitive to these environmental changes.

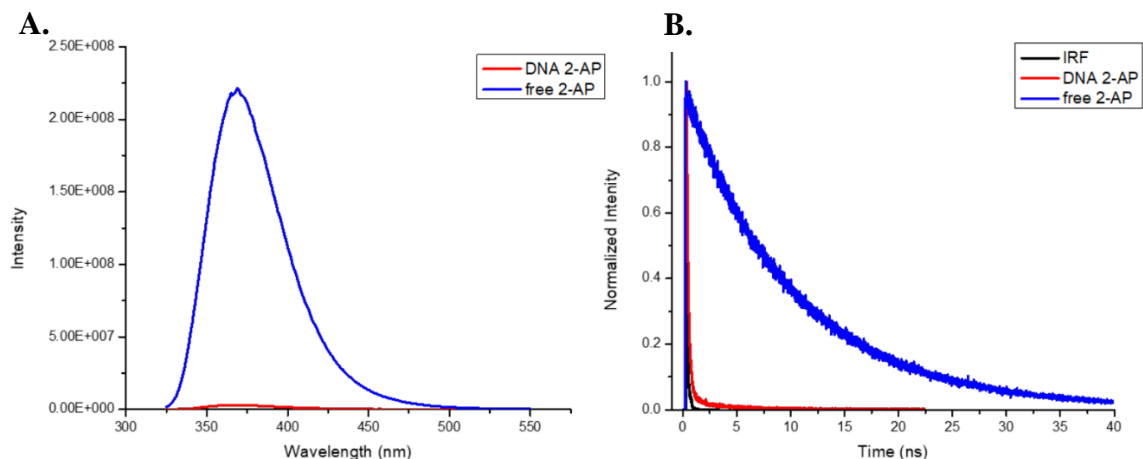


Figure 5.3: Quenching of 2-AP Fluorescence Placed on DNA. Change in (A) Fluorescence intensity of same concentration and (B) Lifetime decay of DNA containing 2-AP and free 2-AP.

The origin of the quenching mechanism of 2-AP in DNA structure is still a topic of debate and there is multiple literature present on the topic. One explanation by Barton group suggests that this quenching is related to the possibility of charge transfer from Guanine to an excited state of 2-AP, which can happen over distances upto 14 Å.^{236–239} It was also reported that this electron transfer is enabled if bridging bases are adenine and attenuated in presence of pyrimidines. Also, charge transfer efficiency shows directionality, being better for 3' to 5' transfer compared to 5' to 3'. One feature of charge transfer that is crucial to this study is how the conformational fluctuations of the duplex facilitate charge transfer. This was established by showing that the frozen DNA duplex shows a dramatic reduction in 2-AP quenching.^{225,239} However, the extent to which excited

2-AP in DNA is quenched by charge transfer (CT) with the other natural bases and the contribution of other non-CT processes is still a field of study. Recently, experimental work has shown that photoinduced CT can happen between all the natural bases and 2-AP.²⁴⁰ Many studies afterward found this ultrafast decaying component or a component that is too fast to measure in typical decay measurements.^{220,224,241} This conclusion of the ultrafast decaying quenched component was identified due to observed discrepancies between the fluorescence quantum yields determined from steady-state intensity measurements and those from the measurement of time-resolved decay parameter. This observation points towards the presence of decay processes that are too fast to be observed in typical lifetime measurements due to instrumental resolution (lifetimes less than about 10 ps). This component of quenched species will be addressed as “ultrafast-decaying dark species” and will be denoted as α_0 in this chapter. α_0 has been a comparatively new discovery in the field of 2-AP photophysics and there are only a few 2-AP-DNA studies reported with it. However, in all these studies, a common theme remains that it’s a major component (10-90% of the population) and represents the most well-stacked 2-AP in the sequence.^{220,234,241} With ever-improving time resolution in fluorescence lifetime measurements, species once deemed to be non-fluorescent are now observable and reported in the literature for few 2-AP systems.^{242,243}

The origin of this most quenched species has been a point of debate in the field. The 2002 paper and work before that in 2001 suggest that the whole ultrafast-decaying dark species (α_0) is a contribution from static quenching of 2-AP.^{213,244} However, a study in 2007 probed the nature of α_0 i.e., whether it’s static quenching or very fast dynamic

quenching.²²⁰ This paper uses the effect of viscosity to discriminate between static and dynamic quenching since only dynamic quenching is affected by viscosity. α_0 dramatically decreased at high viscosity, demonstrating that α_0 component of the population is caused by dynamic quenching.

It should be noted that the presence of these four populations is not proof of only four distinct or fixed conformations in which 2-AP can exist in the DNA context but just

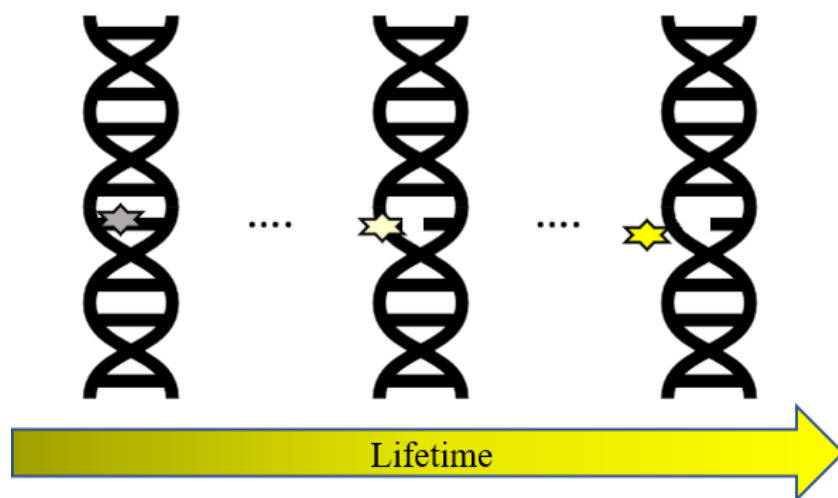


Figure 5.4: Cartoon Representation of 2-AP Population on DNA. 2-AP lifetime going from most stacked to least stacked from left to right. The arrow at the bottom represents lifetime going from low (grey) to high (yellow).

the minimum number of components needed to fit the decay with an exponential fit. There can be a wide variety of intrahelical stacked, intrahelical unstacked, and extrahelical states 2-AP can be present in the sequence. There are multiple ways to interpret the complex fluorescence decay data and determining the most appropriate kinetic scheme with which to interpret the data is not trivial.^{245–248} There are both, deterministic approaches, such as the commonly used iterative reconvolution method which is used further in this chapter, and probabilistic approaches, such as the smoothed exponential series method, the

maximum entropy method which can be used.²⁴⁷ Other functions such as the Lorentzian have also been used in certain studies and there are more complex models being developed that better capture the interplay between conformational dynamics and distance-dependent emission quenching.^{246,249} No single method is preferred universally, and there is likely to be value in using a combination of multiple methods when there is ambiguity in the interpretation of the results and the goal of this project is to use a probabilistic approach in conjugation with the deterministic approach in future. However, for the initial study, a simplistic picture is enough to distinguish the populations in terms of rigidity, where the populations are fitted with four components and the shorter the lifetime components are considered more stacked or rigid it is in the sequence.

Hence, it's evident from the literature that there is a gap in understanding the molecular basis of observations showing sequence dependence for uracil removal efficiency by UDG. Furthermore, the lifetime analysis in these papers lacks reporting a crucial term of ultrafast-decaying dark species (α_0), which is a major component of the 2-AP population distributing in double-stranded DNA and represents the most quenched, and hence the most stacked 2-AP population. As this 2-AP is placed opposite the uracil, this component can be a good reporter of how rigid the uracil context is for a given sequence. In this study, DNA base analog 2-AP is being used to establish the link between DNA rigidity and repair efficiency of base-flipping DNA repair proteins such as UDG. The hypothesis that UDG activity is dictated by the intrinsic local deformability of the DNA sequence around the uracil. This work hypothesizes that a larger α_0 represents a more rigid uracil environment and should make the flipping of uracil base out of the sequence by UDG

more difficult, thus decreasing the uracil removal rate. Therefore, sequences that maintain uracil in a rigid DNA context should be a poorer substrate for UDG.

5.6 Materials and Methods

A. Chemicals and Sequences

Free 2-Aminopurine (2-AP) (CAS Number 452-06-2) was purchased from Sigma-Aldrich and all the DNA sequences were purchased from Integrated DNA Technologies (IDT). The sequences were based on a previous study where DNA repair in vitro by uracil-DNA glycosylase from *E. coli* was reported.²⁰¹ Modification of the sequence mentioned in the paper is being used as a starting point to check if the kinetic data collected by us reflects the same trend. All the oligonucleotide sequences used in this study are mentioned in table 1 and contain 2-AP as we are using the fluorescence signal for both kinetics and flexibility studies. Sequences are 39-nucleotide long and named in order of the uracil removal efficiency reported in the paper, from **1** (100% uracil removal efficiency) to **4** (12% uracil removal efficiency). **2** and **3** gave 50% and 37% uracil removal rate, respectively. To probe the directionality effect of the immediate two more sequences with just the flanking bases reversed are studied for the extreme sequences **1** and **4** and are called **1 rev** and **4 rev**, respectively.

These sequences were then annealed at room temperature and progress of annealing was monitored using fluorescence decrease as the 2AP in dsDNA is more quenched than 2AP in ssDNA. 10-20% excess of uracil (U) containing sequence was used to make sure no excess 2-AP containing ssDNA remains in the solution. Two buffer conditions were used for these studies in order to check for consistency. TRIS buffer (pH 7.5, 20 mM TRIS,

10mM Sodium Chloride, 5mM Magnesium Chloride) and PBS buffer (pH 7, 20 mM Sodium Phosphate, 100 mM Sodium Chloride). All the 3 sections gave consistent results in both the buffer systems. Henceforth, the results shown here are in the PBS buffer.

Table 5.1: Sequences Used in Initial Studies. “Seq” refers to sequence name. The top part in the cell shows uracil (/ideoxyU/) containing strand and the bottom one shows 2-AP (/i2AmPr/) containing complementary strand. Sequence is reported from 5’ to 3’.

Seq	Sequence (5'-3')
1	CTA TAT TGG AAG CTT GCA T/ideoxyU/A ATG ACT CTG TAC ACG AAG CTT CGT GTA CAG AGT CAT T/i2AmPr/A TGC AAG CTT CCA ATA TAG
2	CTA TAT TCG CAG CTT AAC T/ideoxyU/A CAT TCT CTC AAC ACG CTT AAG CGT GTT GAG AGA ATG T/i2AmPr/A GTT AAG CTG CGA ATA TAG
3	CTA TAT TGG AAG CTC TGC A/ideoxyU/T AAT GCT CTG TAC ACG AAG CTT CGT GTA CAG AGC ATT A/i2AmPr/T GCA GAG CTT CCA ATA TAG
4	CTA GAA TGG AAG CTT GAA A/ideoxyU/T GTT ACT CTG TAC ACG AAG CTT CGT GTA CAG AGT AAC A/i2AmPr/T TTC AAG CTT CCA TTC TAG
4 rev	CTA GAA TGG AAG CTT GAA T/ideoxyU/A GTT ACT CAG TAC ACG AAG CTT CGT GTA CTG AGT AAC T/i2AmPr/A TTC AAG CTT CCA TTC TAG
1 rev	CTA TGT TGG AAG CTT GCA A/ideoxyU/T ATG ACT CTG TAC ACG AAG CTT CGT GTA CAG AGT CAT A/i2AmPr/T TGC AAG CTT CCA ACA TAG

B. Kinetic Assay

There are multiple assays reported in the literature for measuring UDG activity. However, as 2-AP is being used to find a link between photophysical characteristics and DNA flexibility, an assay involving 2-AP is being used for the kinetics study as well. In this assay, the analogue 2AP is opposite uracil in the complementary strand, and upon cleavage of the glycosylic bond of the uracil by UDG, an increase in 2AP fluorescence is observed as shown in figure 5.5. Initial velocity is the rate of formation of product ($v_o = d[P]/dt$), the product being uracil removed sequence. It is known that if left for an infinite amount of time all the uracil will be removed from the sequence. So, the mass balance at time $t=0$ and $t=\infty$ become,

$$[S]_{Tot} = [S]_o = [P]_{\infty} \quad (5.1)$$

The change in fluorescence follows the trend shown in figure 5.5 (B) and the total change in fluorescence (F at $t = \text{infinity}$ minus F at $t = 0$) should be proportional to the amount of product that is present. K is the proportionality constant.

$$F_{\infty} - F_0 = \Delta F = K[P]_{\infty} \quad (5.2)$$

Rearranging equation 5.1 and 5.2,

$$K = \frac{\Delta F}{[P]_{\infty}} = \frac{\Delta F}{[S]_o}$$

A more general form of equation 5.2 can be written at any time = t ,

$$F_t - F_0 = K[P]_t \quad (5.3)$$

Taking the first derivative of both sides with respect to time and substituting $v_o = d[P]/dt$, we get,

$$\frac{dF}{dt} = K \frac{d[P]}{dt} = K v_o \quad (5.4)$$

Substituting the proportionality constant K with equation 5.4,

$$\frac{dF}{dt} = \frac{\Delta F}{[S]_0} v_o \quad (5.5)$$

Rearranging the equation, we get,

$$\left(\frac{dF}{dt}\right) \left(\frac{S_0}{\Delta F}\right) = v_o \quad (5.6)$$

Therefore, the initial velocity will be found for all the sequences by finding the initial rate of fluorescence increase (the linear portion of the graph), dividing it by the total change in fluorescence, and multiplying it by the concentration of the initial substrate. The final goal is to determine k_{cat} (catalyst rate constant) and K_M (Michaelis constant), by doing substrate concentration-based assays for all sequences.

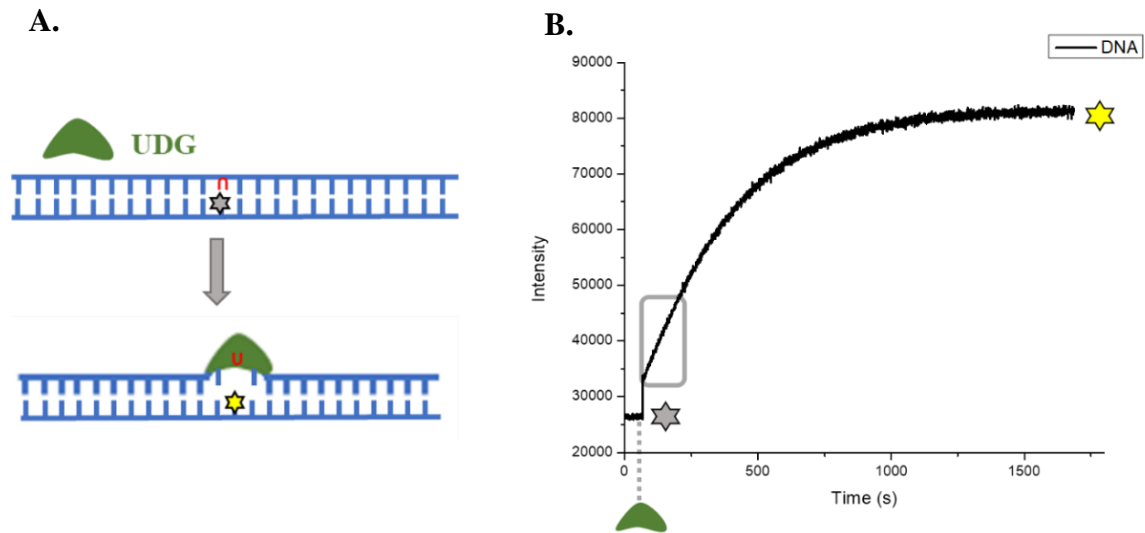


Figure 5.5: 2-AP Based UDG Kinetic Assay. (A) Cartoon representation of increase in 2-AP fluorescence intensity when UDG binds to DNA and (B) Steady-state fluorescence assay where UDG is added to the DNA solution at the grey dotted line.

C. Measurement of Quantum Yield of DNA Sequences

A previously published DNA sequence²⁵⁰, mentioned in table 5.2 as a reference, with a known value of quantum yield (0.013) in PBS buffer was used to establish optimum parameters for ϕ_F measurements. Fluorescence quantum yield (ϕ) was determined as:

$$\phi = \phi_R \frac{I (1 - 10^{-A_R}) n^2}{I_R (1 - 10^{-A}) n_R^2} \quad (5.7)$$

where the subscript R refers to the standard used as a reference for initial parameter determination is free 2-AP in water with $\phi_R = 0.68$, I represents the integrated corrected fluorescence spectrum, A is the absorbance of the solution at the excitation wavelength used to determine I , and n is the refractive index of the solvent. The refractive index term can be omitted in this case as we are using same buffer for all our quantum yield measurements.

Table 5.11: Quantum Yield Reference Sequence. “Seq” refers to sequence name. The top part in the cell shows uracil (/ideoxyU/) containing strand and the bottom one shows 2-AP (/i2AmPr/) containing complementary strand. Sequence is reported from 5’ to 3’.

Seq	Sequence (5’-3’)
Reference	T containing sequence: TGG CGC CCG AAT AGG GAC
	Complementary sequence: GTC CCT /i2AmPr/TT CGG GCG CCA
	Natural complementary sequence: GTC CCT ATT CGG GCG CCA

It was established that 315 nm is a good excitation wavelength as the contribution of natural bases absorbance is not present in this place for the absorbance spectrum of dsDNA without 2-AP (prepared by annealing T containing sequence with natural

complementary sequence as shown in table 5.11). The general approach of 1:10 dilution which was used in previous chapters for relative quantum yield calculations is not used in this study as it will require high DNA concentrations ($\sim 100 \mu\text{M}$) and a different approach of taking an average of multiple measurements to get an accurate absorbance value was taken. To check the variability in the absorbance measurement in the range of 0.05-0.06 in UV-VIS spectrophotometer (Shimadzu UV-1700 PharmaSpec), five spectrums of the same concentration of reference DNA sequence containing 2-AP were made, giving a standard deviation of less than 3% at 315 nm. Thus, concentrations of DNA ($\sim 10 \mu\text{M}$) which give absorbance in this range (0.05-0.06) can be used for absorbance and directly to measure the emission spectra as the inner filter artifacts are minimized in these absorbance ranges. The emission spectrum was then collected from 325nm to 550nm. It is important to subtract the background (emission spectrum of the buffer) as the emission spectrum is contaminated by the Raman peak at $\lambda_{\text{R}} = 352 \text{ nm}$ for $\lambda_{\text{EX}} = 315 \text{ nm}$ ($1/\lambda_{\text{R}} = 1/\lambda_{\text{EX}} - 3.4 \times 10^{-4} \text{ nm}^{-1}$).

To check the accuracy and precision of ϕ measurement five trials were performed and a value of 0.013 was obtained with a relative standard deviation of less than 5%, matching the reported value for the reference DNA sequence as shown in table 5.9.

Further, as the general trend is that dsDNA has quantum yields 2 order of magnitude lower than free 2-AP, it was decided to select one of the sequences in table 5.1 a reference for all the other quantum yield measurements of DNA sequence. For this, it is vital to acquire an accurate value of quantum yield for the new reference with respect to free 2-AP. **1 rev** was chosen as the new reference, and an average of four measurements gave a quantum yield of 0.01, a relative standard deviation of less than 5%, was set as the new

reference. Quantum yield measurements for all the other sequences were conducted with respect to this new reference four times and the average is taken as the quantum yield values.

D. Lifetime Measurements

Time-resolved fluorescence measurements were performed to determine the population distribution of 2-AP present in different DNA contexts with the TCSPC technique using the excitation pulses at 310nm. The laser beam was generated by a mode-locked Ti:Sapphire laser (Mira 900, Coherent) pumped by a frequency-doubled Nd:YVO4 laser (44% from an 18 W Verdi, Coherent). The 130 fs light pulses (at 800 nm with a repetition rate of 250 KHz) were generated by a regeneratively amplified Ti:S laser system (RegA 9000, Coherent Laser). The pulses were sent to an optical parametric amplifier (OPA) to generate the excitation light at the 620 nm then frequency doubled to obtain the excitation at 310 nm. A lifetime of free 2-AP solution in water was measured in a 25 nm time window to confirm a monoexponential fit with a lifetime of 10.2 ns, the same as reported in the literature.²³⁴

Fluorescence decay curves for dsDNA were collected for an excitation wavelength of 310 nm at three different emission wavelengths (380, 390, and 400 nm). This approach helps in having three data set to fit globally during iterative reconvolutions, increasing the robustness and accuracy of the fitting. This approach is especially useful when the population distribution is complex (with more than three components) where lifetimes can often be varied to compensate for pre-exponential factors and vice-versa. Photons were collected till 3000 counts in the peak channel on two timescales (3.3 ns and 25 ns). This

two-timescale data collection approach is useful when the lifetime distribution ranges from picosecond to 10 ns time scales, to take full benefit of the high resolution of the instrument in getting shorter components accurately while getting longer components using long time range decay. The maximum count rate was adjusted to be less than 5000 counts/second for samples and less than 1000 counts/second for IRF to avoid the pulse pile-up effect.

The following equation was used to get the lifetime components:

$$I(t) = I_0 \sum_{i=1}^n A_i e^{-t/\tau_i} \quad (5.8)$$

where n is the minimum number of terms that result in random residuals, and A_i ($\sum_{i=1}^n A_i = 1$) is the fractional weight of each lifetime, τ_i . Intensity decays were fitted using ASUFIT, a MATLAB-based program developed at ASU that uses a standard reconvolution procedure and nonlinear regression. The goodness of the fit was judged by the χ^2 value close to 1 and the randomness of the residuals. Initially, global fits for the 3.3 ns timescale were calculated. The two shortest lifetime components from this fit was then fixed in the global analysis of the decays collected on the 25 ns timescale.

Fits for both the global analysis and those for individual decay curves were carried out by initially attempting to fit the simplest (single exponential) model to the experimental data. The background values used in fitting were estimated from the number of photons arriving before the rising edge of the IRF and were fixed during the fitting procedure by the program. Three lifetime components were obtained by fitting the 3.3 ns window decay globally. However, this fitting does not capture the longer decaying population components and hence, further, a global analysis of 25 ns time window data was conducted, fixing the two of the shorter components and adding one more component. As shown in figure 5.6,

three components do not give a random residual and four components are essential for a good fit.

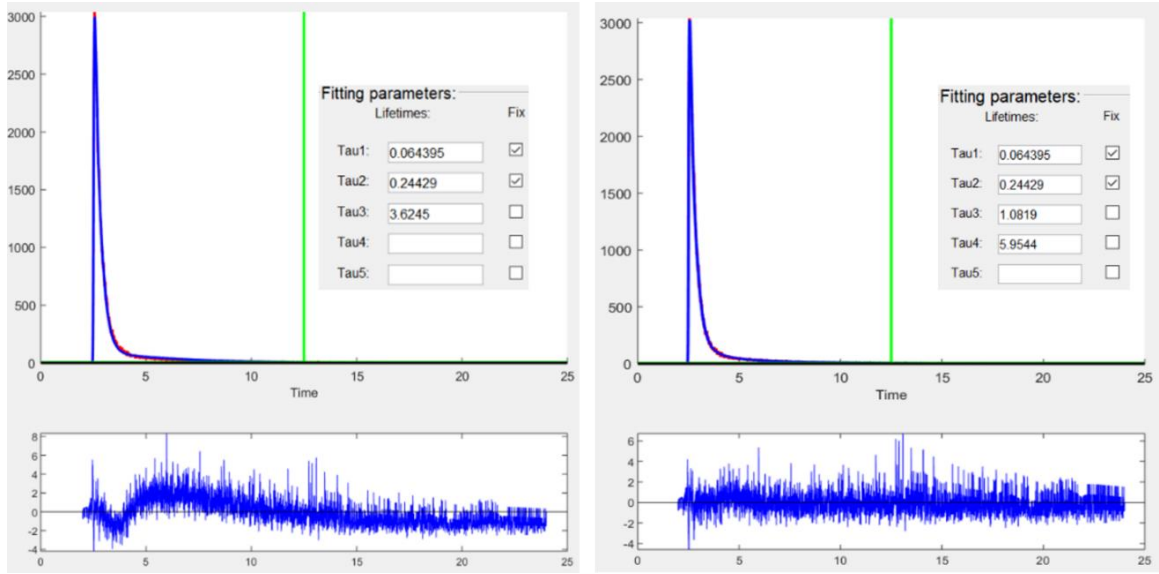


Figure 5.6: Residual Comparison for Three and Four Lifetime Components Fit. The left snapshot of the fitting software shows the fitting with three lifetime component fitting and right shows four-component fitting.

The sum of all the observed amplitudes was taken and individual observed amplitudes were divided by this sum to get the fractional amplitude of each component, A_i ($\sum_{i=1}^n A_i = 1$). The fractional amplitudes obtained for the four components are slightly different for data collected at three different emission wavelengths and are shown in Tables 5.3 through 5.8. The average of the fractional amplitudes for these three datasets was taken to report the average amplitudes (A_1, A_2, \dots) as shown in table 5.10. Finally, the average lifetime $\langle \tau \rangle$ was calculated from the average amplitude and lifetime components using $\langle \tau \rangle = \sum_{i=1}^n A_i \tau_i$.

Table 5.3: Parameters Derived From the Globally Fitted Decays of Sequence **1 Rev.**

Emission wavelength (nm)	A ₁	A ₂	A ₃	A ₄
380	0.422	0.477	0.096	0.005
390	0.396	0.502	0.096	0.006
400	0.386	0.508	0.099	0.007

Global Lifetime: $\tau_1= 0.07$ ns, $\tau_2= 0.31$ ns, $\tau_3= 1.00$ ns, $\tau_4= 6.09$ ns

Table 5.4: Parameters Derived From the Globally Fitted Decays of Sequence **1.**

Emission wavelength (nm)	A ₁	A ₂	A ₃	A ₄
380	0.751	0.238	0.008	0.003
390	0.686	0.300	0.009	0.004
400	0.687	0.296	0.011	0.005

Global Lifetime: $\tau_1= 0.03$ ns, $\tau_2= 0.12$ ns, $\tau_3= 1.46$ ns, $\tau_4= 5.83$ ns

Table 5.5: Parameters Derived From the Globally Fitted Decays of Sequence **2.**

Emission wavelength (nm)	A ₁	A ₂	A ₃	A ₄
380	0.894	0.097	0.006	0.003
390	0.866	0.123	0.007	0.004
400	0.857	0.13	0.008	0.005

Global Lifetimes: $\tau_1= 0.03$ ns, $\tau_2= 0.14$ ns, $\tau_3= 1.87$ ns and $\tau_4= 5.92$ ns

Table 5.6: Parameters Derived From the Globally Fitted Decays of Sequence **3**.

Emission wavelength (nm)	A ₁	A ₂	A ₃	A ₄
380	0.422	0.519	0.053	0.005
390	0.358	0.579	0.056	0.006
400	0.361	0.575	0.057	0.007

Global Lifetimes: $\tau_1=0.08$ ns, $\tau_2=0.31$ ns, $\tau_3=1.05$ ns, $\tau_4=5.55$ ns

Table 5.7: Parameters Derived From the Globally Fitted Decays of Sequence **4**.

Emission wavelength (nm)	A ₁	A ₂	A ₃	A ₄
380	0.686	0.302	0.009	0.003
390	0.662	0.325	0.01	0.004
400	0.682	0.303	0.011	0.005

Global Lifetimes: $\tau_1=0.06$ ns, $\tau_2=0.24$ ns, $\tau_3=1.08$ ns, $\tau_4=5.95$ ns

Table 5.8: Parameters derived from the globally fitted decays of sequence **4 rev**

Emission wavelength (nm)	A ₁	A ₂	A ₃	A ₄
380	0.683	0.301	0.009	0.003
390	0.655	0.322	0.01	0.004
400	0.691	0.308	0.011	0.005

Global Lifetimes: $\tau_1=0.04$, $\tau_2=0.13$, $\tau_3=1.66$, $\tau_4=4.93$

5.7 Results and Discussion

A. Quantum Yield

The quantum yields of the sequences are shown in Table 5.9. Note that **1 rev** is being used as the standard and hence the quantum yield is constant throughout the trials. Sequences in the context TUA (**1, 2, 4 rev**) in general, have lower quantum yields than the sequences in the context AUT (**3, 4, 1 rev**).

Table 5.9: Quantum Yield Results for DNA Sequences. “Seq” refers to sequence name.

Seq	Trial 1	Trial 2	Trial 3	Trial 4	Average ϕ
1 rev	0.01*	0.01	0.01	0.01	0.01*
1	0.0038	0.0037	0.0038	0.0036	0.0037
2	0.0030	0.0030	0.0029	0.0030	0.0030
3	0.0094	0.0095	0.0097	0.0095	0.0095
4	0.0059	0.0057	0.006	0.0059	0.0059
4 rev	0.0036	0.0034	0.0033	0.0035	0.0034

* 1 rev is being used as reference and hence, the ϕ of remains constant through trials.

B. Lifetime Analysis

The lifetime decay curve of all the sequences being studied, along with IRF is shown in figure 5.7. The data were analyzed as mentioned previously and observation of a multiexponential decay indicates that the emitting isolated 2-AP molecules exist in a

heterogeneous environment, with the different decay components representing populations of 2-AP molecules subject to different environments and stacking in the DNA context.

The fluorescence response of the DNA duplexes is dominated by the two short lifetime components, <100 ps and 100-500 ps, respectively, which typically accounts for 90% of the 2-AP species in the duplex. These two components can be comprehended as a highly stacked 2-AP population. Although four decay components were required to satisfactorily fit the decay data, the amplitudes of the two components with the longer lifetimes, ~1ns and > 4.5ns, are very small; together these represent less than 10% of the

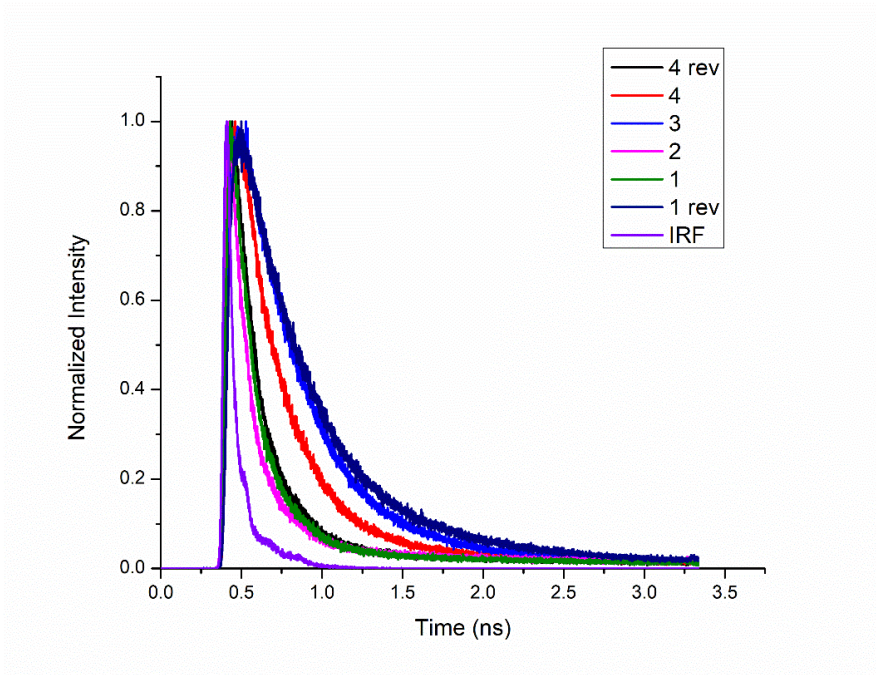


Figure 5.7: Lifetime Decay of Sequences Shown With IRF.

emitting 2-AP population in DNA. These >1 ns component can be interpreted as 2-AP relatively free to move and not completely stacked by the neighboring bases and hence, showing lifetimes tending to that of free 2-AP. However, even the longest lifetime

component is still ~50% shorter than the lifetime of free 2-AP in buffer solution (10.2 ns) pointing towards a certain extent of quenching possible in all populations.

Table 5.10: Lifetime Analysis of DNA Sequences. “Seq” refers to sequence name.

Seq	A ₁	A ₂	A ₃	A ₄	τ_1 (ns)	τ_2 (ns)	τ_3 (ns)	τ_4 (ns)	$\langle\tau\rangle$ (ns)
1 rev	0.402	0.495	0.097	0.006	0.07	0.31	1.00	6.09	0.32
1	0.709	0.278	0.009	0.004	0.03	0.12	1.46	5.83	0.09
2	0.873	0.116	0.007	0.004	0.03	0.14	1.87	5.92	0.08
3	0.381	0.557	0.056	0.006	0.08	0.31	1.05	5.55	0.29
4	0.593	0.375	0.025	0.006	0.06	0.24	1.08	5.95	0.19
4 rev	0.676	0.31	0.01	0.004	0.04	0.13	1.66	4.93	0.10

C. Ultrafast-Decaying Dark Species Population

It was observed that the ratio of the lifetime of free 2-AP (10.2 ns) and the average lifetime of sequences gave a higher value than the ratio of quantum yield of free 2-AP (0.68) and sequences as shown in table 5.11. This indicates that the lifetime of the sequence is underrepresented. This is consistent with the presence of an ultrafast decaying, quenched population of 2-AP which is decaying in picosecond range and hence, is not possible to be captured with the TCSPC instrumentation (<40 ps).

Thus, it's important to include the ultrafast-decaying dark species explicitly as an additional amplitude parameter α_0 given as²³⁴:

$$\alpha_0 = 1 - \left(\frac{\tau_{free}\phi_{DNA}}{\langle\tau\rangle_{DNA}\phi_{free}} \right) \quad (5.9)$$

where τ is lifetime, ϕ is quantum yield, subscript free refers to free 2-AP in buffer solution and DNA refers to the sequence. There are very few studies in the literature that takes into consideration this undetected population in the literature, which can lead to misinterpretation of the data.^{220,234} Calculated α_0 shown in table 5.11 goes on to show that majority of 2-AP in DNA duplex is extremely quenched due to stacking interactions with the neighboring bases.

Table 5.11: Calculated α_0 for DNA Sequences. “Seq” refers to sequence name.

Seq	ϕ_{DNA}	$\langle\tau\rangle_{DNA}(\text{ns})$	ϕ_{free}/ϕ_{DNA}	$\tau_{free}/\langle\tau\rangle_{DNA}$	α_0
1 rev	0.01	0.32	0.015	0.031	0.53
1	0.0037	0.09	0.005	0.010	0.40
2	0.0030	0.08	0.004	0.008	0.45
3	0.0095	0.29	0.014	0.029	0.51
4	0.0059	0.19	0.009	0.019	0.54
4 rev	0.0034	0.10	0.005	0.010	0.48

All the other amplitudes need to be adjusted to accommodate this ultrafast decaying component such that $\alpha_0 + \sum_{i=1}^n A_i = 1$. Thus, the amplitude values are corrected for the dark species, using $\alpha_i = A_i (1 - \alpha_0)$ and shown in table 5.12 which has the updated

population distribution. From the literature and observations in this study, α_0 represents a highly stacked environment in the sequence and hence, can be used as a measure of how rigid the DNA is in a given context; a more rigid context will give rise to a well-stacked, and hence, a highly quenched 2-AP population which can be quantified from a larger value of α_0 . Thus, this work attempts to quantify the rigidity of a DNA context in terms of α_0 .

Table 5.11: α_0 and Corrected Fractional Distribution of Lifetime Components. “Seq” refers to sequence name.

Seq	α_0^*	α_1	α_2	α_3	α_4	τ_1 (ns)	τ_2 (ns)	τ_3 (ns)	τ_4 (ns)	$\langle\tau\rangle$ (ns)
1 rev	0.530	0.190	0.235	0.046	0.003	0.07	0.31	1.00	6.09	0.32
1	0.400	0.424	0.166	0.006	0.002	0.03	0.12	1.46	5.83	0.09
2	0.450	0.476	0.0635	0.004	0.002	0.03	0.14	1.87	5.92	0.08
3	0.510	0.185	0.271	0.027	0.003	0.08	0.31	1.05	5.55	0.29
4	0.540	0.271	0.171	0.012	0.003	0.06	0.24	1.08	5.95	0.19
4 rev	0.480	0.349	0.160	0.005	0.002	0.04	0.13	1.66	4.93	0.10

*As α_0 is a calculated value with two significant figures and other fractional components acquired have three significant figures, a zero is added to α_0 for calculations and reporting of all amplitudes.

From table 5.12, the most rigid sequence based on α_0 is **4** and **1 rev** whereas, least rigid, therefore, the most flexible sequence is **1**. The rigidity ranking through **1** to **4** follows **1 < 2 < 3 < 4** according to their α_0 value and a visual representation of this trend is provided in figure 5.8. Between **1** and **1 rev**, **1 rev** is more rigid. On the contrary between **4** and **4 rev**, **4** gives a higher α_0 thus, more rigid. As mentioned in table 5.1, the only difference

between **1/4** and **1 rev/4 rev** is the flanking based are reversed. Hence, a different value of α_0 between these sequences points towards rigidity being a DNA directionality-dependent property. The biological implications of this will be discussed further.

D. UDG Uracil Removal Kinetics

As mentioned in the Chemicals and Sequences section, The sequences are based on a previous study where DNA repair in vitro by uracil-DNA glycosylase from *E. coli* was studied.²⁰¹ These uracil removal rates were determined for different uracil context in an *E. coli* *lacI* gene (>1000 nucleotides) and later the uracil efficiency for selected sequence contexts were checked on smaller 19-22-nucleotides long sequences, showing consistency. The paper uses electrophoresis-based assay and the % of uracil removed after incubation times is reported. As mentioned previously, we are using a 39-nucleotides long sequence and 2-AP fluorescence assay, making it crucial to check whether our assays show similar uracil removal efficiency trends. According to the paper uracil removal efficiency can be ranked as **1** (100% uracil removal) > **2** (50% uracil removal) > **3** (37% uracil removal) > **4** (12% uracil removal). The initial rate studies are ongoing for this work and being conducted by Bryan Ugaz. The initial results look in line with the paper and a couple of patterns can be seen readily such as **1** > **2** > **4**, **4 rev** > **4** and **1** > **1 rev** at the concentration of 0.15uM. The **1** > **4** trend was also confirmed by gel electrophoresis assay.

E. Ultrafast-Decaying Dark Species Correlation to Rigidity

The final goal of this work is to find the relationship between the physical properties of DNA and the sequence-dependent uracil removal efficiency. Our hypothesis is that a

more rigid uracil environment should make the flipping of the uracil base out of the sequence by UDG more difficult, thus decreasing the uracil removal efficiency.

Since the sequences are designed such that 2-AP is placed directly opposite to uracil, the environment in terms of local rigidity experienced by uracil should be equivalent to 2-AP. Therefore, based on discussion in the Ultrafast-Decaying Dark Species Population section, the uracil is present in the most rigid context in **4**. The rigidity ranking through **1** to **4** should follow $\mathbf{1} < \mathbf{2} < \mathbf{3} < \mathbf{4}$ according to their α_0 value as can be visually seen in figure 5.8.

If the hypothesis that the more rigid contexts make uracil flipping difficult, making rigid sequences bad substrate for uracil removal is true, the uracil removal should follow a trend where **4**, being most rigid, gives the lowest uracil removal rate. In contrast, **1**, being least rigid should make uracil flipping by UDG easier and hence, give the highest rate. The trend for uracil removal rate by UDG, by this logic, should be $\mathbf{4} < \mathbf{3} < \mathbf{2} < \mathbf{1}$, which is in line with observed rates discussed in the UDG Uracil Removal Kinetics section. Also, as **1** sequence gives the highest rate, it was expected that reversing the uracil flanking bases should lower the rate, which is observed. The reason for this decrease in rate can be attributed to **1 rev** being more rigid between **1** and **1 rev** based on α_0 .

Thus, we can use the α_0 as a measure of the rigidity of the DNA and correlate it with uracil removal efficiency by UDG, confirming that the preliminary results support our hypothesis.

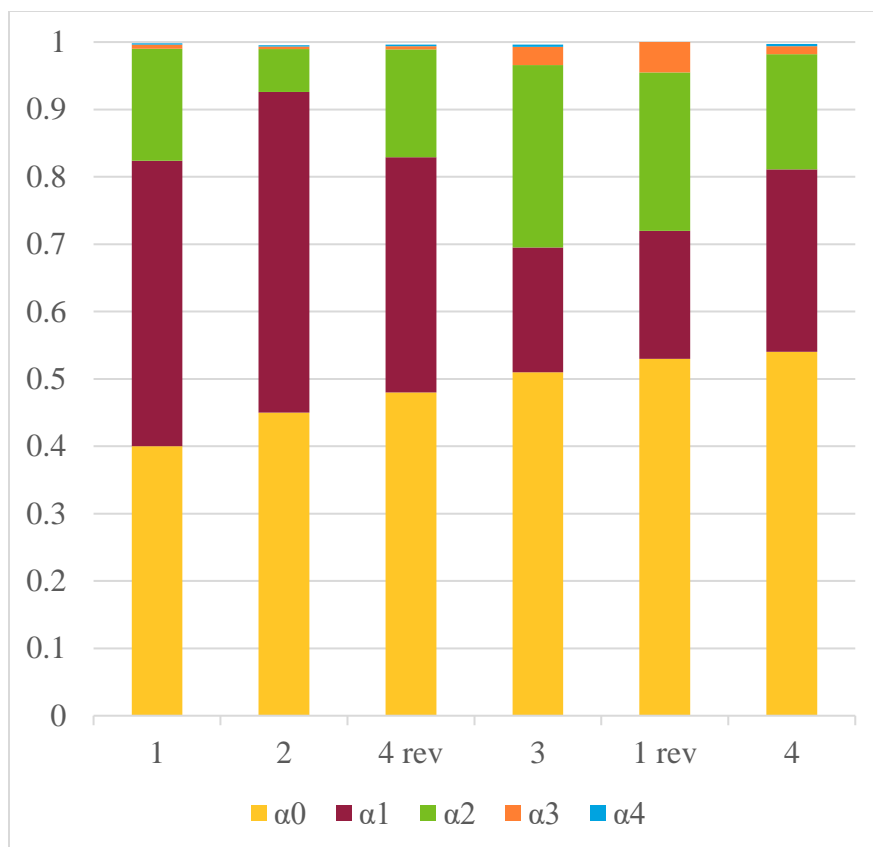


Figure 5.8: Stacked Column Plot of Calculated Amplitudes for Sequences.

5.8 Future Work

The next set of sequences to systematically understand the immediate context dependence are shown in table 5.13. Thus, the next goal is to study the uracil removal rate dependence on the sequence in a systematic way, changing one base at a time. These studies will shed light on the contribution of nature of the bases flanking uracil and directionality dependence (5' or 3') to the overall physical properties and uracil removal efficiency. As shown in table 5.13, sequences 1 A and 4 A are variants of 1 and 4 with both flanking bases changed to A. Similarly, 1 T and 4 T are variants of 1 and 4 with both flanking bases changed to T. This will also help answer the question of how much the

Table 5.13: Sequences to Be Studied Next. “Seq” refers to sequence name.

Seq	Sequence (5'-3')
1	CTA TAT TGG AAG CTT GCA T/ideoxyU/A ATG ACT CTG TAC ACG AAG CTT CGT GTA CAG AGT CAT T/i2AmPr/A TGC AAG CTT CCA ATA TAG
4	CTA GAA TGG AAG CTT GAA A/ideoxyU/T GTT ACT CTG TAC ACG AAG CTT CGT GTA CAG AGT AAC A/i2AmPr/T TTC AAG CTT CCA TTC TAG
1 A	CTA TGT TGG AAG CTT GCA A/ideoxyU/A ATG ACT CTG TAC ACG AAG CTT CGT GTA CAG AGT CAT T/i2AmPr/T TGC AAG CTT CCA ACA TAG
1 T	CTA TAT TGG AAG CTT GCA T/ideoxyU/T ATG ACT CTG TAC ACG AAG CTT CGT GTA CAG AGT CAT A/i2AmPr/A TGC AAG CTT CCA ATA TAG
4 A	CTA GAA TGG AAG CTT GAA A/ideoxyU/A GTT ACT CAG TAC ACG AAG CTT CGT GTA CTG AGT AAC T/i2AmPr/T TTC AAG CTT CCA TTC TAG
4 T	CTA GAA TGG AAG CTT GAA T/ideoxyU/T GTT ACT CTG TAC ACG AAG CTT CGT GTA CAG AGT AAC A/i2AmPr/A TTC AAG CTT CCA TTC TAG

sequence context which is immediately next to U matters in flexibility and uracil removal efficiency. Till now, this study has focused on sequences where U is surrounded by T and A bases and the reason is that as mentioned previously, 2-AP is quenched the most by G. However, a sequence containing G was studied, and even though, the fluorescence is heavily quenched ($\phi = 0.002$, $\langle\tau\rangle = 0.05$ ns), the data can still be resolved to get the four-component lifetime distributions with ultrafast-decaying dark species population being more prominent (~70%). Further sequences for making a broader study will be chosen

based on the results obtained for the new sequences in table 5.13 and computational assessment of different context flexibility done by collaborators.

In addition to the reconvolution method being used currently, other methods involving probabilistic approach of data fitting will be tried for lifetime studies in the future. A MATLAB program based on a recently published paper comparing the deterministic and probabilistic approaches to fit lifetime data will be used for performing a probabilistic approach of analyzing decay curves.²⁴⁷ These methods include maximum entropy method (MEM), smoothed exponential series method (SESM), and basis pursuit denoising (BPDN) analysis.

In an effort to elucidate the flexibility based uracil removal efficiency in DNA, fluorescence technique, nuclear magnetic resonance (NMR) measurement of nucleotide dynamics and molecular dynamics (MD) simulations will be combined to give a holistic picture of the physical basis of the sequence-dependence. NMR will be used to get the imino proton exchange rates which can be used to characterize the kinetics of intrinsic deformability of DNA. MD simulations will be used to quantify barriers for uracil flipping as a function of sequence and to characterize which physical flexibility parameter is most important.

The final goal of this work is to come up with a universal approach to answer why base flipping proteins efficiency is sequence dependent. There are many DNA repairing proteins which rely on base flipping to remove impurities with sequence-dependent efficiency. This approach will eventually be expanded on to these other DNA repairing proteins such as, Thymine-DNA glycosylase (TDG) and Alanine-glyoxylate transaminase

(AGT) to check the universality of the local flexibility dependence on DNA repair efficiency.

REFERENCES

1. Lakowicz, J. *Principles of Fluorescence Spectroscopy*. (Kluwer Academic/Plenum Publishers, 1999).
2. Kasha, M. Characterization of Electronic Transitions in Complex Molecules. *Discuss. Faraday Soc.* 14–19 (1950).
3. Turro, N. J., Ramamurthy, V. & Scaiano, J. C. *Modern molecular photochemistry of organic molecules*. (University Science Books, 2010).
4. Torimura, M. et al. Fluorescence-quenching phenomenon by photoinduced electron transfer between a fluorescent dye and a nucleotide base. *Anal. Sci.* 17, 155–160 (2001).
5. Heinlein, T., Knemeyer, J. P., Piestert, O. & Sauer, M. Photoinduced electron transfer between fluorescent dyes and guanosine residues in DNA-hairpins. *J. Phys. Chem. B* 107, 7957–7964 (2003).
6. Clegg, R. M. 1.24 Fluorescence and FRET: Theoretical Concepts 101. in *Comprehensive Biophysics* 592–617 (Elsevier, 2012).
7. Klostermeier, D. & Millar, D. P. Time-resolved fluorescence resonance energy transfer: A versatile tool for the analysis of nucleic acids. *Biopolymers* 61, 159–179 (2001).
8. Yip, W. T., Hu, D. H., Yu, J., Vanden Bout, D. A. & Barbara, P. F. Classifying the photophysical dynamics of single- and multiple-chromophoric molecules by single molecule spectroscopy. *J. Phys. Chem. A* 102, 7564–7575 (1998).
9. Hartmann, A., Krainer, G. & Schlierf, M. Different Fluorophore Labeling Strategies and Designs Affect Millisecond Kinetics of DNA Hairpins. *Molecules* 19, 13735–13754 (2014).
10. Sauer, M., Hofkens, J. & Enderlein, J. Fluorophores and Fluorescent Labels. in *Handbook of Fluorescence Spectroscopy and Imaging* (eds. Sauer, M., Hofkens, J. & Enderlein, J.) (2011). doi:10.1002/9783527633500.ch2.
11. Hillisch, A., Lorenz, M. & Diekmann, S. Recent advances in FRET: distance determination in protein-DNA complexes. *Curr. Opin. Struct. Biol.* 11, 201–207 (2001).
12. Betzig, E. et al. Imaging Intracellular Fluorescent Proteins at Nanometer Resolution. *Science* 313, 1642–1645 (2006).

13. Betzig, E. & Chichester, R. J. Single Molecules Observed by Near-Field Scanning Optical Microscopy. *Science* 262, 1422–1425 (1993).
14. Hell, S. W. & Wichmann, J. Breaking the diffraction resolution limit by stimulated emission: stimulated-emission-depletion fluorescence microscopy. *Opt Lett* 19, 780–782 (1994).
15. Hwang, H. & Myong, S. Protein induced fluorescence enhancement (PIFE) for probing protein–nucleic acid interactions. *Chem. Soc. Rev.* 43, 1221–1229 (2014).
16. Lerner, E., Ploetz, E., Hohlbein, J., Cordes, T. & Weiss, S. A Quantitative Theoretical Framework For Protein-Induced Fluorescence Enhancement–Förster-Type Resonance Energy Transfer (PIFE-FRET). *J. Phys. Chem. B* 120, 6401–6410 (2016).
17. Wilhelmsson, L. M. Fluorescent nucleic acid base analogues. *Q. Rev. Biophys.* 43, 159–183 (2010).
18. Jones, A. C. & Neely, R. K. 2-aminopurine as a fluorescent probe of DNA conformation and the DNA-enzyme interface. *Q. Rev. Biophys.* 48, 244–279 (2015).
19. Sandin, P. Fluorescent properties of DNA base analogue tC upon incorporation into DNA -- negligible influence of neighbouring bases on fluorescence quantum yield. *Nucleic Acids Res.* 33, 5019–5025 (2005).
20. Fischer, M. & Georges, J. Fluorescence quantum yield of rhodamine 6G in ethanol as a function of concentration using thermal lens spectrometry. *Chem. Phys. Lett.* 260, 115–118 (1996).
21. Arbeloa, F. L., Arbeloa, T. L., Estevez, M. J. T. & Arbeloa, I. L. Photophysics of Rhodamines - Molecular-Structure and Solvent Effects. *J. Phys. Chem.* 95, 2203–2208 (1991).
22. Vogelsang, J., Cordes, T., Forthmann, C., Steinhauer, C. & Tinnefeld, P. Controlling the fluorescence of ordinary oxazine dyes for single-molecule switching and superresolution microscopy. *Proc. Natl. Acad. Sci. U. S. A.* 106, 8107–8112 (2009).
23. Rulliere, C. Laser action and photoisomerization of 3,3'-diethyl oxadicyanone iodide (DODCI) - Influence of temperature and concentration. *Chem. Phys. Lett.* 43, 303–308 (1976).
24. Bilmes, G. M., Tocho, J. O. & Braslavsky, S. E. Photophysical processes of polymethine dyes. An absorption, emission, and optoacoustic study on 3, 3'-diethylthiadicyanone iodide. *J. Phys. Chem.* 93, 6696–6699 (1989).

25. Korppitommola, J. E. I., Hakkarainen, A., Hukka, T. & Subbi, J. An Isomerization Reaction of a Cyanine Dye in Normal-Alcohols - Microscopic Friction and an Excited-State Barrier Crossing. *J. Phys. Chem.* 95, 8482–8491 (1991).
26. Mishra, A., Behera, R. K., Behera, P. K., Mishra, B. K. & Behera, G. B. Cyanines during the 1990s: A Review. *Chem. Rev.* 100, 1973–2012 (2000).
27. Levitus, M. & Ranjit, S. Cyanine dyes in biophysical research: the photophysics of polymethine fluorescent dyes in biomolecular environments. *Q. Rev. Biophys.* 44, 123–151 (2011).
28. Chibisov, A. K., Zakharova, G. V. & Görner, H. Effects of substituents in the polymethine chain on the photoprocesses in indodicarbocyanine dyes. *J. Chem. Soc. Faraday Trans.* 92, 4917–4925 (1996).
29. Akesson, E., Sundstrom, V. & Gillbro, T. Solvent-Dependent Barrier Heights of Excited-State Photoisomerization Reactions. *Chem. Phys. Lett.* 121, 513–522 (1985).
30. Norman, D. G., Grainger, R. J., Uhrin, D. & Lilley, D. M. J. Location of cyanine-3 on double-stranded DNA: Importance for fluorescence resonance energy transfer studies. *Biochemistry* 39, 6317–6324 (2000).
31. Ouellet, J., Schorr, S., Iqbal, A., Wilson, T. J. & Lilley, D. M. Orientation of cyanine fluorophores terminally attached to DNA via long, flexible tethers. *Biophys. J.* 101, 1148–1154 (2011).
32. Sanborn, M. E., Connolly, B. K., Gurunathan, K. & Levitus, M. Fluorescence properties and photophysics of the sulfoindocyanine Cy3 linked covalently to DNA. *J. Phys. Chem. B* 111, 11064–11074 (2007).
33. Grabolle, M., Pauli, J., Brehm, R. & Resch-Genger, U. Structural control of dye–protein binding, aggregation and hydrophilicity in a series of asymmetric cyanines. *Dyes Pigments* 103, 118–126 (2014).
34. Chibisov, A. et al. Photorelaxation processes in covalently linked indodicarbocyanine and thiadicarbocyanine dyes. *J. Phys. Chem.* 99, 886–893 (1995).
35. Cooper, M. et al. Cy3B (TM): Improving the performance of cyanine dyes. *J. Fluoresc.* 14, 145–150 (2004).
36. Kuzmin, V. A. & Darmanyan, A. P. Study of Sterically Hindered Short-Lived Isomers of Polymethine Dyes by Laser Photolysis. *Chem. Phys. Lett.* 54, 159–163 (1978).
37. Klehs, K. et al. Increasing the Brightness of Cyanine Fluorophores for Single-Molecule and Superresolution Imaging. *ChemPhysChem* 15, 637–641 (2014).

38. Leisle, L. et al. Cellular encoding of Cy dyes for single-molecule imaging. *eLife* 5, e19088 (2016).
39. Patterson, G., Davidson, M., Manley, S. & Lippincott-Schwartz, J. Superresolution Imaging using Single-Molecule Localization. *Annu. Rev. Phys. Chem.* 61, 345–367 (2010).
40. Dempsey, G. T. et al. Photoswitching Mechanism of Cyanine Dyes. *J. Am. Chem. Soc.* 131, 18192–18193 (2009).
41. Wurth, C., Grabolle, M., Pauli, J., Spieles, M. & Resch-Genger, U. Relative and absolute determination of fluorescence quantum yields of transparent samples. *Nat. Protoc.* 8, 1535–1550 (2013).
42. Suzuki, K. et al. Reevaluation of absolute luminescence quantum yields of standard solutions using a spectrometer with an integrating sphere and a back-thinned CCD detector. *Phys. Chem. Chem. Phys.* 11, 9850–9860 (2009).
43. Levitus, M. Tutorial: measurement of fluorescence spectra and determination of relative fluorescence quantum yields of transparent samples. *Methods Appl. Fluoresc.* 8, 033001 (2020).
44. O'Connor, D., Phillips, D., Eds. *Time-Correlated Single-Photon Counting*. (1984).
45. Wahl, M. *Time-Correlated Single Photon Counting*. 14.
46. Spiriti, J., Binder, J. K., Levitus, M. & van der Vaart, A. Cy3-DNA Stacking Interactions Strongly Depend on the Identity of the Terminal Basepair. *Biophys. J.* 100, 1049–1057 (2011).
47. Hofmann, H. Understanding disordered and unfolded proteins using single-molecule FRET and polymer theory. *Methods Appl. Fluoresc.* 4 (2016).
48. Shroder, D. Y., Lippert, L. G. & Goldman, Y. E. Single molecule optical measurements of orientation and rotations of biological macromolecules. *Methods Appl. Fluoresc.* 4 (2016).
49. Borgia, A., Williams, P. M. & Clarke, J. Single-molecule studies of protein folding. *Annu Rev Biochem* 77, 101–125 (2008).
50. Li, G. W. & Xie, X. S. Central dogma at the single-molecule level in living cells. *Nature* 475, 308–315 (2011).
51. Marshall, R. A., Aitken, C. E., Dorywalska, M. & Puglisi, J. D. Translation at the single-molecule level. *Annu Rev Biochem* 77, 177–203 (2008).
52. Park, J. et al. PcrA Helicase Dismantles RecA Filaments by Reeling in DNA in Uniform Steps. *Cell* 142, 544–555 (2010).

53. Schuler, B. & Eaton, W. A. Protein folding studied by single-molecule FRET. *Curr Opin Struct Biol* 18, 16–26 (2008).
54. Weiss, S. Fluorescence spectroscopy of single biomolecules. *Science* 283, 1676–1683 (1999).
55. Peterman, E. J. G., Sosa, H. & Moerner, W. E. Single-molecule fluorescence spectroscopy and microscopy of biomolecular motors. *Annu Rev Phys Chem* 55, 79–96 (2004).
56. Roy, R., Hohng, S. & Ha, T. A practical guide to single-molecule FRET. *Nat. Methods* 5, 507–516 (2008).
57. Ha, T., Kozlov, A. G. & Lohman, T. M. Single-Molecule Views of Protein Movement on Single-Stranded DNA. *Annu Rev Biophys* 41, 295–319 (2012).
58. Mukhopadhyay, J. *et al.* Translocation of sigma(70) with RNA polymerase during transcription: Fluorescence resonance energy transfer assay for movement relative to DNA. *Cell* 106, 453–463 (2001).
59. Honda, M., Park, J., Pugh, R. A., Ha, T. & Spies, M. Single-Molecule Analysis Reveals Differential Effect of ssDNA-Binding Proteins on DNA Translocation by XPD Helicase. *Mol Cell* 35, 694–703 (2009).
60. Myong, S. *et al.* Cytosolic Viral Sensor RIG-I Is a 5'-Triphosphate-Dependent Translocase on Double-Stranded RNA. *Science* 323, 1070–1074 (2009).
61. Hwang, H., Kim, H. & Myong, S. Protein induced fluorescence enhancement as a single molecule assay with short distance sensitivity. *Proc. Natl. Acad. Sci. U.S.A* 108, 7414–7418 (2011).
62. Qiu, Y. *et al.* Srs2 prevents Rad51 filament formation by repetitive motion on DNA. *Nat Commun* 4, 2281 (2013).
63. Park, J. *et al.* PcrA Helicase Dismantles RecA Filaments by Reeling in DNA in Uniform Steps. *Cell* 142, 544–555 (2010).
64. Galletto, R. & Tomko, E. J. Translocation of *Saccharomyces cerevisiae* Pif1 helicase monomers on single-stranded DNA. *Nuc Acids Res* 41, 4613–4627 (2013).
65. Koenig, S. L. B., Liyanage, P. S., Sigel, R. K. O. & Rueda, D. Helicase-mediated changes in RNA structure at the single-molecule level. *RNA Biology* 10, 133–148 (2013).
66. Koh, H. R., Kidwell, M. A., Rangunathan, K., Doudna, J. A. & Myong, S. ATP-independent diffusion of double-stranded RNA binding proteins. *P Natl Acad Sci USA* 110, 151–156 (2013).

67. Marko, R. A. *et al.* Binding Kinetics and Affinities of Heterodimeric versus Homodimeric HIV-1 Reverse Transcriptase on DNA-DNA Substrates at the Single-Molecule Level. *J. Phys. Chem. B* 117, 4560–4567 (2013).
68. Maxwell, B. A. & Suo, Z. Single-molecule Investigation of Substrate Binding Kinetics and Protein Conformational Dynamics of a B-family Replicative DNA Polymerase. *J Biol Chem* 288, 11590–11600 (2013).
69. Vrtis, K. B., Markiewicz, R. P., Romano, L. J. & Rueda, D. Carcinogenic adducts induce distinct DNA polymerase binding orientations. *Nuc Acids Res* 41, 7843–7853 (2013).
70. Nguyen, B. *et al.* Diffusion of Human Replication Protein A along Single-Stranded DNA. *J Mol Biol* 426, 3246–3261 (2014).
71. Morten, M., Lopez, S., Steinmark, I., Rafferty, A. & Magennis, S. Stacking-induced fluorescence increase reveals allosteric interactions through DNA. *Nucleic Acids Res* 46, 11618–11626 (2018).
72. McNerney, C. *et al.* Bending and Wrapping of Upstream Promoter DNA on E. coli RNA Polymerase Facilitates Open Complex Formation in Transcription Initiation; A Fluorescence (FRET, PIFE) Study. *FASEB Journal* 32 (2018).
73. Gidi, Y., Gotte, M. & Cosa, G. Conformational Changes Spanning Angstroms to Nanometers via a Combined Protein-Induced Fluorescence Enhancement-Forster Resonance Energy Transfer Method. *J. Phys. Chem. B* 121, 2039–2048 (2017).
74. Song, D., Graham, T. G. & Loparo, J. A general approach to visualize protein binding and DNA conformation without protein labelling. *Nat Commun* 7, 10976 (2016).
75. Lerner, E., Ploetz, E., Hohlbein, J., Cordes, T. & Weiss, S. A Quantitative Theoretical Framework For Protein-Induced Fluorescence Enhancement-Forster-Type Resonance Energy Transfer (PIFE-FRET). *J. Phys. Chem. B* 120, 6401–6410 (2016).
76. Koh, H., Wang, X. & Myong, S. Visualizing repetitive diffusion activity of double-strand RNA binding proteins by single molecule fluorescence assays. *Methods* 105, 109–118 (2016).
77. Evelyn, P. *et al.* Förster resonance energy transfer and protein-induced fluorescence enhancement as synergetic multi-scale molecular rulers. *Sci Rep* 6 (2016).
78. Zhou, R., Zhang, J., Bochman, M., Zakian, V. & Ha, T. Periodic DNA patrolling underlies diverse functions of Pif1 on R-loops and G-rich DNA. *Elife* 3 (2014).

79. Levitus, M. & Ranjit, S. Cyanine dyes in biophysical research: the photophysics of polymethine fluorescent dyes in biomolecular environments. *Q Rev Biophys* 44, 123–151 (2011).
80. Mujumdar, R. B., Ernst, L. A., Mujumdar, S. R., Lewis, C. J. & Waggoner, A. S. Cyanine Dye Labeling Reagents - Sulfoindocyanine Succinimidyl Esters. *Bioconjugate Chem* 4, 105–111 (1993).
81. Hwang, H. & Myong, S. Protein induced fluorescence enhancement (PIFE) for probing protein-nucleic acid interactions. *Chem Soc Rev* 43, 1221–1229 (2014).
82. Aramendia, P. F., Negri, R. M. & Roman, E. S. Temperature dependence of fluorescence and photoisomerization in symmetric carbocyanines. Influence of medium viscosity and molecular structure. *J. Phys. Chem* 98, 3165–3173 (1994).
83. Waldeck, D. H. & Fleming, G. R. Influence of Viscosity and Temperature on Rotational Reorientation - Anisotropic Absorption Studies of 3,3'-Diethyloxadicarbocyanine Iodide. *J Phys Chem* 85, 2614–2617 (1981).
84. Sundstrom, V. & Gillbro, T. Viscosity-Dependent Isomerization Yields of Some Cyanine Dyes - a Picosecond Laser Spectroscopy Study. *J Phys Chem* 86, 1788–1794 (1982).
85. Akesson, E., Sundstrom, V. & Gillbro, T. Solvent-Dependent Barrier Heights of Excited-State Photoisomerization Reactions. *Chem Phys Lett* 121, 513–522 (1985).
86. Korppittomola, J. E. I., Hakkarainen, A., Hukka, T. & Subbi, J. An Isomerization Reaction of a Cyanine Dye in Normal-Alcohols - Microscopic Friction and an Excited-State Barrier Crossing. *J Phys Chem* 95, 8482–8491 (1991).
87. Chibisov, A. K., Zakharova, G. V. & Gorner, H. Effects of substituents in the polymethine chain on the photoprocesses in indodicarbocyanine dyes. *J. Chem. Soc., Faraday Trans* 92, 4917–4925 (1996).
88. Rullière, C. Laser action and photoisomerisation of 3, 3'-diethyl oxadicarbocyanine iodide (DODCI): influence of temperature and concentration. *Chem Phys Lett* 43, 303–308 (1976).
89. Sanborn, M. E., Connolly, B. K., Gurunathan, K. & Levitus, M. Fluorescence properties and photophysics of the sulfoindocyanine Cy3 linked covalently to DNA. *J. Phys. Chem. B* 111, 11064–11074 (2007).
90. Spiriti, J., Binder, J. K., Levitus, M. & Vaart, A. Cy3-DNA Stacking Interactions Strongly Depend on the Identity of the Terminal Basepair. *Biophys. J* 100, 1049–1057 (2011).

91. Harvey, B. J., Perez, C. & Levitus, M. DNA sequence-dependent enhancement of Cy3 fluorescence. *Photoch Photobio Sci* 8, 1105–1110 (2009).
92. Stennett, E. M., Ciuba, M. A., Lin, S. & Levitus, M. Demystifying PIFE: The photophysics behind the protein-induced fluorescence enhancement phenomenon in Cy3. *J. Phys. Chem. letters* 6, 1819–1823 (2015).
93. Gruber, H. J. *et al.* Anomalous fluorescence enhancement of Cy3 and Cy3.5 versus anomalous fluorescence loss of Cy5 and Cy7 upon covalent linking to IgG and noncovalent binding to avidin. *Bioconjugate Chem* 11, 696–704 (2000).
94. Czerney, P. *et al.* Tailor-made dyes for fluorescence correlation spectroscopy (FCS). *Biol Chem* 382, 495–498 (2001).
95. Buschmann, V., Weston, K. D. & Sauer, M. Spectroscopic study and evaluation of red-absorbing fluorescent dyes. *Bioconjugate Chem* 14, 195–204 (2003).
96. Klehs, K. *et al.* Increasing the Brightness of Cyanine Fluorophores for Single-Molecule and Superresolution Imaging. *ChemPhysChem* 15, 637–641 (2014).
97. Preus, S., Noer, S. L., Hildebrandt, L. L., Gudnason, D. & Birkedal, V. iSMS: single-molecule FRET microscopy software. *Nat Methods* 12, 593–594 (2015).
98. Bronson, J. E., Fei, J. Y., Hofman, J. M., Gonzalez, R. L. & Wiggins, C. H. Learning Rates and States from Biophysical Time Series: A Bayesian Approach to Model Selection and Single-Molecule FRET Data. *Biophys J* 97, 3196–3205 (2009).
99. Ponterini, G. & Momicchioli, F. Trans Cis Photoisomerization Mechanism of Carbocyanines - Experimental Check of Theoretical-Models. *Chem Phys* 151, 111–126 (1991).
100. Lee, S. F., Vérolet, Q. & Fürstenberg, A. Improved Super-Resolution Microscopy with Oxazine Fluorophores in Heavy Water. *Angew. Chem. Int. Ed* 52, 8948–8951 (2013).
101. Harvey, B. J. & Levitus, M. Nucleobase-Specific Enhancement of Cy3 Fluorescence. *J Fluoresc* 19, 443–448 (2009).
102. CRC handbook of chemistry and physics. (CRC Press/Taylor & Francis, 2018).
103. Harris, K. R. & Woolf, L. A. Temperature and volume dependence of the viscosity of water and heavy water at low temperatures. *J Chem Eng Data* 49, 1064–1069 (2004).
104. Yusa, M., Mathur, G. P. & Stager, R. A. Viscosity and Compression of Ethanol-Water Mixtures of Pressures up to 40000 Psig. *J Chem Eng Data* 22, 32–35 (1977).

105. Khimenko, V., Chibisov, A. K. & Görner, H. Effects of alkyl substituents in the polymethine chain on the photoprocesses in thiocarbocyanine dyes. *J. Phys. Chem. A* 101, 7304–7310 (1997).
106. Kuzmin, V. A. & Darmanyany, A. P. Study of Sterically Hindered Short-Lived Isomers of Polymethine Dyes by Laser Photolysis. *Chem Phys Lett* 54, 159–163 (1978).
107. Chibisov, A. et al. Photorelaxation processes in covalently linked indocarbocyanine and thiocarbocyanine dyes. *J. Phys. Chem* 99, 886–893 (1995).
108. Dempster, D., Morrow, T., Rankin, R. & Thompson, G. Photochemical characteristics of cyanine dyes. Part 1.—3, 3'-diethyloxadicarbocyanine iodide and 3, 3'-diethylthiadicarbocyanine iodide. *J. Chem. Soc. Faraday Trans. 2: Molecular and Chemical Physics* 68, 1479–1496 (1972).
109. Duchowicz, R., Scaffardi, L. & Tocho, J. O. Relaxation Processes of Singlet Excited-State of 3,3'-Diethyloxadicarbocyanine Iodide (DODCI) Photoisomer. *Chem Phys Lett* 170, 497–501 (1990).
110. Huang, Z. X. et al. Spectral identification of specific photophysics of Cy5 by means of ensemble and single molecule measurements. *J Phys Chem A* 110, 45–50 (2006).
111. Ciuba, M. A. & Levitus, M. Manganese-Induced Triplet Blinking and Photobleaching of Single Molecule Cyanine Dyes. *ChemPhysChem* 14, 3495–3502 (2013).
112. Jia, K. et al. Characterization of photoinduced isomerization and intersystem crossing of the cyanine dye Cy3. *J Phys Chem A* 111, 1593–1597 (2007).
113. Sigel, H. & Griesser, R. Nucleoside 5'-triphosphates: self-association, acid-base, and metal ion-binding properties in solution. *Chem Soc Rev* 34, 875–900 (2005).
114. Rymden, R. & Stilbs, P. Nucleotide Aggregation in Aqueous-Solution – a Multicomponent Self-Diffusion Study. *Biophys Chem* 21, 145–156 (1985).
115. Ranjit, S. & Levitus, M. Probing the Interaction Between Fluorophores and DNA Nucleotides by Fluorescence Correlation Spectroscopy and Fluorescence Quenching. *Photochem Photobiol* 88, 782–791 (2012).
116. Iqbal, A., Wang, L., Thompson, K. C., Lilley, D. M. J. & Norman, D. G. The structure of cyanine 5 terminally attached to double-stranded DNA: Implications for FRET studies. *Biochemistry* 47, 7857–7862 (2008).

117. Urnavicius, L., McPhee, S. A., Lilley, D. M. & Norman, D. G. The structure of sulfoindocarbocyanine 3 terminally attached to dsDNA via a long, flexible tether. *Biophys J* 102, 561–568 (2012).
118. Widengren, J. & Schwille, P. Characterization of photoinduced isomerization and back-isomerization of the cyanine dye Cy5 by fluorescence correlation spectroscopy. *J Phys Chem A* 104, 6416–6428 (2000).
119. Sims, P. J., Waggoner, A. S., Wang, C. H. & Hoffman, J. F. Studies on Mechanism by Which Cyanine Dyes Measure Membrane-Potential in Red Blood-Cells and Phosphatidylcholine Vesicles. *Biochemistry* 13, 3315–3330 (1974).
120. Dyomics. <https://dyomics.com/en/products/red-excitation/dy-630.html> (accessed May 9 2019).
121. Michie, M. S. et al. Cyanine Conformational Restraint in the Far-Red Range. *J Am Chem Soc* 139, 12406–12409 (2017).
122. Rurack, K. Fluorescence Quantum Yields: Methods of Determination and Standards. in *Standardization and Quality Assurance in Fluorescence Measurements I* (eds. Techniques, R.-G. & U.) 101–145 (Springer, 2008).
123. Sauer, M. & Heilemann, M. Single-Molecule Localization Microscopy in Eukaryotes. *Chem. Rev.* 117, 7478–7509 (2017).
124. Sengupta, P., van Engelenburg, S. B. & Lippincott-Schwartz, J. Superresolution Imaging of Biological Systems Using Photoactivated Localization Microscopy. *Chem. Rev.* 114, 3189–3202 (2014).
125. Huang, B., Bates, M. & Zhuang, X. Super-Resolution Fluorescence Microscopy. *Annu. Rev. Biochem.* 78, 993–1016 (2009).
126. Mortensen, K. I., Churchman, L. S., Spudich, J. A. & Flyvbjerg, H. Optimized localization analysis for single-molecule tracking and super-resolution microscopy. *Nat Methods* 7, 377–381 (2010).
127. Grimm, J. B. et al. A general method to improve fluorophores for live-cell and single-molecule microscopy. *Nat Methods* 12, 244–250 (2015).
128. Mishra, A., Behera, R. K., Behera, P. K., Mishra, B. K. & Behera, G. B. Cyanines during the 1990s: A Review. *Chem. Rev.* 100, 1973–2012 (2000).
129. Gorka, A. P. & Schnermann, M. J. Harnessing cyanine photooxidation: from slowing photobleaching to near-IR uncaging. *Current Opinion in Chemical Biology* 33, 117–125 (2016).

130. Mujumdar, R. B., Ernst, L. A., Mujumdar, S. R., Lewis, C. J. & Waggoner, A. S. Cyanine dye labeling reagents: Sulfoindocyanine succinimidyl esters. *Bioconjugate Chem.* 4, 105–111 (1993).
131. van de Linde, S. et al. Direct stochastic optical reconstruction microscopy with standard fluorescent probes. *Nat Protoc* 6, 991–1009 (2011).
132. Heilemann, M., van de Linde, S., Mukherjee, A. & Sauer, M. Super-Resolution Imaging with Small Organic Fluorophores. *Angew. Chem. Int. Ed.* 48, 6903–6908 (2009).
133. Dempsey, G. T., Vaughan, J. C., Chen, K. H., Bates, M. & Zhuang, X. Evaluation of fluorophores for optimal performance in localization-based super-resolution imaging. *Nat Methods* 8, 1027–1036 (2011).
134. Levitus, M. & Ranjit, S. Cyanine dyes in biophysical research: the photophysics of polymethine fluorescent dyes in biomolecular environments. *Quart. Rev. Biophys.* 44, 123–151 (2011).
135. Stennett, E. M. S., Ciuba, M. A. & Levitus, M. Photophysical processes in single molecule organic fluorescent probes. *Chem. Soc. Rev.* 43, 1057–1075 (2014).
136. Waggoner, A. S. 54). RIGIDIZED TRIMETHINE CYANINE DYES. 28 (2000).
137. Cooper, M. et al. Cy3BTM: Improving the Performance of Cyanine Dyes. *Journal of Fluorescence* 6 (2004).
138. Sanborn, M. E., Connolly, B. K., Gurunathan, K. & Levitus, M. Fluorescence Properties and Photophysics of the Sulfoindocyanine Cy3 Linked Covalently to DNA. *J. Phys. Chem. B* 111, 11064–11074 (2007).
139. Heilemann, M., Margeat, E., Kasper, R., Sauer, M. & Tinnefeld, P. Carbocyanine Dyes as Efficient Reversible Single-Molecule Optical Switch. *J. Am. Chem. Soc.* 127, 3801–3806 (2005).
140. Chatterjee, A. K., Choi, T.-L., Sanders, D. P. & Grubbs, R. H. A General Model for Selectivity in Olefin Cross Metathesis. *J. Am. Chem. Soc.* 125, 11360–11370 (2003).
141. Garber, S. B., Kingsbury, J. S., Gray, B. L. & Hoveyda, A. H. Efficient and Recyclable Monomeric and Dendritic Ru-Based Metathesis Catalysts. *J. Am. Chem. Soc.* 122, 8168–8179 (2000).
142. Niehörster, T. et al. Multi-target spectrally resolved fluorescence lifetime imaging microscopy. *Nat Methods* 13, 257–262 (2016).

143. Chozinski, T. J., Gagnon, L. A. & Vaughan, J. C. Twinkle, twinkle little star: Photoswitchable fluorophores for super-resolution imaging. *FEBS Letters* 588, 3603–3612 (2014).
144. Dempsey, G. T. et al. Photoswitching Mechanism of Cyanine Dyes. *J. Am. Chem. Soc.* 131, 18192–18193 (2009).
145. Vaughan, J. C., Dempsey, G. T., Sun, E. & Zhuang, X. Phosphine Quenching of Cyanine Dyes as a Versatile Tool for Fluorescence Microscopy. *J. Am. Chem. Soc.* 135, 1197–1200 (2013).
146. Vaughan, J. C., Jia, S. & Zhuang, X. Ultrabright photoactivatable fluorophores created by reductive caging. *Nat Methods* 9, 1181–1184 (2012).
147. Lehmann, M. et al. Multicolor Caged dSTORM Resolves the Ultrastructure of Synaptic Vesicles in the Brain. *Angew. Chem. Int. Ed.* 54, 13230–13235 (2015).
148. Kundu, K. et al. Hydrocyanines: A Class of Fluorescent Sensors That Can Image Reactive Oxygen Species in Cell Culture, Tissue, and In Vivo. *Angew. Chem. Int. Ed.* 48, 299–303 (2009).
149. Ram, S., Prabhat, P., Chao, J., Sally Ward, E. & Ober, R. J. High Accuracy 3D Quantum Dot Tracking with Multifocal Plane Microscopy for the Study of Fast Intracellular Dynamics in Live Cells. *Biophysical Journal* 95, 6025–6043 (2008).
150. Franke, C., Sauer, M. & van de Linde, S. Photometry unlocks 3D information from 2D localization microscopy data. *Nat Methods* 14, 41–44 (2017).
151. Initial antibody labeling studies with NHS-esters of 7 and 8 resulted in significant H-aggregate formation.
152. Altman, R. B. et al. Cyanine fluorophore derivatives with enhanced photostability. *Nat Methods* 9, 68–71 (2012).
153. Renikuntla, B. R., Rose, H. C., Eldo, J., Waggoner, A. S. & Armitage, B. A. Improved Photostability and Fluorescence Properties through Polyfluorination of a Cyanine Dye. *Org. Lett.* 6, 909–912 (2004).
154. Toutchkine, A., Nguyen, D.-V. & Hahn, K. M. Merocyanine Dyes with Improved Photostability. *Org. Lett.* 9, 2775–2777 (2007).
155. Goraka, A. P. & Schnermann, M. J. Harnessing cyanine photooxidation: from slowing photobleaching to near-IR uncaging. *Current Opinion in Chemical Biology* 33, 117–125 (2016).
156. Hilderbrand, S. A. & Weissleder, R. Near-infrared fluorescence: application to in vivo molecular imaging. *Curr. Opin. Chem. Biol* 14, 71–9 (2010).

157. Zhou, X., Lai, R., Beck, J. R., Li, H. & Stains, C. I. Nebraska Red: a phosphinate-based near-infrared fluorophore scaffold for chemical biology applications. *Chem. Commun* 52, 12290–12293 (2016).
158. Cosco, E. D. et al. Flavylium Polymethine Fluorophores for Near- and Shortwave Infrared Imaging. *Angew. Chem. Int. Ed* 56, 13126–13129 (2017).
159. Liu, J. et al. Sulfone-Rhodamines: A New Class of Near-Infrared Fluorescent Dyes for Bioimaging. *ACS Appl. Mater. Interfaces* 8, 22953–62 (2016).
160. Soper, S. A. & Mattingly, Q. L. Steady-State and Picosecond Laser Fluorescence Studies of Nonradiative Pathways in Tricarbocyanine Dyes - Implications to the Design of near-Ir Fluorochromes with High Fluorescence Efficiencies. *J. Amer. Chem. Soc* 116, 3744–3752 (1994).
161. Levitus, M. & Ranjit, S. Cyanine dyes in biophysical research: the photophysics of polymethine fluorescent dyes in biomolecular environments. *Q. Rev. Biophys* 44, 123–151 (2011).
162. Stennett, E. M. S., Ciuba, M. A. & Levitus, M. Photophysical processes in single molecule organic fluorescent probes. *Chem. Soc. Rev* 43, 1057–1075 (2014).
163. Mujumdar, R. B., Ernst, L. A., Mujumdar, S. R., Lewis, C. J. & Waggoner, A. S. Cyanine dye labeling reagents: sulfoindocyanine succinimidyl esters. *Bioconj. Chem* 4, 105–11 (1993).
164. Mujumdar, S. R., Mujumdar, R. B., Grant, C. M. & Waggoner, A. S. Cyanine-labeling reagents: Sulfoindocyanine succinimidyl esters. *Bioconj. Chem* 7, 356–362 (1996).
165. Sanchez-Galvez, A. et al. Ultrafast radiationless deactivation of organic dyes: evidence for a two-state two-mode pathway in polymethine cyanines. *J. Amer. Chem. Soc* 122, 2911–2924 (2000).
166. Cooper, M. et al. Cy3B (TM): Improving the performance of cyanine dyes. *J. Fluoresc* 14, 145–150 (2004).
167. Michie, M. S. et al. Cyanine Conformational Restraint in the Far-Red Range. *J. Am. Chem. Soc* 139, 12406–12409 (2017).
168. Chibisov, A. K., Zakharova, G. V. & Gorner, H. Effects of substituents in the polymethine chain on the photoprocesses in indodicarbocyanine dyes. *J. Chem. Soc. Faraday Trans* 92, 4917–4925 (1996).
169. Aramendia, P. F., Negri, R. M. & Sanroman, E. Temperature-Dependence of Fluorescence and Photoisomerization in Symmetrical Carbocyanines - Influence of Medium Viscosity and Molecular-Structure. *J. Phys. Chem* 98, 3165–3173 (1994).

170. Fouassier, J. P., Lougnot, D. J. & Faure, J. Transient Absorptions in a Polymethine Laser Dye. *Chem. Phys. Lett* 35, 189–194 (1975).
171. Adamson, B. D., Coughlan, N. J. A., Continetti, R. E. & Bieske, E. J. Changing the shape of molecular ions: photoisomerization action spectroscopy in the gas phase. *Phys. Chem. Chem. Phys* 15, 9540–9548 (2013).
172. Waggoner, A. S. & Mujumdar, R. B. Rigidized trimethine cyanine dyes.
173. Sanborn, M. E., Connolly, B. K., Gurunathan, K. & Levitus, M. Fluorescence Properties and Photophysics of the Sulfoindocyanine Cy3 Linked Covalently to DNA. *J. Phys. Chem. B* 111, 11064 (2007).
174. Fouassier, J. P., Lougnot, D. J. & Faure, J. Transient Lifetime Measurements in 1,1'-Diethyl-4,4'-Carbocyanine Iodide (Cryptocyanine, Dci) Using a Train of Picosecond Pulses. *Chem. Phys. Lett* 30, 448–450 (1975).
175. Buschmann, V., W., K. D. & S, M. Spectroscopic study and evaluation of red-absorbing fluorescent dyes. *Bioconj. Chem* 14, 195–204 (2003).
176. Widengren, J. & S, P. Characterization of photoinduced isomerization and back-isomerization of the cyanine dye Cy5 by fluorescence correlation spectroscopy. *J. Phys. Chem. A* 104, 6416–6428 (2000).
177. Korppitommola, J. E. I., Hakkarainen, A., Hukka, T. & Subbi, J. An Isomerization Reaction of a Cyanine Dye in Normal-Alcohols - Microscopic Friction and an Excited-State Barrier Crossing. *J. Phys. Chem* 95, 8482–8491 (1991).
178. Kumari, N., Ciuba, M. A. & Levitus, M. Photophysical properties of the hemicyanine Dy-630 and its potential as a single-molecule fluorescent probe for biophysical applications. *Methods Appl. Fluoresc* 8, 015004 (2019).
179. Sundstrom, V. & Gillbro, T. Viscosity-Dependent Isomerization Yields of Some Cyanine Dyes - a Picosecond Laser Spectroscopy Study. *J. Phys. Chem* 86, 1788–1794 (1982).
180. Klehs, K. et al. Increasing the brightness of cyanine fluorophores for single-molecule and superresolution imaging. *Chemphyschem* 15, 637–41 (2014).
181. Åkesson, E., Sundström, V. & Gillbro, T., Solvent-dependent barrier heights of excited-state photoisomerization reactions. *Chem. Phys. Lett* 121, 513–522 (1985).
182. Kohn, W. & Sham, L. J. S.-C. Self-Consistent Equations Including Exchange and Correlation Effects. *Phys. Rev* 140, 1133–1138 (1965).
183. Gross, E. K. U. & Kohn, W. Time-Dependent Density-Functional theory. *Adv. Quantum Chem* 21, 255–291 (1990).

184. Becke, A. D. Density-Functional Thermochemistry. III. The Role of Exact Exchange. *J. Chem. Phys.* 98, 5648–5652 (1993).
185. Stephens, P. J., Devlin, F. J., Chablowski, C. F. & Frisch, M. J. Ab Initio Calculation of Vibrational Absorption and Circular Dichroism Spectra Using Density Functional Force Fields. *J. Phys. Chem* 98, 11623–11627 (1994).
186. Hertwig, R. H. & Koch, W. On the Parameterization of the Local Correlation Functional. What is Becke-3-LYP? *Chem. Phys. Lett* 268, 345–351 (1997).
187. Ivanic, J. Direct Configuration Interaction and Multiconfigurational Self-Consistent-Field Method for Multiple Active Spaces with Variable Occupations. I. Method. *J. Chem. Phys* 119, 9634–9376 (2003).
188. Roskop, L. & Gordon, M. S. Quasi-Degenerate Second-Order Perturbation Theory for Occupation Restricted Multiple Active Space Self-Consistent-Field Reference Functions. *J. Chem. Phys* 135, 044101 (2011).
189. Miertus, S., Scrocco, E. & Tomasi, J. Electrostatic Interaction of a Solute with a Continuum. A direct utilization of Ab Initio Molecular Potentials for the Prevision of Solvent Effects. *J. Chem. Phys* 55, 117–129 (1981).
190. Li, H. & Jensen, J. H. Improving the Efficiency and Convergence of Geometry Optimization with the Polarizable Continuum Model: New Energy Gradients and Molecular Surface Tessellation. *J. Comput. Chem* 25, 1449–1462 (2004).
191. Wang, Y. & Li, H. Excited State Geometry of Photoactive Yellow Protein Chromophore: A Combined Conductorlike Polarizable Continuum Model and Time-Dependent Density Functional Study. *J. Chem. Phys* 133, 034108 (2010).
192. Schmidt, M. W. et al. The General Atomic and Molecular Electronic Structure System. *J. Comput. Chem* 14, 1347–1363 (1993). See <http://www.msg.ameslab.gov/advances/updatepaper.html> for a current list of features.
193. Gordon, M. S. & Schmidt, M. W. Advances in electronic structure theory: GAMESS a decade later. in *Theory and Applications of Computational Chemistry: the first forty years* (eds. Dykstra, C. E., Frenking, G., Kim, K. S. & Scuseria, G. E.) (Amsterdam, 2005).
194. Champagne, B., Guillaume, M. & Zutterman, F. TDDFT investigation of the optical properties of cyanine dyes. *Chemical Physics Letters* 425, 105 (2006).
195. Le Guennic, B. & Jacquemin, D. Taking up the cyanine challenge with quantum tools. *Acc Chem Res* 48, 530 (2015).

196. Nani, R. R. et al. In Vivo Activation of Duocarmycin-Antibody Conjugates by Near-Infrared Light. vol. 3 (Acs Central Sci, 2017).
197. Szent-Gyorgyi, C. et al. Fluorogen-activating single-chain antibodies for imaging cell surface proteins. *Nat. Biotechnol* 26, 235 (2008).
198. Smith, B. D., Gassensmith, J. J. & Arunkumar, E., Molecular Encapsulation: Reactions in Constrained Systems 11, 309–325 (2010).
199. Visnes, T. et al. Uracil in DNA and its processing by different DNA glycosylases. *Philos. Trans. R. Soc. B-Biol. Sci.* 364, 563–568 (2009).
200. Slupphaug, G., Arvait, A., Krokan, H. E. & Tainer, J. A. A nucleotide-flipping mechanism from the structure of human uracil-DNA glycosylase bound to DNA. *Science* 272, 384–386 (1996).
201. Nilsen, H., Yazdankhah, S. P., Eftedal, I. & Krokan, H. E. Sequence specificity for removal of uracil from U·A pairs and U·G mismatches by uracil-DNA glycosylase from *Escherichia coli*, and correlation with mutational hotspots. *FEBS Lett.* 362, 205–209 (1995).
202. Hölz, K., Pavlic, A., Lietard, J. & Somoza, M. M. Specificity and Efficiency of the Uracil DNA Glycosylase-Mediated Strand Cleavage Surveyed on Large Sequence Libraries. *Sci. Rep.* 9, 17822 (2019).
203. Sibghat-Ullah et al. Base Analog and Neighboring Base Effects on Substrate Specificity of Recombinant Human G:T Mismatch-Specific Thymine DNA–Glycosylase †. *Biochemistry* 35, 12926–12932 (1996).
204. Eftedal, I., Guddal, P. H., Slupphaug, G., Volden, G. & Krokan, H. E. Consensus Sequences for Good and Poor Removal of Uracil from Double-Stranded DNA by Uracil-DNA Glycosylase. *Nucleic Acids Res.* 21, 2095–2101 (1993).
205. Xiao, G. Y. et al. Crystal structure of *Escherichia coli* uracil DNA glycosylase and its complexes with uracil and glycerol: Structure and glycosylase mechanism revisited. *Proteins-Struct. Funct. Genet.* 35, 13–24 (1999).
206. Bellamy, S. R. W., Krusong, K. & Baldwin, G. S. A rapid reaction analysis of uracil DNA glycosylase indicates an active mechanism of base flipping. *Nucleic Acids Res.* 35, 1478–1487 (2007).
207. Parikh, S. S., Putnam, C. D. & Tainer, J. A. Lessons learned from structural results on uracil-DNA glycosylase. *Mutat. Res. Repair* 460, 183–199 (2000).
208. Parikh, S. S. et al. Base excision repair initiation revealed by crystal structures and binding kinetics of human uracil-DNA glycosylase with DNA. *Embo J.* 17, 5214–5226 (1998).

209. Drohat, A. C. & Maiti, A. Mechanisms for enzymatic cleavage of the N-glycosidic bond in DNA. *Org. Biomol. Chem.* 12, 8367–8378 (2014).
210. Friedman, R. A. & Honig, B. A free energy analysis of nucleic acid base stacking in aqueous solution. *Biophys. J.* 69, 1528–1535 (1995).
211. Fuxreiter, M., Luo, N., Jedlovsky, P., Simon, I. & Osman, R. Role of base flipping in specific recognition of damaged DNA by repair enzymes. *J. Mol. Biol.* 323, 823–834 (2002).
212. Ramstein, J. & Lavery, R. Energetic Coupling between DNA Bending and Base Pair Opening. *Proc. Natl. Acad. Sci. U. S. A.* 85, 7231–7235 (1988).
213. Seibert, E., Ross, J. B. A. & Osman, R. Role of DNA flexibility in sequence-dependent activity of uracil DNA glycosylase. *Biochemistry* 41, 10976–10984 (2002).
214. Ward, D. C., Reich, E. & Stryer, L. Fluorescence Studies of Nucleotides and Polynucleotides. I. Formycin 2-Aminopurine Riboside 2,6-Diaminopurine Riboside and Their Derivatives. *J. Biol. Chem.* 244, 1228- (1969).
215. Serrano-Andres, L., Merchán, M. & Borin, A. C. Adenine and 2-aminopurine: Paradigms of modern theoretical photochemistry. *Proc. Natl. Acad. Sci.* 103, 8691–8696 (2006).
216. Ludwig, V. et al. 2-Aminopurine non-radiative decay and emission in aqueous solution: A theoretical study. *Chem. Phys. Lett.* 463, 201–205 (2008).
217. Feng, K., Engler, G., Seefeld, K. & Kleinermanns, K. Dispersed Fluorescence and Delayed Ionization of Jet-Cooled 2-Aminopurine: Relaxation to a Dark State Causes Weak Fluorescence. *ChemPhysChem* 10, 886–889 (2009).
218. Lobsiger, S., Sinha, R. K., Trachsel, M. & Leutwyler, S. Low-lying excited states and nonradiative processes of the adenine analogues 7H- and 9H-2-aminopurine. *J. Chem. Phys.* 134, 114307 (2011).
219. Reichardt, C., Wen, C., Vogt, R. A. & Crespo-Hernández, C. E. Role of intersystem crossing in the fluorescence quenching of 2-aminopurine 2'-deoxyriboside in solution. *Photochem. Photobiol. Sci. Off. J. Eur. Photochem. Assoc. Eur. Soc. Photobiol.* 12, 1341–1350 (2013).
220. Avilov, S. V., Piemont, E., Shvadchak, V., de Rocquigny, H. & Mely, Y. Probing dynamics of HIV-1 nucleocapsid protein/target hexanucleotide complexes by 2-aminopurine. *Nucleic Acids Res.* 36, 885–896 (2007).

221. Avilov, S. V., Godet, J., Piémont, E. & Mély, Y. Site-Specific Characterization of HIV-1 Nucleocapsid Protein Binding to Oligonucleotides with Two Binding Sites †. *Biochemistry* 48, 2422–2430 (2009).
222. Guest, C. R. et al. Interaction of DNA with the Klenow fragment of DNA polymerase I studied by time-resolved fluorescence spectroscopy. *Biochemistry* 30, 8759–8770 (1991).
223. Hochstrasser, R. A., Carver, T. E., Sowers, L. C. & Millar, D. P. Melting of a DNA helix terminus within the active site of a DNA polymerase. *Biochemistry* 33, 11971–11979 (1994).
224. Neely, R. K. Time-resolved fluorescence of 2-aminopurine as a probe of base flipping in M.HhaI-DNA complexes. *Nucleic Acids Res.* 33, 6953–6960 (2005).
225. Neely, R. K. & Jones, A. C. Influence of Base Dynamics on the Conformational Properties of DNA: Observation of Static Conformational States in Rigid Duplexes at 77 K. *J. Am. Chem. Soc.* 128, 15952–15953 (2006).
226. Nordlund, T. M. et al. Structure and dynamics of a fluorescent DNA oligomer containing the EcoRI recognition sequence: fluorescence, molecular dynamics, and NMR studies. *Biochemistry* 28, 9095–9103 (1989).
227. Rachofsky, E. L., Osman, R. & Ross, J. B. A. Probing structure and dynamics of DNA with 2-aminopurine: Effects of local environment on fluorescence. *Biochemistry* 40, 946–956 (2001).
228. Ramreddy, T., Rao & Krishnamoorthy, G. Site-Specific Dynamics of Strands in ss- and dsDNA As Revealed by Time-Domain Fluorescence of 2-Aminopurine. *J. Phys. Chem. B* 111, 5757–5766 (2007).
229. Sabir, T. et al. Branchpoint Expansion in a Fully Complementary Three-Way DNA Junction. *J. Am. Chem. Soc.* 134, 6280–6285 (2012).
230. Xu, D., Evans, K. O. & Nordlund, T. M. Melting and Premelting Transitions of an Oligomer Measured by DNA Base Fluorescence and Absorption. *Biochemistry* 33, 9592–9599 (1994).
231. Allan, B. W. & Reich, N. O. Targeted Base Stacking Disruption by the EcoRI DNA Methyltransferase. *Biochemistry* 35, 14757–14762 (1996).
232. Holz, B., Klimasauskas, S., Serva, S. & Weinhold, E. 2-Aminopurine as a fluorescent probe for DNA base flipping by methyltransferases. *Nucleic Acids Res.* 26, 1076–1083 (1998).
233. Gowher, H. & Jeltsch, A. Molecular enzymology of the Eco RV DNA-(adenine-N6)-methyltransferase: kinetics of DNA binding and bending, kinetic mechanism

- and linear diffusion of the enzyme on DNA11 Edited by J. Karn. *J. Mol. Biol.* 303, 93–110 (2000).
234. Godet, J. et al. Specific implications of the HIV-1 nucleocapsid zinc fingers in the annealing of the primer binding site complementary sequences during the obligatory plus strand transfer. *Nucleic Acids Res.* 39, 6633–6645 (2011).
235. Lenz, T. et al. 2-Aminopurine Flipped into the Active Site of the Adenine-Specific DNA Methyltransferase M.TaqI: Crystal Structures and Time-Resolved Fluorescence. *J. Am. Chem. Soc.* 129, 6240–6248 (2007).
236. O’Neil, M. A. & Barton, J. K. 2-Aminopurine: A Probe of Structural Dynamics and Charge Transfer in DNA and DNA:RNA Hybrids. *J. Am. Chem. Soc.* 124, 13053–13066 (2002).
237. O’Neill, M. A. & Barton, J. K. Effects of strand and directional asymmetry on base-base coupling and charge transfer in double-helical DNA. *Proc. Natl. Acad. Sci.* 99, 16543–16550 (2002).
238. O’Neil, M. A. & Barton, J. K. DNA Charge Transport: Conformationally Gated Hopping through Stacked Domains. *J. Am. Chem. Soc.* 126, 11471–11483 (2004).
239. O’Neill, M. A., Dohno, C. & Barton, J. K. Direct Chemical Evidence for Charge Transfer between Photoexcited 2-Aminopurine and Guanine in Duplex DNA. *J. Am. Chem. Soc.* 126, 1316–1317 (2004).
240. Larsen, O. F. A. et al. Ultrafast transient-absorption and steady-state fluorescence measurements on 2-aminopurine substituted dinucleotides and 2-aminopurine substituted DNA duplexes. *Phys. Chem. Chem. Phys.* 6, 154 (2004).
241. Neely, R. K. et al. Time-resolved fluorescence studies of nucleotide flipping by restriction enzymes. *Nucleic Acids Res.* 37, 6859–6870 (2009).
242. Xia, T. Taking femtosecond snapshots of RNA conformational dynamics and complexity. *Curr. Opin. Chem. Biol.* 12, 604–611 (2008).
243. Gelot, T., Tourón-Touceda, P., Crégut, O., Léonard, J. & Haacke, S. Ultrafast Site-Specific Fluorescence Quenching of 2-Aminopurine in a DNA Hairpin Studied by Femtosecond Down-Conversion. <https://pubs.acs.org/doi/pdf/10.1021/jp212187m> (2012) doi:10.1021/jp212187m.
244. Rachofsky, E. L., Seibert, E., Stivers, J. T., Osman, R. & Ross, J. B. A. Conformation and Dynamics of Abasic Sites in DNA Investigated by Time-Resolved Fluorescence of 2-Aminopurine †. *Biochemistry* 40, 957–967 (2001).
245. Bharill, S. et al. Fluorescence intensity decays of 2-aminopurine solutions: Lifetime distribution approach. *Anal. Biochem.* 377, 141–149 (2008).

246. Fogarty, A. C., Jones, A. C. & Camp, P. J. Extraction of lifetime distributions from fluorescence decays with application to DNA-base analogues. *Phys. Chem. Chem. Phys.* 13, 3819 (2011).
247. Smith, D. A., McKenzie, G., Jones, A. C. & Smith, T. A. Analysis of time-correlated single photon counting data: a comparative evaluation of deterministic and probabilistic approaches. *Methods Appl. Fluoresc.* 5, 042001 (2017).
248. Verbeek, G. et al. Gaussian distributions of the decay times of the singlet excited state of aromatic amines dispersed in polymer films. *Macromolecules* 26, 472–478 (1993).
249. Remington, J. M., Philip, A. M., Hariharan, M. & Kohler, B. On the origin of multiexponential fluorescence decays from 2-aminopurine-labeled dinucleotides. *J. Chem. Phys.* 145, 155101 (2016).
250. Sholokh, M. et al. Conquering 2-Aminopurine's Deficiencies: Highly Emissive Isomorphic Guanosine Surrogate Faithfully Monitors Guanosine Conformation and Dynamics in DNA. *J. Am. Chem. Soc.* 137, 3185–3188 (2015).

APPENDIX A

SUPPLEMENTAL INFORMATION FOR CHAPTER 2

Photophysical Properties of the Hemicyanine Dy-630 and its Potential as a Single-Molecule Fluorescent Probe for Biophysical Applications

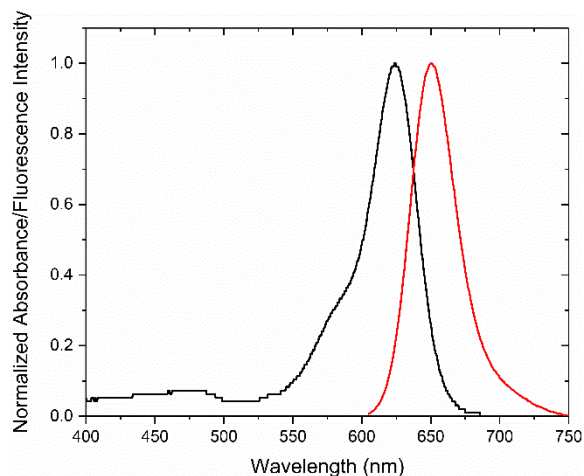
Nikita Kumari, Monika A. Ciuba, and Marcia Levitus.

School of Molecular Sciences and the Biodesign Institute, Arizona State University, PO Box 875601, Tempe, AZ 85287

Table of Contents

Figure A1: Absorption and Fluorescence Spectra of dIC ₂ (5) and Dy-630 in ethanol	158
Figure A2: Fluorescence anisotropy of Dy-630 in glycerol at 7°C	159
Figure A3: Aggregation of Dy-630 in water	160
Figure A4: Fitting parameters obtained from the time-resolved fluorescence decays of Dy-630 in solutions of dGMP	161
Figure A5: Time-resolved fluorescence anisotropy decays of Dy-630 in the presence and absence of Klenow Fragment (KF)	162
Figure A6: Biochemical activity of KF on the fluorescently labeled DNA samples.	162
Table A1: Fitting parameters obtained from the time-resolved fluorescence decays of all dye-DNA samples in the absence or presence of 1.25 equivalents of Klenow fragment.	163
Figure A7: sm-TIRF traces of Cy5-DNA compared to Dy-632-DNA	164
Analysis of Dwell Times	165

Dy-630



dIC₂(5)

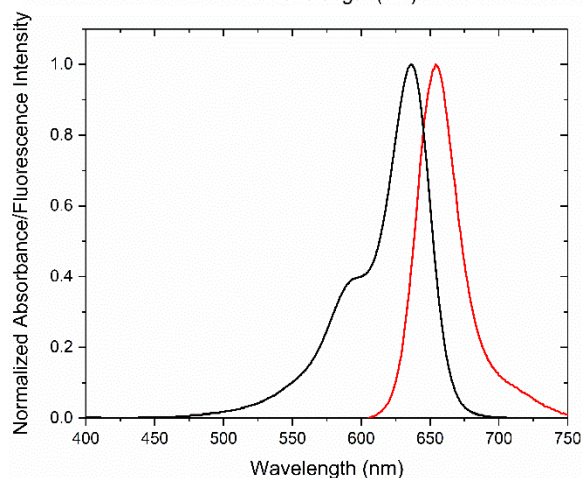


Figure A1: Normalized absorption (black) and fluorescence (red) spectra of Dy-630 (left) and dIC₂(5) in ethanol.

The value at the main absorption band is very close to the theoretical limit of 0.4 for absorption transition dipole moments that are parallel to the emission transition dipole moment. This indicates that the rotational correlation time of the dye in this solution is significantly longer than the lifetime of fluorescence, and that depolarization due to rotational diffusion is minimal. Therefore, the value measured at 470 nm is also a good estimate of the fundamental fluorescence anisotropy (r_0) at that wavelength.

The fundamental anisotropy is given by $r_0 = \frac{1}{5}(3\cos^2\beta - 1)$, where β is the angle between the absorption and emission transition dipole moments. A value of $r_0 = -0.1$ corresponds to $\beta = 66^\circ$.

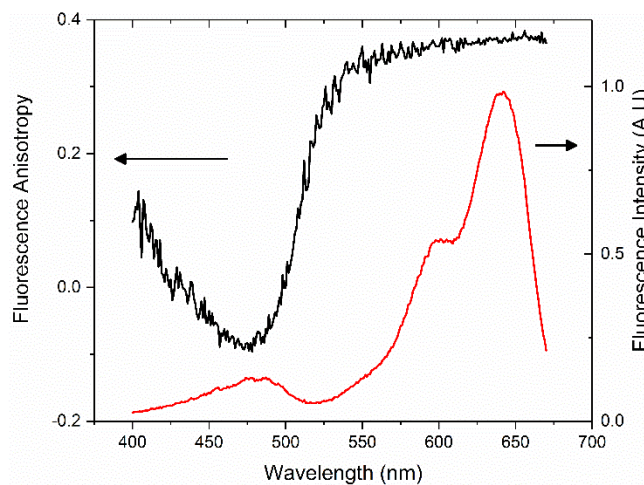


Figure A2: Steady-state fluorescence anisotropy of Dy-630 in glycerol at 7°C as a function of excitation wavelength. The normalized excitation spectrum of the same sample is shown in red.

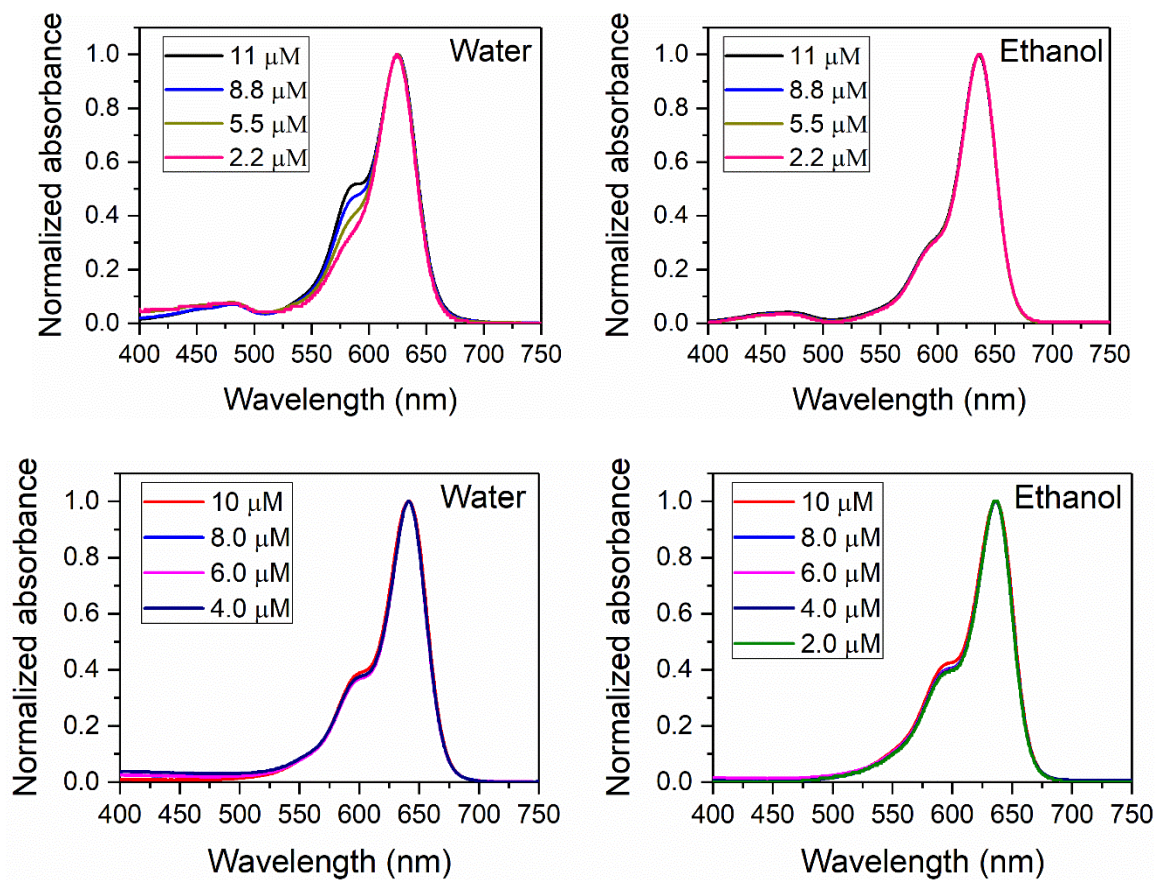


Figure A3: Normalized absorption spectra of Dy-630 (top) and diIC₂(5) (bottom) in water and ethanol at the dye concentrations indicated in the figure legend.

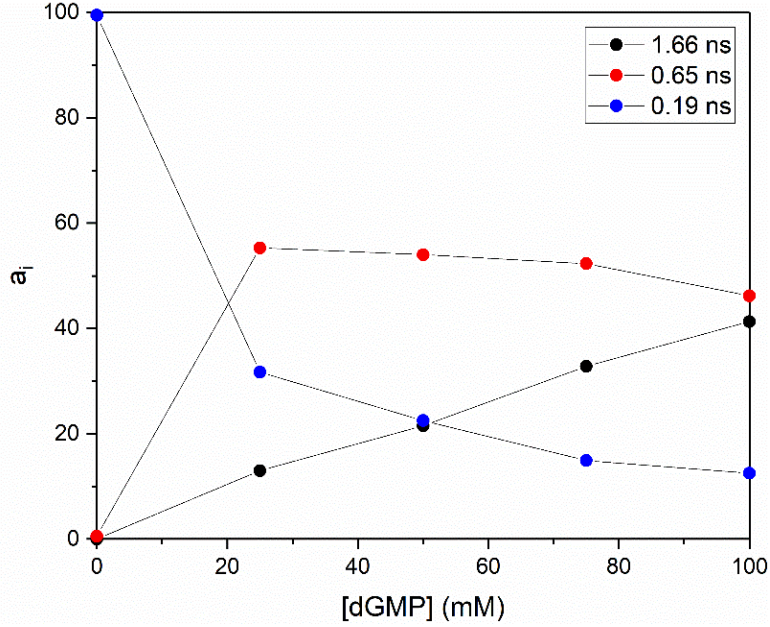


Figure A4: Time-resolved fluorescence decays of Dy-630 in solutions of dGMP. The figure shows the relative normalized amplitudes ($\sum_i a_i = 1$) for the three fluorescence lifetimes obtained from a global fit of the time resolved fluorescence decays measured at different dGMP concentrations. Data points are connected by lines just to guide the eye.

Fluorescence intensity decays were measured as described in Materials and Methods. The fluorescence anisotropy decays were constructed from the intensities collected at 0° (I_{VV}) and 90° (I_{VH}) as

$$r(t) = \frac{I_{VV}(t) - G \times I_{VH}(t)}{I_{VV}(t) + 2 \times G \times I_{VH}(t)}$$

The factor G accounts for polarization biases and was determined using the tail-matching method using a solution of Cy5 in aqueous buffer.

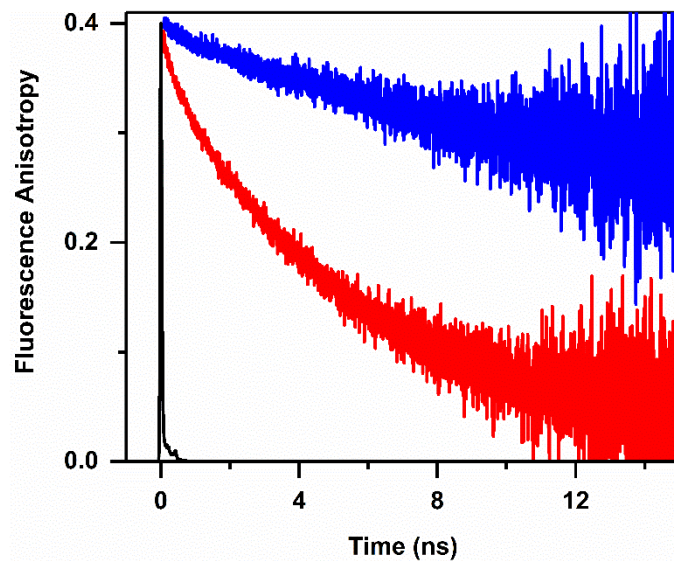
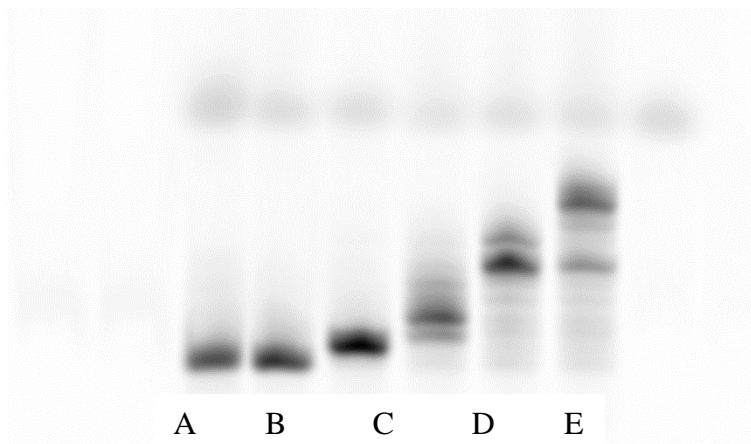


Figure A5: Time-resolved fluorescence anisotropy decays of Dy-630 in the presence and absence of Klenow Fragment (KF)



A: Dy-630 ssDNA, B: Dy-630 dsDNA, C: Dy-630 dsDNA + KF + dCTP, D: Dy-630 dsDNA + KF + dCTP + dATP, E: Dy-630 dsDNA + KF + dCTP + dATP + dGTP, F: Dy-630 dsDNA + KF + dCTP + dATP + dGTP + dTTP

Figure A6: Biochemical activity of KF on the fluorescently labeled DNA samples. Samples of Dy630-dsDNA were incubated with KF (DNA Pol I, Large Klenow fragment 3'→5' exo⁻, New England Biolabs) for 30 min. at 37°C in the absence or presence of dNTPs. Mixtures were run through 20% PAGE denaturing gels and imaged using a fluorescence scanner. Results show that KF is able to extend the fluorescently labeled DNA, indicating that its activity is not hampered by the dye.

Table A1: Time-resolved fluorescence intensity decay parameters of all dye-DNA samples in the absence or presence of 1.25 equivalents of Klenow fragment. Intensity decays were fitted with the minimum number of exponential terms that result in random residuals (see Materials and Methods).

	τ_1 (ns)	A_1 (%)	τ_2 (ns)	A_2 (%)	τ_3 (ns)	A_3 (%)	$\langle \tau \rangle$ (ns)
Dy-630-DNA	-	-	1.3	27%	3.0	73%	2.5
Dy-630-DNA + KF	-	-	1.5	23%	3.2	77%	2.8
Dy-632-DNA	-	-	1.1	32%	2.6	68%	2.1
Dy-632-DNA + KF	-	-	1.2	8%	2.9	92%	2.8
Cy3-DNA	0.2	37%	1.0	41%	2.1	22%	0.9
Cy3-DNA + KF	0.2	22%	1.1	42%	2.3	36%	1.3
Cy5-DNA	-	-	1.0	42%	2.0	58%	1.5
Cy5-DNA + KF	-	-	1.1	29%	2.3	71%	2.0

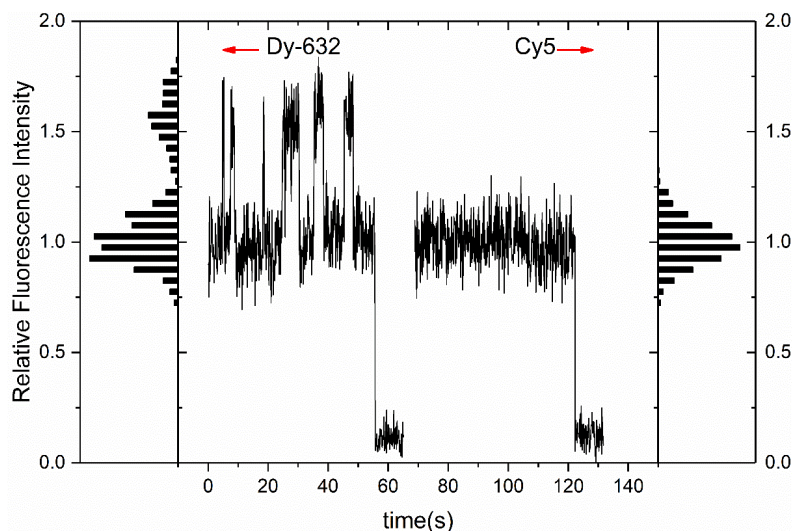


Figure A7: Comparison of sm-TIRF traces of Cy5-DNA and Dy-632-DNA. Both traces were normalized to allow for a direct comparison, and are shifted in time arbitrarily. Histograms of the normalized intensity values are shown on each side (intensities after photobleaching are not included). The width of the histograms for both dyes is similar, ruling out the possibility that Cy5 shows the same two-step behavior of Dy-632 but on a timescale that is too fast to result in distinct $H \leftrightarrow L$ transitions. This would result in significantly wider histograms for Cy5. Instead, these data suggest that either Cy5 mostly experiences one type of environment on the DNA, or that the fluorescence quantum yields on different environments are very similar.

Analysis of Dwell Times

The measured dwell times are discrete approximations of a continuous random variable (τ).

The values plotted in the ordinate of Fig. 2.9 represent the fraction of observed dwell times with $t_1 < \tau < t_2$. For example, in Fig. 2.9, the first bar indicates that we observed 104 dwell times out of a total of 203 with a duration shorter than 4 s ($0 < \tau < 4$ s).

Mathematically,

$$p(t_1 < \tau < t_2) = \int_{t_1}^{t_2} \langle \tau \rangle e^{-\tau/\langle \tau \rangle} d\tau = e^{-t_1/\langle \tau \rangle} - e^{-t_2/\langle \tau \rangle} \quad (2.3)$$

The values in the abscissa of Fig. 9 are the centers of the bins used to construct the histogram (t): $t = \frac{t_2+t_1}{2}$

It follows that $t_1 = t - (t_2 - t_1)/2$ and $t_2 = t + (t_2 - t_1)/2$

Therefore,

$$p(t_1 < \tau < t_2) = e^{-(t-\frac{\Delta}{2})/\langle \tau \rangle} - e^{-(t+\frac{\Delta}{2})/\langle \tau \rangle} \quad (2.4)$$

where $\Delta = t_2 - t_1$ is the width of the bin.

Therefore, the value of $\langle \tau \rangle$ was calculated from fitting the data of Fig. 9 to the following equation:

$$f(t) = e^{-\left(t-\frac{\Delta}{2}\right)/\langle\tau\rangle} - e^{-\left(t+\frac{\Delta}{2}\right)/\langle\tau\rangle} \quad (2.5)$$

Where Δ is a constant that depends on the width of the bins used to construct the histogram, and $\langle\tau\rangle$ is the only fitting parameter. The rate constants for the transitions were calculated as $\langle\tau\rangle^{-1}$.

APPENDIX B

SUPPLEMENTAL INFORMATION FOR CHAPTER 4

Supporting Information

for

Defining the Impact of Cyanine Conformational Restraint in the Near-Infrared Range

Contents

1. General Materials and Methods
2. Synthetic Procedures
 - A. Figure B1. ^1H and ^{13}C NMR assignments of 2 (in MeOD).
 - B. Figure B2. ^1H NMR of A) pure equilibrated (red) and B) diastereomeric mixture (blue) of 6 in MeOD.
3. Photophysical Measurements
 - A. Figure B3A. Transient spectroscopy data (in ethanol) for 2 at different delay times.
 - B. Figure B3B. Relationship between τ_F and viscosity for 1 and 2 in different solvents.
 - C. Figure B4. Lifetime data for A) parent heptamethine indocyanine 1 and B) constrained heptamethine indocyanine 2 in different solvents.

- D. Figure B5. Lifetime data for A) parent heptamethine indocyanine 1 and B) constrained heptamethine indocyanine 2 at different temperatures (in °C) in ethanol.
 - E. Table B1. Photophysical data collected for 1 and 2 in protic and aprotic solvents.
4. Computational Chemistry Methods and Results
- A. Table B2. Computed absorbance (top section) and emission (bottom section) energies vs. experimentally measured (eV).
 - B. Figure B6. Computed and experimental absorbance and emission energies (nm).
 - C. Figure B7. Chain bond length (top) and bond angle (bottom) changes when going from parent indocyanine to its conformationally restricted form.
5. ¹H and ¹³C and Associated 2-D NMR Spectra
6. References

1. General Materials and Methods

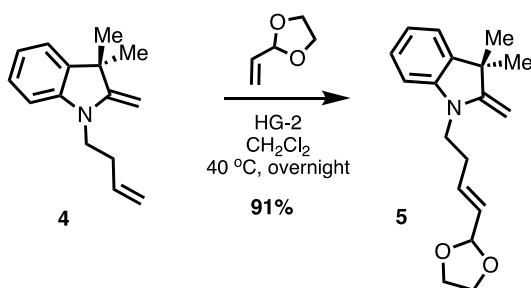
All commercially obtained reagents were used as received. 2,3,3-trimethyl indoline, N-[5-(Phenylamino)-2,4-pentadienylidene]aniline mono hydrochloride, Hoveyda-Grubbs II catalyst were purchased from Sigma-Aldrich (St. Louis, MO). Flash column chromatography was performed using reversed phase (100 Å, 20-40-micron particle size, RediSep® Rf Gold® Reversed-phase C18 or C18Aq) on a CombiFlash® Rf 200i (Teledyne Isco, Inc., Lincoln, NE). High-resolution LC/MS analyses were conducted on a Thermo-Fisher LTQ-Orbitrap-XL hybrid mass spectrometer system with an Ion MAX API electrospray ion source in negative ion mode. Analytical LC/MS was performed using a Shimadzu LCMS-2020 Single Quadrupole utilizing a Kinetex 2.6 µm C18 100 Å (2.1 x 50 mm) column obtained from Phenomenex, Inc (Torrance, CA). Runs employed a gradient of 0→90% MeCN/0.1% aqueous formic acid over 4.5 min at a flow rate of 0.2 mL/min. ¹H NMR and ¹³C NMR spectra were recorded on Bruker spectrometers (at 400 or 500 MHz or at 100 or 125 MHz) and are reported relative to deuterated solvent signals. Data for ¹H NMR spectra are reported as follows: chemical shift (δ ppm), multiplicity, coupling constant (Hz), and integration. Data for ¹³C NMR spectra are reported in terms of chemical shift. Absorbance curves were obtained on a Shimadzu UV-2550 spectrophotometer operated by UVProbe 2.32 software.

Data analysis and curve fitting were performed using MS Excel 2011 and GraphPad Prism 7. See http://pubs.acs.org/userimages/ContentEditor/1218717864819/joceah_abbreviations.pdf for standard acronyms and abbreviations.

2. Synthetic Procedures

The synthesis of **4** was conducted according to our previously reported literature procedure.¹

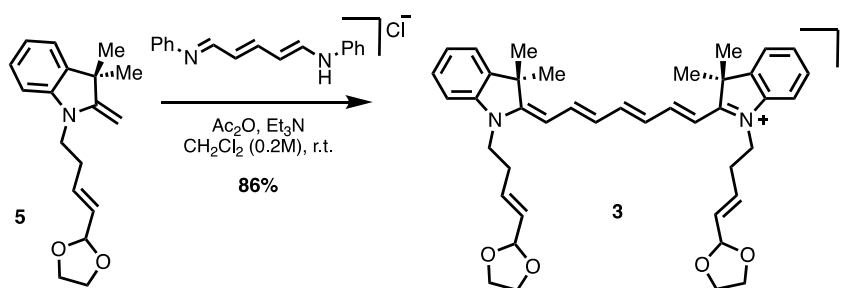
Synthesis of dioxolane-conjugate adduct (**5**):



To a solution of **4** (300mg, 0.826 mmol, 1.0 equiv.) and Hoveyda-Grubbs II catalyst (50 mg, 0.082 mmol, 0.10 equiv.) in anhydrous DCM (4mL, 0.2M) was added 2-vinyl-1,3-dioxolane (420 μ L, 4.13 mmol, 5 equiv.) under argon after degassing with vacuum. The reaction was refluxed at 40 °C for 20 hours and reapplied to static vacuum/argon (g) every 30 minutes for the first 4 hours. The progress of the reaction was monitored by LC/MS and upon completion, the reaction was cooled to room temperature and quenched with NaHCO₃ (4 mL). The biphasic mixture was then separated, extracted with DCM (3 \times 30 mL), dried (Na₂SO₄), and concentrated *in vacuo*. The crude reaction mixture was then purified by normal phase column chromatography (40 g silica column, 0 – 50% Hex/EtOAc) to afford the desired product **5** (215 mg, 0.754 mmol, 91% yield) as a pale-pink oil. ¹H NMR (500 MHz, CDCl₃) δ 7.13 (td, *J* = 7.7, 1.2 Hz, 1H), 7.11 – 7.08 (m, 1H), 6.77 (td, *J* = 7.4, 1.1 Hz, 1H), 6.54 (d, *J* = 7.8 Hz, 1H), 5.98 (dt, *J* = 15.2, 6.9 Hz, 1H), 5.60 (ddt, *J* = 15.5, 6.2,

1.4 Hz, 1H), 5.22 (d, $J = 6.2$ Hz, 1H), 4.02 – 3.93 (m, 2H), 3.92 – 3.86 (m, 4H), 3.62 – 3.56 (m, 2H), 2.44 (ddd, $J = 14.3, 7.2, 1.3$ Hz, 2H), 1.35 (s, 6H). ^{13}C NMR (126 MHz, CDCl_3) δ 161.15, 145.50, 137.50, 133.76, 128.43, 127.48, 121.85, 118.39, 105.05, 103.66, 73.40, 64.90, 44.15, 41.33, 29.98, 28.49. HRMS (ESI) calculated for $\text{C}_{18}\text{H}_{23}\text{NO}_2$ ($\text{M}+\text{H}$) $^+$ 286.1802, observed 286.1813.

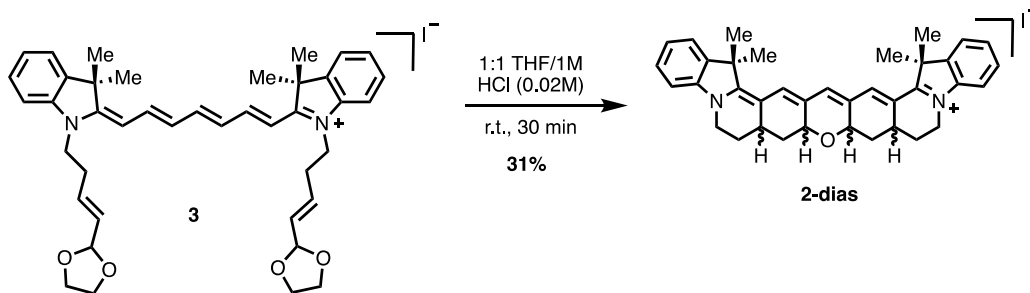
Synthesis of bis-indole cyanine adduct (3):



To a solution of **5** (300 mg, 1.052 mmol, 3 equiv.), N-[5-(Phenylamino)-2,4-pentadienyldiene] aniline monochloride (100 mg, 0.351 mmol, 1.0 equiv.), and Et_3N (245 μL , 1.76 mmol, 5 equiv.) in anhydrous DCM (1.75 mL, 0.2M) was added Ac_2O (100 μL , 1.052 mmol, 3 equiv.). The reaction mixture was left to stir at room temperature for 12 hours and then heated to 40 $^\circ\text{C}$ for an additional 3 hours. The progress of the reaction was monitored by LC/MS and upon completion, the reaction was cooled to room temperature and quenched with NaHCO_3 (2 mL). The biphasic mixture was then separated, extracted over DCM (3×15 mL) and concentrated *in vacuo*. The crude reaction mixture was then re-dissolved in a 1:1 mixture of DCM (20 mL) 1M NaI (20 mL) and stirred vigorously over 2 hours. Next, the DCM layer was separated, washed with H_2O (10 mL), dried (Na_2SO_4) and concentrated *in vacuo*. The concentrate was purified via normal phase column

chromatography (24 g silica column, 0 – 10% DCM/MeOH) to yield **3** (230 mg, 0.302 mmol, 86% yield) as a dark blue solid. ^1H NMR (500 MHz, MeOD) δ 7.93 (t, J = 13.1 Hz, 2H), 7.46 (dd, J = 7.5, 1.1 Hz, 2H), 7.39 (td, J = 7.8, 1.2 Hz, 2H), 7.27 (d, J = 7.9 Hz, 2H), 7.23 (t, J = 7.4 Hz, 2H), 6.58 (t, J = 12.7 Hz, 2H), 6.30 (d, J = 13.6 Hz, 2H), 5.96 (dt, J = 15.0, 7.3 Hz, 2H), 5.47 (dd, J = 15.9, 6.3 Hz, 2H), 5.08 (d, J = 5.8 Hz, 2H), 4.20 (t, J = 6.9 Hz, 4H), 3.84 – 3.79 (m, 4H), 3.79 – 3.75 (m, 4H), 2.66 – 2.53 (m, 4H), 1.69 (s, 12H). ^{13}C NMR (126 MHz, MeOD) δ 173.44, 157.72, 153.00, 143.62, 142.45, 132.25, 131.87, 129.70, 127.15, 126.00, 123.38, 111.99, 105.37, 104.22, 100.08, 65.84, 50.38, 43.80, 31.18, 28.10. HRMS (ESI) calculated for $\text{C}_{41}\text{H}_{49}\text{N}_2\text{O}_4$ (M) $^+$ 633.3687, observed 633.3669.

Synthesis of a diastereomeric mixture of the constrained cyanine (2-dias):



To a dark blue solution of **3** (50 mg, 0.069 mmol, 1.0 equiv.) in THF (1mL) was added 1M HCl (1mL). Upon addition of acid, the reaction mixture immediately turned dark green. The reaction mixture was left to stir at room temperature and the progress was monitored by LC/MS analysis. Significant product formation was seen in 30 minutes, after which time the reaction mixture was quenched with NaHCO_3 (1 mL), extracted over DCM (3×15 mL), dried (Na_2SO_4) and concentrated *in vacuo*. The crude reaction mixture was then re-dissolved in a 1:1 mixture of DCM (15 mL) and 1M NaI (15 mL) and stirred vigorously

11.4, 4.3 Hz, 2H), 2.40 – 2.32 (m, 2H), 1.76 – 1.73 (m, 2H), 1.70 (d, $J = 4.5$ Hz, 12H), 1.45 (q, $J = 11.7$ Hz, 2H). ^{13}C NMR (126 MHz, MeOD) δ 167.91, 143.62, 143.08, 142.53, 141.26, 132.67, 129.68, 126.09, 123.25, 115.35, 111.14, 73.83, 49.97, 44.09, 36.53, 32.63, 28.77, 28.20, 27.71. HRMS (ESI) calculated for $\text{C}_{37}\text{H}_{39}\text{N}_2\text{O}$ (M^+) 527.3057, observed 527.3043.

Position	δ_{H} (mult., J in Hz)	δ_{C} (mult., J in Hz)
1	–	167.91
2	–	49.97
3	–	143.62 or 142.53
4 – 7	7.47 (d, $J = 6.9$ Hz, 2H), 7.39 (td, $J = 7.8, 1.2$ Hz, 2H), 7.24 (t, $J = 7.4$ Hz, 2H), 7.21 (m, 2H)	143.08, 129.68, 126.09, 123.25
8	–	143.62 or 142.53
9	4.28 (dd, $J = 13.7, 4.1$ Hz, 2H), 3.80 (td, $J = 13.2, 4.0$ Hz, 2H)	44.09
10	2.40 – 2.32 (m, 2H) 1.76 – 1.73 (m, 2H)	28.77
11	2.80 (tt, $J = 12.4, 4.1$ Hz, 2H)	32.63
12	2.44 (dt, $J = 11.4, 4.3$ Hz, 2H) 1.45 (q, $J = 11.7$ Hz, 2H)	36.53
13	–	73.83
14	7.22 (s, 1H)	111.14
15	–	132.67
16	7.50 (s, 2H)	141.26
17	–	115.35
18 – 19	1.70 (d, $J = 4.5$ Hz, 12H)	28.20, 27.71

Figure B1. ^1H and ^{13}C NMR assignments of **2** (in MeOD).

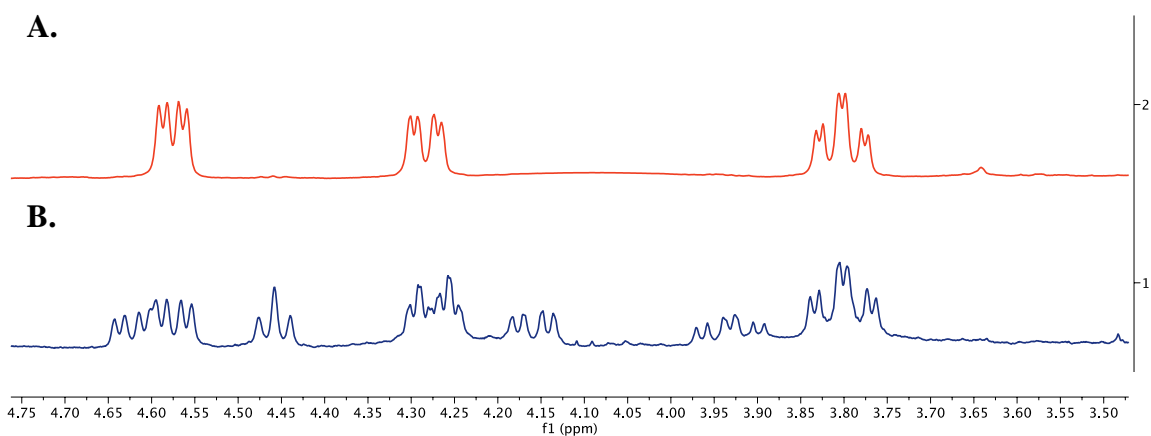
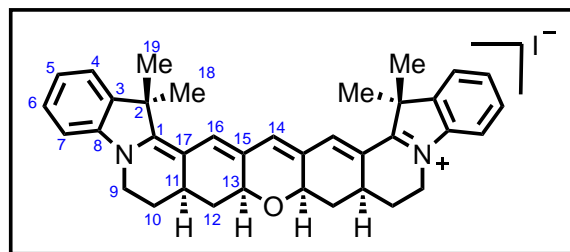


Figure B2: ^1H NMR of (A) pure equilibrated (red) and (B) diastereomeric mixture (blue) of **2** in MeOD.

3. Photophysical measurements

Absorption and Steady-State Fluorescence Spectroscopy:

Absorption spectra were measured using a Shimadzu UV-1700 PharmaSpec UV-VIS spectrophotometer. Fluorescence emission spectra for absolute quantum yield determinations were recorded on a PTI QuantaMaster steady state spectrofluorometer operated by FelixGX 4.2.2 software, with 4 nm excitation and emission slit widths, and a 0.1 s integration rate. The absolute quantum yields (ϕ_F) of **1** and **2** in DCM were measured using a Quantaurus-QY spectrometer (model C11374) from Hamamatsu. This instrument uses an integrating sphere to determine photons absorbed and emitted by a sample.

Measurements were carried out using dilute samples ($A < 0.1$) and self-absorption corrections were performed using the instrument's software.

Fluorescence emission spectra for relative quantum yield determinations were measured on a Nanolog fluorometer (Horiba Jobin Yvon). Fluorescence spectra were corrected for wavelength-dependent detector responsivity using correction curves determined with a calibrated light source. Relative fluorescence quantum yields were determined for **1** and **2** in a variety of solvents using the corresponding compounds in DCM as reference ($\phi_F = 0.455$ and $\phi_F = 0.401$ for **1** and **2** in DCM, respectively).

Fluorescence quantum yields (ϕ_F) were determined as $\phi_F = \phi_{F,R} \frac{I (1 - 10^{-A_R}) n^2}{I_R (1 - 10^{-A}) n_R^2}$ where the subscript R refers to the standard used as a reference (i.e. the compounds dissolved in DCM), I represents the integrated corrected fluorescence spectrum, A is the absorbance of the solution at the excitation wavelength used to determine I , and n is the refractive index of the solvent. Absorbances at the excitation wavelength (680 nm for **1** and 725 nm for **2**) were kept around $A \sim 0.05$ in all fluorescence experiments to avoid inner filter artifacts. To improve the precision in the determination of A for the calculation of ϕ_F , absorbances were measured for solutions displaying $A \sim 0.5$ at the shoulder (i.e. excitation wavelength) of the spectrum and precise 1:10 dilutions were performed before the fluorescence determinations.

Time-Resolved Fluorescence Spectroscopy

Time-Correlated Single Photon Counting (TCSPC) setup used Fianium supercontinuum laser (SC- 450-4-PP) operating at 20 MHz for the excitation light. The

excitation wavelength was set at 700 nm for all the lifetime measurements. The emission was set at 775 nm and 800 nm for **1** and **2** lifetime measurements, respectively. The detector was a Hamamatsu MCP-PMT R3809U- 50 photomultiplier tube and data was recorded with a Becker and Hickl TCSPC Timing Card (B&H SPC830). The instrument response function (IRF) was measured by scattering excitation light off a 3% Ludox solution. For the temperature-based experiment, the temperature was controlled using a water circulator and was measured inside the cuvette with a thermocouple. Intensity decays were fitted using ASUFIT, a MATLAB-based program developed at ASU.

(<http://www.public.asu.edu/~laserweb/asufit>)

Transient absorption measurements

Transient absorption spectra were measured using EOS Nanosecond-to-millisecond Transient Absorption Spectrometer in the range of 500 –1000 nm. The excitation source consists of a KHz regeneratively-amplified Ti:S laser, and two optical parametric amplifiers (Spectra Physics). The excitation wavelength was set at 750 nm for these experiments. The measurement time window was set at 100 μ s. Initial spectra were averaged as mentioned in the legends of the graph. Intensity decays at specific wavelengths were fitted using the ASUFIT.

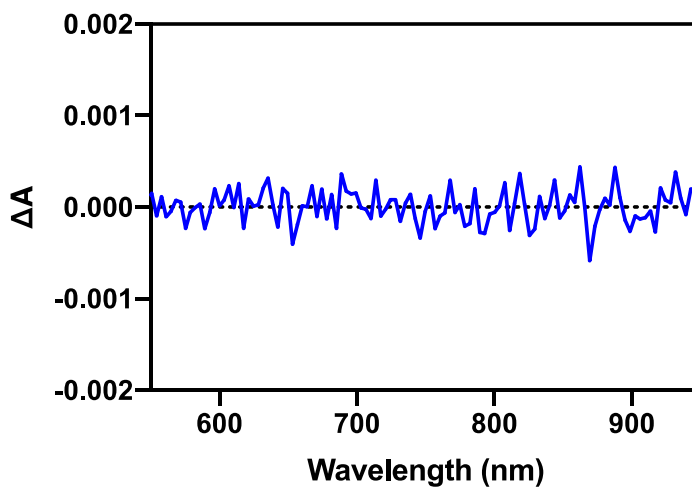
FCS measurements

FCS measurements were carried out on a custom-built confocal microscope based on an Olympus IX-71. The laser (LDH 760 D-C, PicoQuant GmbH, Germany) was cleaned

up using a 740/40 bandpass filter (Thorlabs GmbH) and focused onto the sample by an oil-immersion objective (UPLSAPO100XO, NA 1.40, Olympus Deutschland GmbH). A dichroic beam splitter (Quad Line Beamsplitter zt488/543/635/730rpc, Chroma Technology Corporation) separated the excitation from the emission light. The emission light was focused on a 50 μm pinhole (Thorlabs GmbH) and sent through a bandpass filter (810/80, Thorlabs GmbH). Emission light was collected by an avalanche photodiode (SPCM-AQRH-14-TR, Excelitas Technologies GmbH & Co. KG) and registered by a single-photon counting module (HydraHarp 400, PicoQuant GmbH). A commercial software package was used to record time traces and to calculate and fit correlation curves (SymphoTime 64, PicoQuant GmbH). We employed the built-in FLCS correction to suppress detector after pulsing effects.

Samples were diluted to nanomolar concentrations and measured in a reducing and oxidizing buffer system with enzymatic oxygen removal consisting of 90% buffer A (100 mM MgCl_2 , 40 mM Tris, 2 mM Trolox/Troloxquinone and 1% w/v Glucose) and 10% buffer B (glucose oxidase (1 mg/mL), 0.4 % (v/v) catalase (50 $\mu\text{g/mL}$), 30 % glycerol, 12.5 mM KCl in 50 mM TRIS). A laser power of 25 μW and a repetition rate of 80 MHz was used. The confocal volume was placed 10 μm into the solution. Each sample was measured for 30 minutes.

A.



B.

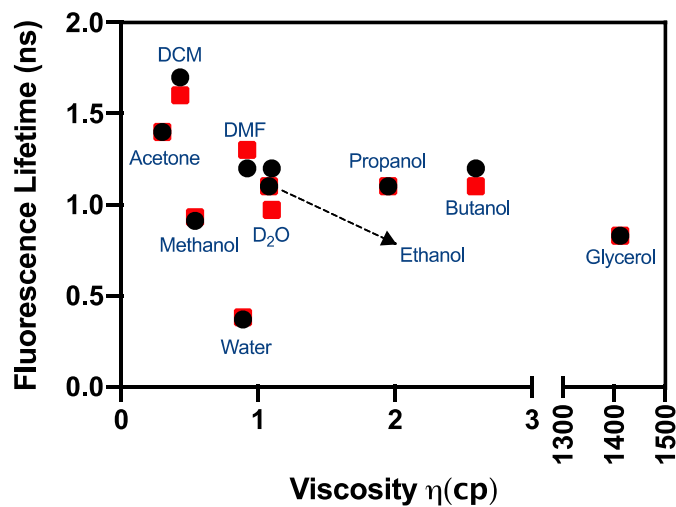


Figure B3: (A) Difference transient absorption spectrum of **1** in glycerol at a 50 ns delay time. The positive absorption signal observed with **1** in ethanol (Figure 2A) is not observed in glycerol at any delay time. (B) Relationship between Fluorescence lifetime (τ_F) and viscosity for **1** (black circle) and **2** (red square) in different solvents

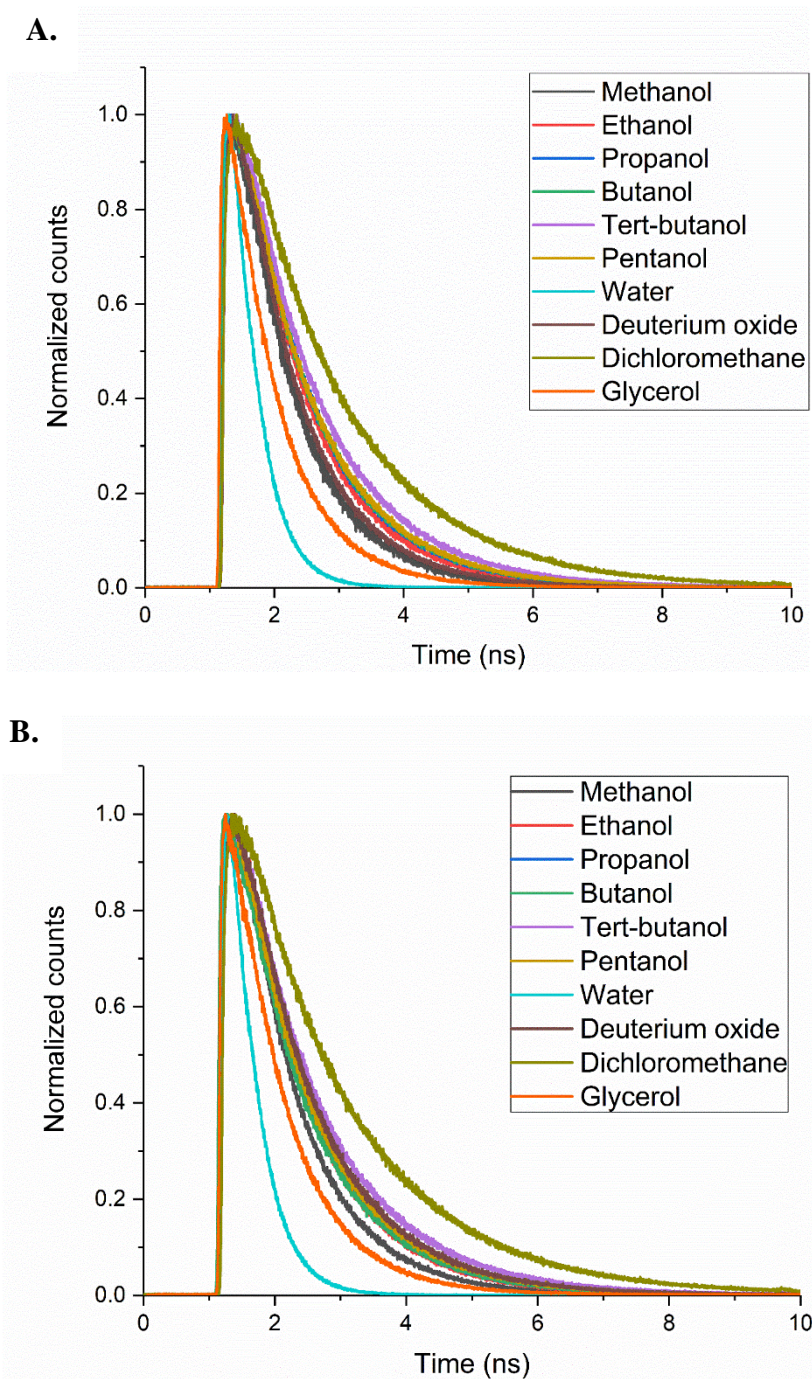


Figure B4: Lifetime data for (A) Parent heptamethine indocyanine **1** and (B) Constrained heptamethine indocyanine **2** in different solvent. Lifetimes are listed in Table S1.

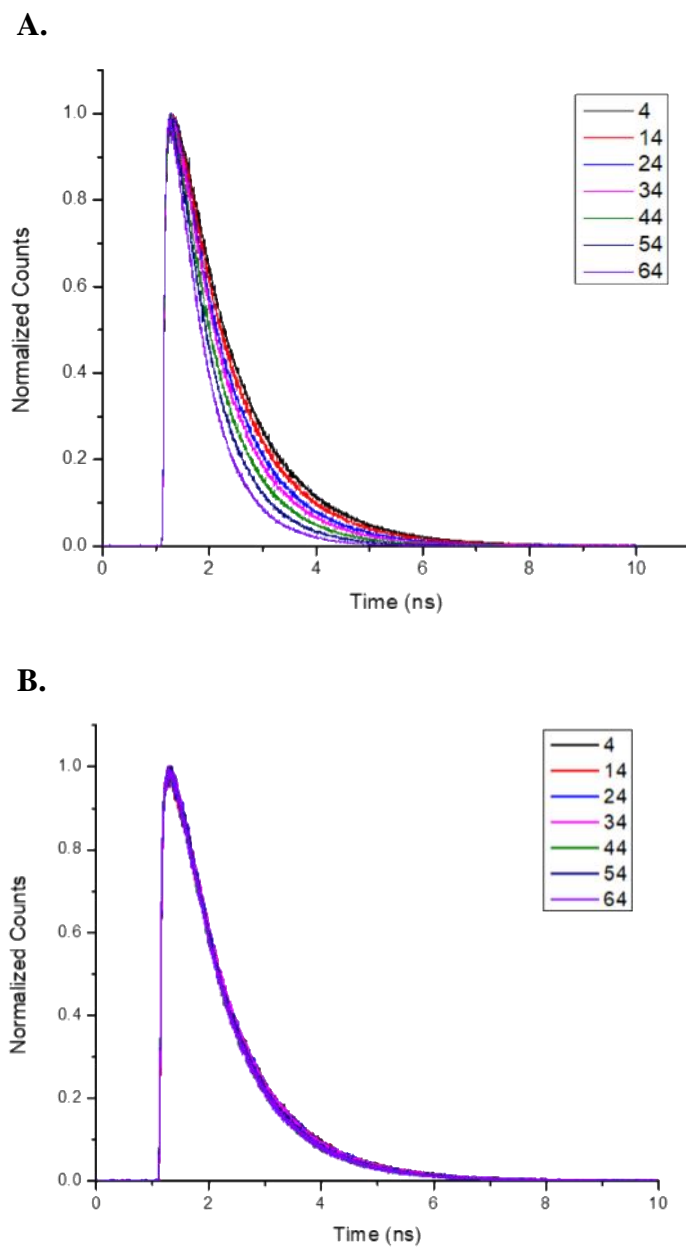


Figure B5: Lifetime data for (A) Parent heptamethine indocyanine **1** and (B) Constrained heptamethine indocyanine **2** at different temperatures (as shown in the legend; in °C) in ethanol.

Table B1. Photophysical data collected for **1** and **2** in protic and aprotic solvents

Solvents	Solvent Properties		1			2		
	Dielectric constant	η (cp)	ϕ_F	τ_F (ns)	$\ln(k_{nr})$	ϕ_F	τ_F (ns)	$\ln(k_{nr})$
Methanol	33.6	0.54	0.24	0.91	-0.180	0.29	0.93	-0.270
Ethanol	25	1.08	0.24 [†]	1.1	-0.370	0.31	1.1	-0.466
Propanol	21.51	1.95	0.26	1.1	-0.396	0.3	1.1	-0.452
Butanol	18.34	2.59	0.30	1.2	-0.539	0.32	1.1	-0.481
T-butanol	18.74	6.68	0.35	1.2	0.613	0.34	1.3	-0.678
Pentanol	15.8	3.5	0.31	1.2	-0.553	0.32	1.2	-0.568
Water *	80.36	0.89	0.064	0.37	-0.928	0.081	0.38	0.883
Glycerol	42.5	1412	0.26	0.83	-0.115	0.28	0.83	-0.142
DCM	9.02	0.43	0.46	1.6	-1.086	0.40	1.7	-1.041
D ₂ O	78.3	1.1	0.2	0.97 ^{††}	-0.193	0.18	1.2	-0.381
Acetone	21.36	0.30	0.33	1.4	-0.737	0.37	1.4	-0.799
DMF	37.06	0.92	0.31	1.3	-0.633	0.34	1.2	-0.598

*Contains 5% DMSO in all steady-state experiments (no DMSO in lifetime experiments).

4. Computational Chemistry Methods and Results

Quantum chemistry calculations were performed using a local version of the GAMESS package and molecular orbitals were illustrated using MacMolPlt.⁵⁻⁷ The 6-31G(d) and cc-pVTZ basis sets have been used.⁸⁻⁹

Density functional theory (DFT) utilizing the B3LYP functional was used to optimize ground state (S0) geometries.¹⁰⁻¹³ The time-dependent density functional theory (TDDFT) method¹⁰⁻¹⁶ was used to compute vertical excitation, or absorbance, energies (S0 → S1*) at ground state (S0) optimized geometries, as well as deexcitation, or emission, energies (S1 → S0*) at singlet excited state optimized geometries (S1).¹⁴⁻¹⁹ Ground state (S0) DFT and excited state (S1) TDDFT computations used the Euler-MacLaurin radial and Lebedev angular grids with respective dimensions (96, 302) and (48, 110).²⁰⁻²² All reported DFT and TDDFT results used the cc-pVTZ basis set.

The occupation restricted multiple active space (ORMAS) method with second-order perturbation theory correction (ORMAS-PT2) was also used to compute vertical excitation (absorbance) energies and deexcitation (emission) energies.²³⁻²⁵ ORMAS-PT2 calculations were performed using the 6-31G(d) basis set at B3LYP/6-31G(d) ground state (S0; vertical excitation energy) and TDDFT-B3LYP/6-31G(d) excited state (S1; deexcitation energy) optimized geometries. For each system the ORMAS active space contained all valence π electrons (e), orbitals (o) and the associated configuration interaction (CI) spaces were constructed as follows: we start with the (2 electron, 2 orbital) base active space (HOMO-like orbital + LUMO-like orbital with two electrons, i.e., (2,2) active space)(doubly occupied valence π orbitals not including HOMO-like orbital) and

apply all single and double excitations out of this reference and into a virtual orbital space containing only the remaining valence π orbitals. HOMO and LUMO refer to the highest occupied molecular orbital and lowest unoccupied molecular orbital, respectively, in a closed-shell wavefunction. These ORMAS wavefunctions represent active spaces of (20e, 19o), (22e, 21o), and (24e, 23o) for the parent and conformationally restrained versions of trimethine, pentamethine, and heptamethine indocyanines, respectively. The ORMAS S0 and S1 wavefunctions were then simultaneously optimized (for orbitals and CI coefficients) by minimizing the average of the energies of the ground (S0) and excited (S1) singlet states. For example, for parent heptamethine indocyanine the \$DET/\$ORMAS GAMESS input specifications were:

```
$det   ncore=98 nels=24 nact=23 nstate=3 wstate(1)=1,1 $end
$ormas   nspace=3   mstart(1)=99,110,112   mine(1)=20,0,0
maxe(1)=22,4,2 $end
```

and for conformationally restrained heptamethine indocyanine they were:

```
$det   ncore=129 nels=24 nact=23 nstate=3 wstate(1)=1,1 $end
$ormas   nspace=3   mstart(1)=130,141,143   mine(1)=20,0,0
maxe(1)=22,4,2 $end
```

Subsequent ORMAS-PT2 energies for each state (S0 and S1) were then computed by modeling all single and double valence electron excitations out of the individual S0 and S1 ORMAS reference wavefunctions (1s orbitals were kept core).

Table B2: Computed absorbance (top section) and emission (bottom section) energies vs. experimentally measured (eV). All calculations included water solvent effects via the Polarizable Continuum Model (PCM). Differences (computed – experimental) given in parentheses and mean unsigned errors (MUEs) shown at bottom of each section.

System/Method		TDDFT- B3LYP-PCM	ORMAS-PT2- PCM	Experiment
Absorbance				
Trimethine indocyanine	Parent	2.631 (0.373)	2.409 (0.151)	2.258 ^a
	Conformationally restrained	2.569 (0.347)	2.341 (0.119)	2.222 ^a
Pentamethine indocyanine	Parent	2.334 (0.391)	2.088 (0.145)	1.943 ^b
	Conformationally restrained	2.240 (0.367)	2.000 (0.127)	1.873 ^b
Heptamethine indocyanine	Parent	2.089 (0.404)	1.849 (0.164)	1.685 ^c
	Conformationally restrained	1.978 (0.378)	1.749 (0.149)	1.600 ^c
MUE		0.377	0.143	
Emission				
Trimethine indocyanine	Parent	2.174 (–0.028)	2.196 (–0.006)	2.202 ^a
	Conformationally restrained	2.156 (–0.008)	2.162 (–0.002)	2.164 ^a
Pentamethine indocyanine	Parent	1.939 (0.052)	1.969 (0.082)	1.887 ^b
	Conformationally restrained	1.884 (0.053)	1.906 (0.075)	1.831 ^b
Heptamethine indocyanine	Parent	1.725 (0.117)	1.780 (0.172)	1.608 ^c
	Conformationally restrained	1.644 (0.084)	1.693 (0.133)	1.560 ^c
MUE		0.057	0.078	

^a Klehs, K.; Spahn, C.; Endesfelder, U.; Lee, S. F.; Furstenberg, A.; Heilemann, M., Increasing the brightness of cyanine fluorophores for single-molecule and superresolution imaging. *Chemphyschem* **2014**, *15* (4), 637-41.

^b Michie, M. S.; Gotz, R.; Franke, C.; Bowler, M.; Kumari, N.; Magidson, V.; Levitus, M.; Loncarek, J.; Sauer, M.; Schnermann, M. J., Cyanine Conformational Restraint in the Far-Red Range. *J Am Chem Soc* **2017**, *139* (36), 12406-12409.

^c This work.

All calculations were performed in solvent (water) phases via the polarizable continuum model (PCM) approach for the DFT, TDDFT, ORMAS, and ORMAS-PT2 methods.²⁶⁻³⁰

In all cases a high density of tesserae was used (NTSALL = 960 in \$TESCAV).

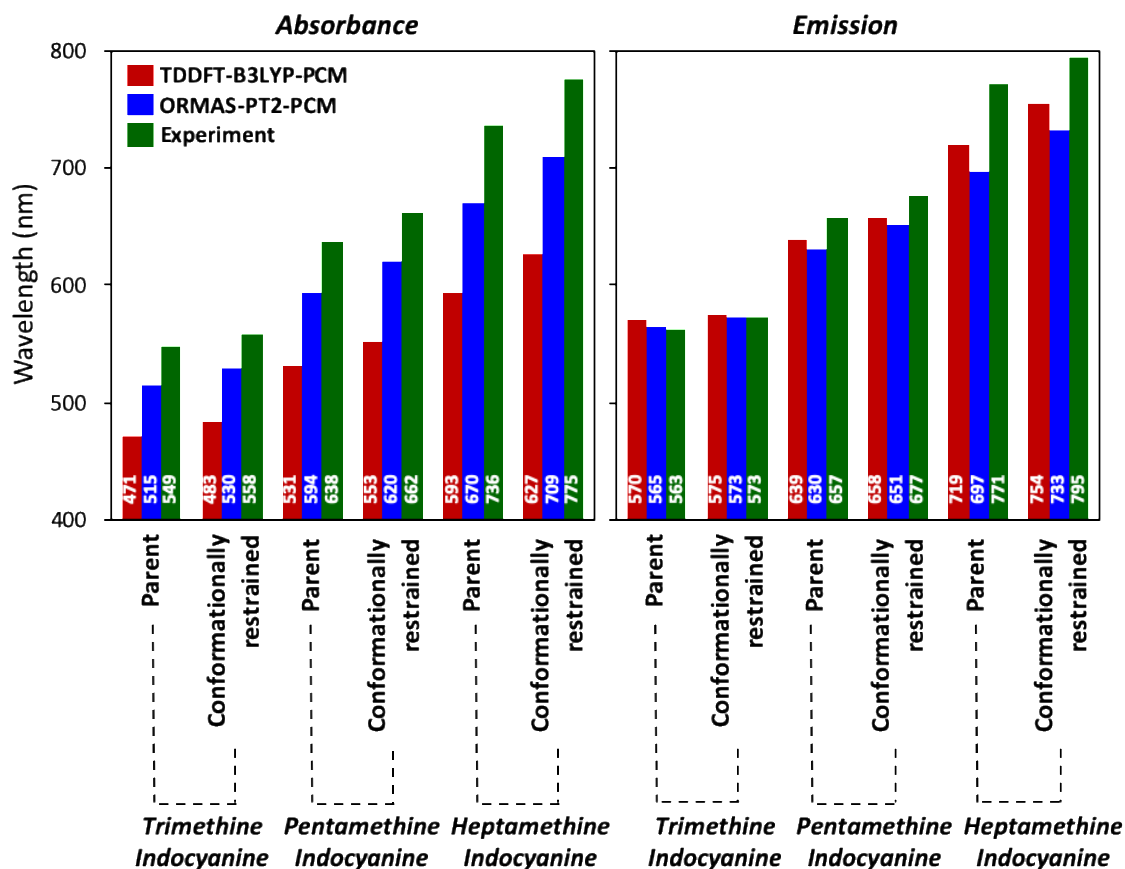


Figure B6: Computed and experimental absorbance and emission energies (nm). See Table B2 and Sections 6 and 7 for more details.

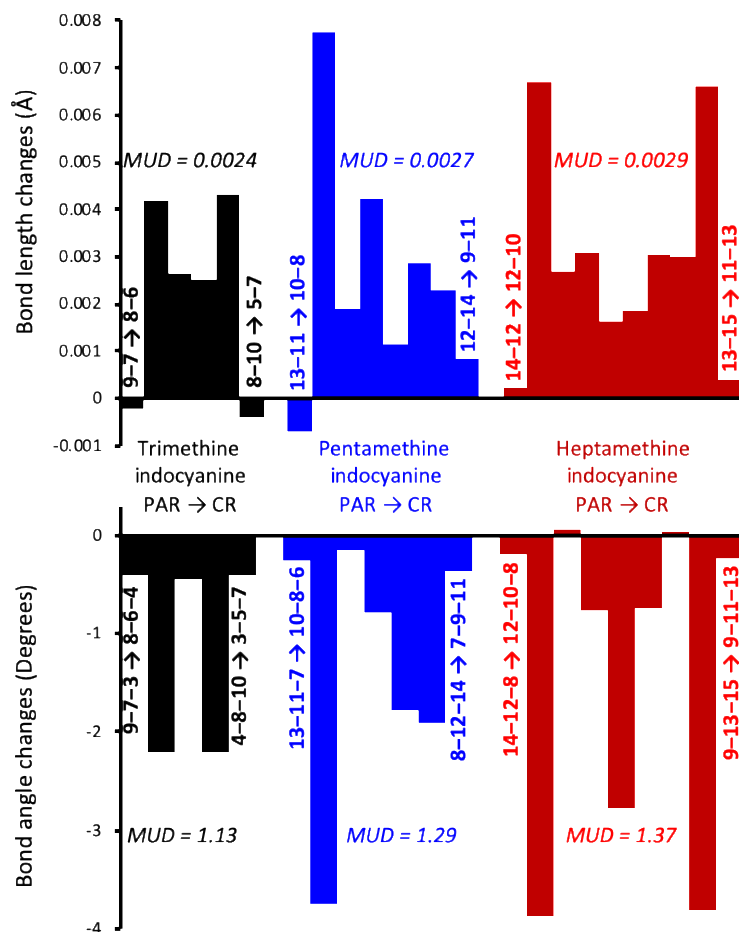


Figure B7: Chain bond length (top) and bond angle (bottom) changes when going from parent indocyanine to its conformationally restricted form. Parameter changes are determined sequentially for heavy atoms starting and ending at nitrogen atoms. Actual start/end bonds and angles are given where atom numberings correspond to the Cartesian coordinates (B3LYP-PCM/cc-pVTZ optimized geometries) provided in Section 6. Mean unsigned differences (MUDs) are also shown. **Note: PAR and CR stand for parent and conformationally restrained indocyanine variant.**

Section B5. ^1H and ^{13}C and Associated 2-D NMR Spectra

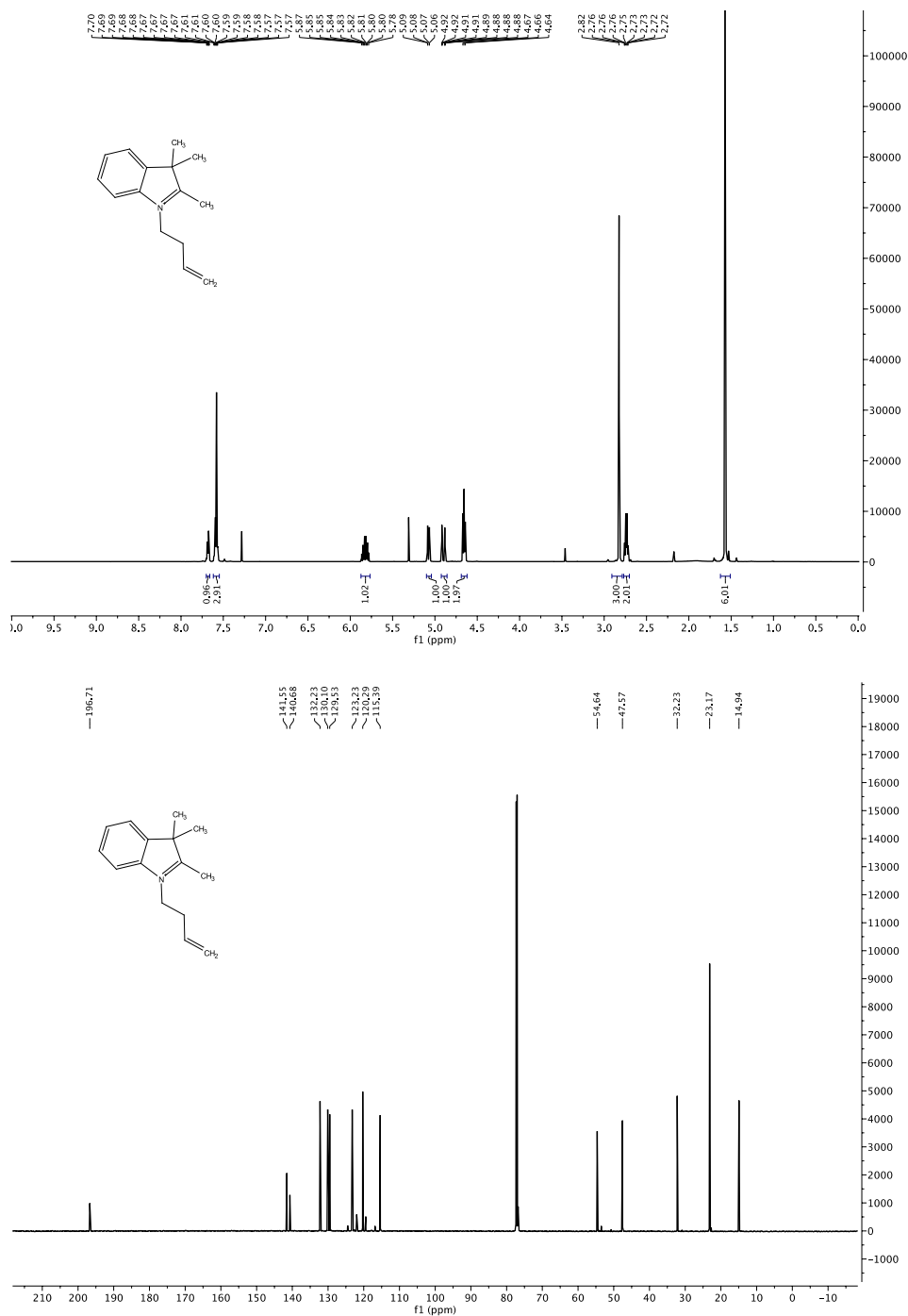


Figure B8: ^1H and ^{13}C NMR spectra of 4

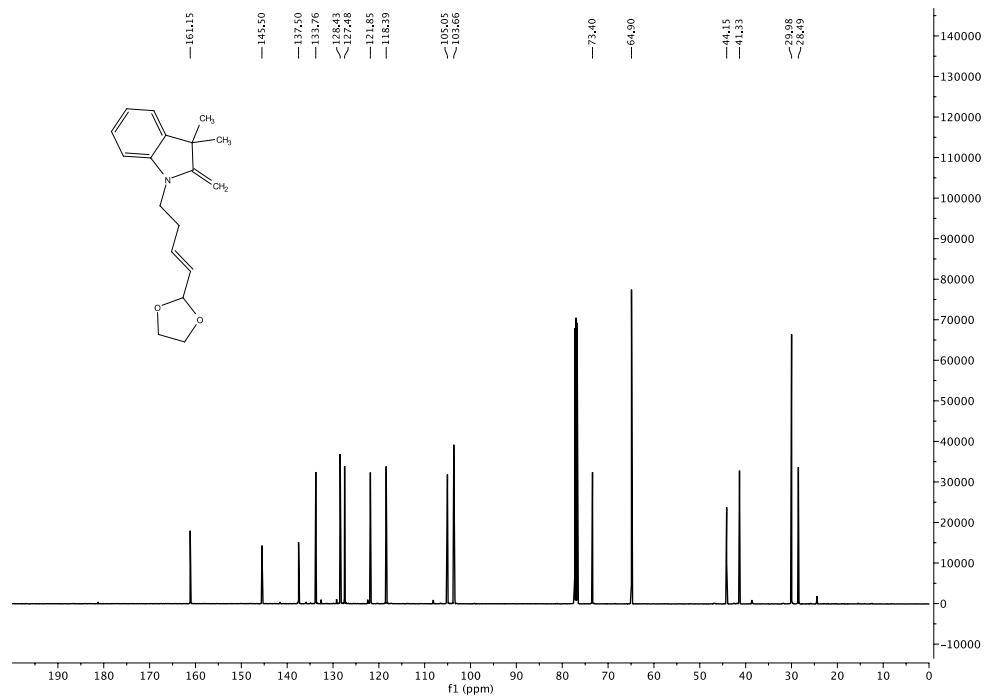
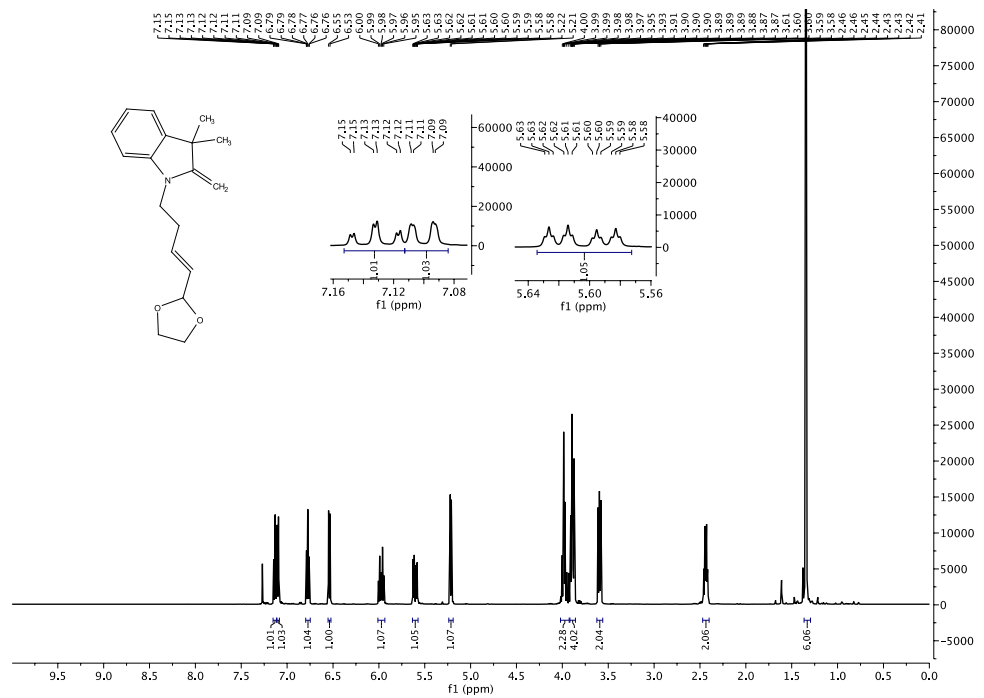


Figure B9: ¹H and ¹³C NMR spectra of 5

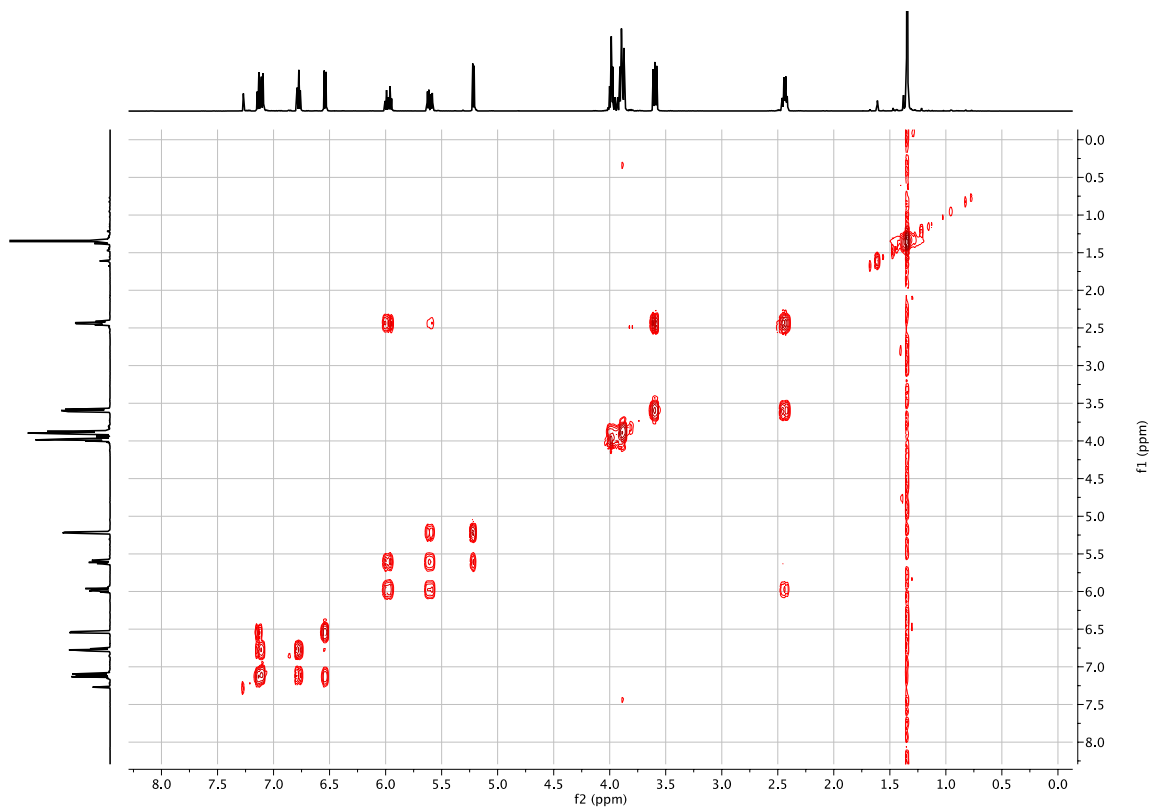


Figure B10: Gradient COSY NMR spectra of **5**

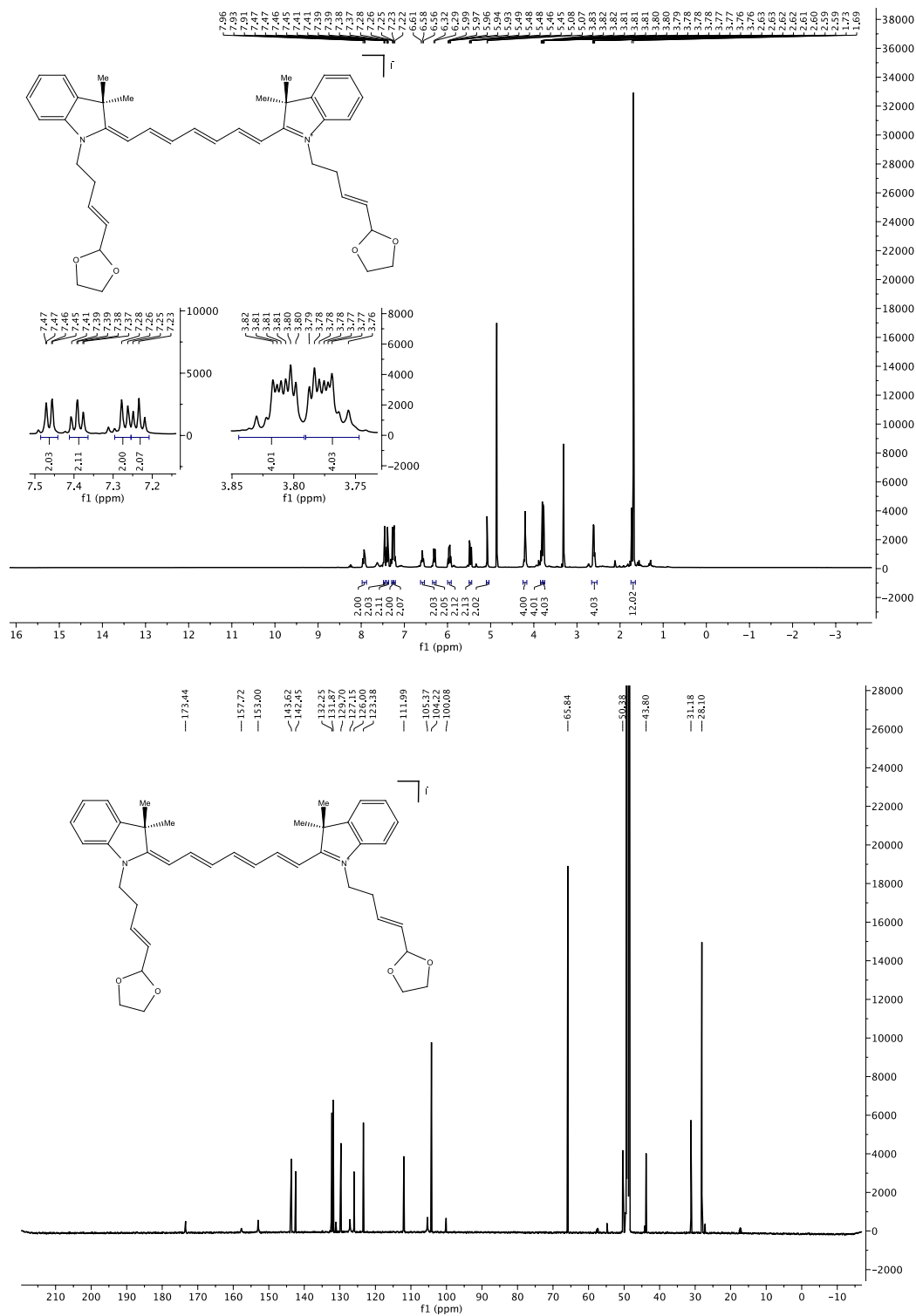


Figure B11: ¹H and ¹³C NMR spectra of **3**

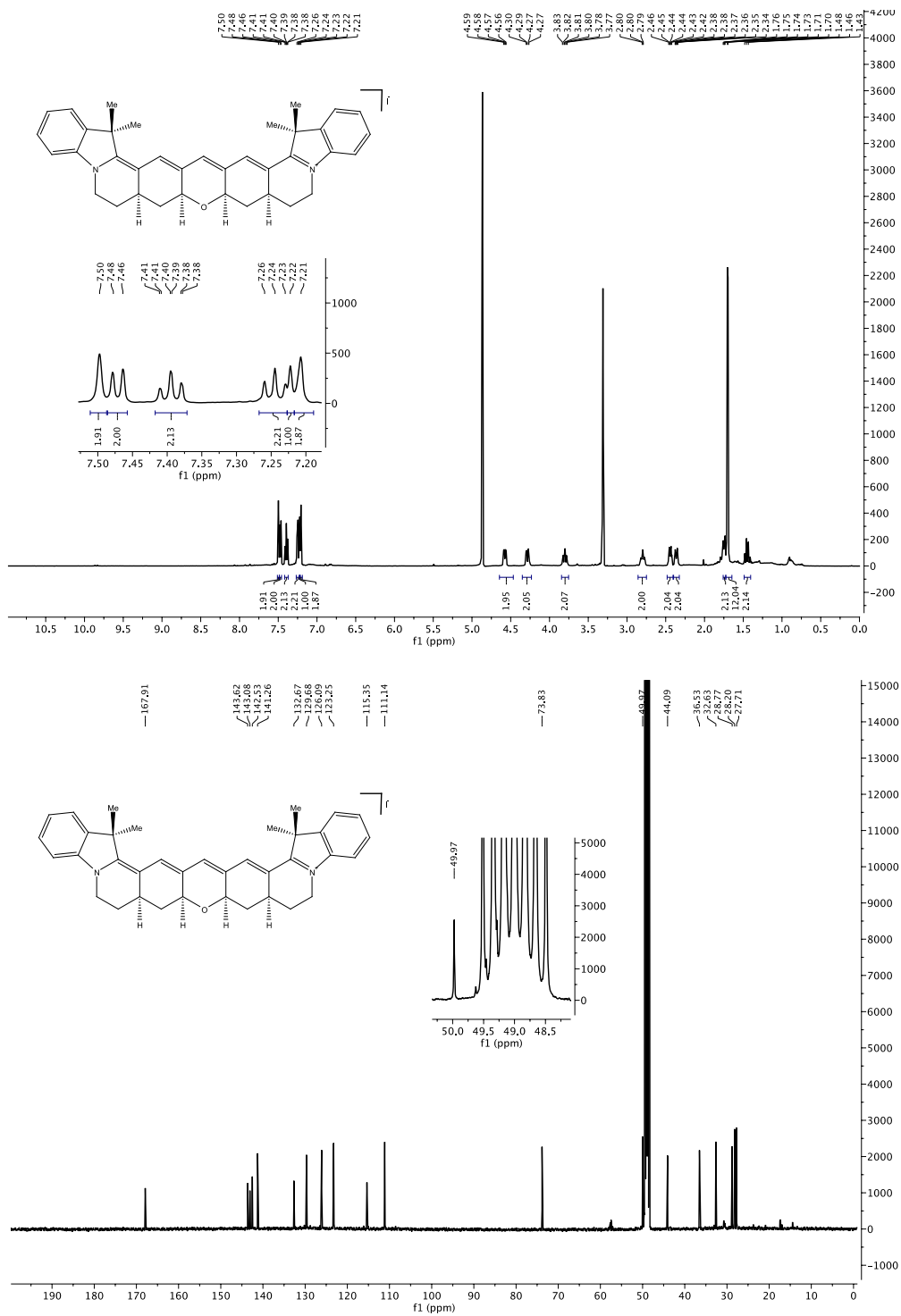


Figure B12: ¹H and ¹³C NMR spectra of 2

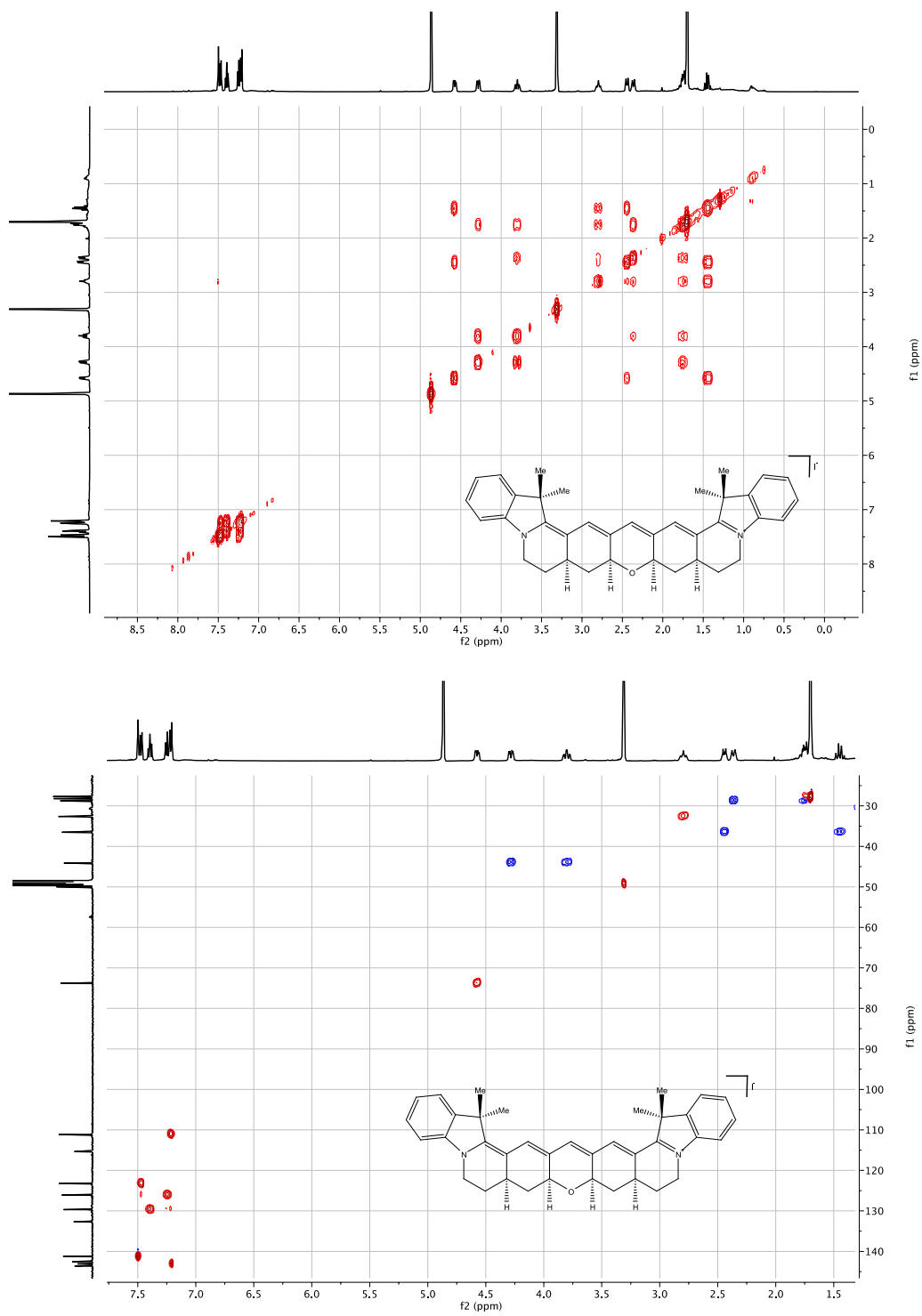


Figure B13: Gradient COSY and HSQC NMR spectra of **2**

APPENDIX C

GLOBAL LIFETIME REPRODUCIBILITY STUDIES FOR CHAPTER 5

Table C1: Lifetime Analysis for Two Dataset of DNA Sequence. The sequences ending with repeat are the second dataset.

Sample	A_1	A_2	A_3	A_4	τ_1 (ns)	τ_2 (ns)	τ_3 (ns)	τ_4 (ns)	$\langle \tau \rangle$ (ns)
1 rev	0.402	0.495	0.097	0.006	0.07	0.31	1.00	6.09	0.32
1 rev-repeat	0.420	0.467	0.107	0.006	0.07	0.31	0.92	6.68	0.31
1	0.709	0.278	0.009	0.004	0.03	0.12	1.46	5.83	0.09
1-repeat	0.725	0.263	0.009	0.004	0.04	0.12	1.68	6.98	0.10
2	0.873	0.116	0.007	0.004	0.03	0.14	1.87	5.92	0.08
2-repeat	0.849	0.140	0.008	0.004	0.03	0.12	1.53	6.59	0.08
3	0.381	0.557	0.056	0.006	0.08	0.31	1.05	5.55	0.29
3-repeat	0.384	0.549	0.060	0.007	0.09	0.31	0.98	6.13	0.30
4	0.593	0.375	0.025	0.006	0.06	0.24	1.08	5.95	0.19
4-repeat	0.575	0.397	0.0230	0.005	0.07	0.24	1.2	6.6	0.20
4 rev	0.676	0.310	0.010	0.004	0.04	0.13	1.66	4.93	0.10
4 rev-repeat	0.675	0.311	0.011	0.004	0.04	0.12	1.69	5.85	0.11

The lifetime experiment was repeated and the data analysis were compared to check for the reproducibility. From the results, the analysis seems to be robust. Please note that the

longest component lifetime changes are significant. However, the fractional component, which is of interest to access the population distribution is consistent between two sets of data.

APPENDIX D








REUSE PERMISSION OF PUBLISHED WORK

DECLARATION


I verify that the co-authors of the published work have approved of my use of our publications in my dissertation.

Nikita Kumari

LICENSE



Home Help Email Support Sign In Create Account




Cyanine Conformational Restraint in the Far-Red Range
Author: Megan S. Michie, Ralph Götz, Christian Franke, et al
Publication: Journal of the American Chemical Society
Publisher: American Chemical Society
Date: Sep 1, 2017
Copyright © 2017, American Chemical Society

PERMISSION/LICENSE IS GRANTED FOR YOUR ORDER AT NO CHARGE

This type of permission/license, instead of the standard Terms & Conditions, is sent to you because no fee is being charged for your order. Please note the following:

- Permission is granted for your request in both print and electronic formats, and translations.
- If figures and/or tables were requested, they may be adapted or used in part.
- Please print this page for your records and send a copy of it to your publisher/graduate school.
- Appropriate credit for the requested material should be given as follows: "Reprinted (adapted) with permission from (COMPLETE REFERENCE CITATION). Copyright (YEAR) American Chemical Society." Insert appropriate information in place of the capitalized words.
- One-time permission is granted only for the use specified in your request. No additional uses are granted (such as derivative works or other editions). For any other uses, please submit a new request.

[BACK](#) [CLOSE WINDOW](#)



Impact of Cyanine Conformational Restraint in the Near-Infrared Range
Author: Siddharth S. Matikonda, Gabrielle Hammersley, Nikita Kumari, et al
Publication: The Journal of Organic Chemistry
Publisher: American Chemical Society
Date: May 1, 2020
Copyright © 2020, American Chemical Society

PERMISSION/LICENSE IS GRANTED FOR YOUR ORDER AT NO CHARGE

This type of permission/license, instead of the standard Terms & Conditions, is sent to you because no fee is being charged for your order. Please note the following:

- Permission is granted for your request in both print and electronic formats, and translations.
- If figures and/or tables were requested, they may be adapted or used in part.
- Please print this page for your records and send a copy of it to your publisher/graduate school.
- Appropriate credit for the requested material should be given as follows: "Reprinted (adapted) with permission from (COMPLETE REFERENCE CITATION). Copyright (YEAR) American Chemical Society." Insert appropriate information in place of the capitalized words.
- One-time permission is granted only for the use specified in your request. No additional uses are granted (such as derivative works or other editions). For any other uses, please submit a new request.

[BACK](#) [CLOSE WINDOW](#)